

GOLD AS A SENSING PLATFORM FOR THE RAPID DETECTION OF  
EXPLOSIVES AND MALARIAL BIOMARKERS

By

Christopher P. Gulka

Dissertation

Submitted to the Faculty of the  
Graduate School of Vanderbilt University  
in partial fulfillment of the requirements  
for the degree of

DOCTOR OF PHILOSOPHY

in

Chemistry

December, 2014

Nashville, Tennessee

Approved:

David W. Wright

Richard F. Haglund

Timothy P. Hanusa

Darryl J. Bornhop

## ACKNOWLEDGEMENTS

The work presented in this dissertation could not have been possible without the gracious funding provided by the Defense Threat Reduction Agency (DTRA), the North Atlantic Treaty Organization (NATO), the Bill and Melinda Gates Foundation, and Vanderbilt University. The funding provided by these organizations has greatly facilitated my research efforts including but not limited to: procurement of reagents and lab supplies, reserving instrument time slots, providing a reliable and safe atmosphere in which to work, the ability to present my work at conferences, and the disbursement of my stipend.

There are so many people that have helped pave the road in earning my degree. First, I would like to thank my research advisor, Prof. David Wright. You have truly created an enjoyable research experience for me, even though I've been "fired" and reprimanded too many times to count on both hands. Nevertheless, you are one of the most passionate individuals I have ever had the privilege of meeting, and the free reign that you have afforded me over my project has spurred my scientific creativity. I would also like to thank my collaborator in Biomedical Engineering, Prof. Rick Haselton, for his guidance, mentorship, and ability to force me to think abstractly. I would finally like to thank my collaborators and committee members: Profs. Richard Haglund, David Cliffel, Timothy Hanusa, and Darryl Bornhop.

When I first started graduate school, I was always really interested in joining a lab with an active dynamic and I don't think I could have made a better choice with the Wright lab. I have had the privilege of working not only with individuals who have aided



in my professional development, but individuals who I consider true friends. Dr. Josh Swartz was my graduate student mentor when I first joined the lab and really got me off the ground running. Your passion for learning and teaching helped facilitate my transition between undergrad and graduate school. I have always considered Dr. Becca Sandlin as the big sister that I never had, because whether you disapproved of my girlfriend or my attitude, you always “told it like it is.” I really appreciate that because it is often difficult to receive criticism in science and I believe you have ameliorated this process for me. Considering your current position at Harvard and your upbringing in Monterey, TN, you are truly inspirational, and I am so lucky to have met you. I would also like to thank Dr. Stephen Jackson as a compassionate friend and as a mentor. I don’t know what I would have done without you that night when we had to install the HPLC computers. You definitely didn’t have to stay in lab until midnight to install them. You also didn’t have to stay late ensuring I was well prepared for my qualifying exam. I would also like to thank Dr. John Stone for his mentorship, optimism, compassion, and friendship. Finally, I would like to thank other previous lab members and research fellows: Dr. S. Reese Harry, Dr. Anh Hoang, Dr. Jonas Perez, Holly Carrell, Phoebe Penamon, Matthew Bryant, Alexander Denton, Alec Pawlukiewicz, and Lidalee Silva-Baucage.

I am also extremely lucky to work with lab members who have supported my research endeavors. With so many different ongoing projects in the lab, there is such a diverse array of knowledge surrounding me. Since science is so interdisciplinary nowadays, everyone in lab possesses his or her own unique skillset. Whether I have asked for help or just sought out someone to bounce off ideas, it has been an amazing experience when you all have been there for me. With that, I would like to thank the

following current lab members: Dr. Joseph Conrad, Dr. Alex Rutledge, Dr. Nick Adams, Keersten Davis, Jenny Nesbitt, Anna Bitting, Kim Fong, Adam Travis, Wes Bauer, Lauren Gibson, Alexis Wong, Nicholas Wright, and Christine Markwalter. In addition, I have had the privilege of working with wonderful student collaborators who have been integral in my research efforts and professional development: Dr. Joshua Trantum, Evan Gizzie, and Mark Baglia. Finally, I would also like to thank: Dr. Tony Hmelo, Dr. James McBride, Dr. Ben Schmidt, and Dr. Dmitry Koktysh for training and guidance with respect to VINSE equipment and Andrzej Balinski for training and guidance with respect to numerous instruments in the analytical lab. Finally, I would like to thank the second-shift custodians, especially Greg and Eddie, for their pick-me-up talks, late-night life advice, and encouraging words of optimism.

My admittance to the chemistry department at Vanderbilt University would not have been possible without the mentorship and support of my undergraduate advisor and close friend at the University of Richmond, Prof. Michael Leopold, also known as “Leo.” This man possesses the challenging ability to mold undergraduate minds into future scientists. His greatest talent is allowing a student to recognize his or her strengths while simultaneously developing their weaknesses. It was Leo that first told me that I could actually be a scientist and upon hearing this, I was shocked. My first reaction was, “Who would want me?” But after some convincing and numerous long conversations, he got me believing too. Leo always puts students first, whether he is extending his office hours until midnight before an exam, mentoring his students in a research setting, or discussing future graduate or professional plans. He has always puts his students first and would do anything to fight for them.

Finally, I would like to thank my brother, Casey, my father, Ronald, and my late mother, Cynthia, for their endless love and support. It was extremely difficult watching my mother deteriorate for a year before losing her battle with cancer, but the love I received from family, friends, and mentors has put me in a strong and stable position, both emotionally and professionally. As an anonymous source once said, "Life goes on." I am also glad that my father has found happiness with his wife, Beth, the newest addition to our family. Beth's love and support (and her proclivity for mixology) has made life easier and I look forward to what the future holds for them.

## TABLE OF CONTENTS

	Page
ACKNOWLEDGEMENTS.....	ii
LIST OF TABLES.....	viii
LIST OF FIGURES.....	viii
Chapter	
I. INTRODUCTION.....	1
Efforts Towards Point-of-Care Testing and Rapid Sensing.....	1
An Ancient Material as a Substrate for Sensor and Diagnostic Development.....	2
Scope of Dissertation.....	5
II. SELECTIVE BIOMIMETIC RECOGNITION OF NITROAROMATIC EXPLOSIVE MOLECULES USING A QUARTZ CRYSTAL MICROBALANCE SENSOR.....	7
Abstract.....	7
Introduction.....	8
Materials and Methods.....	11
Results and Discussion.....	13
Conclusions.....	22
Section Acknowledgements.....	23
III. ELECTROCHEMICAL DETECTION OF 2,4,6-TRINITROTOLUENE AT COLLOIDAL GOLD NANOPARTICLE FILM ASSEMBLIES.....	24
Abstract.....	24
Introduction.....	25
Materials and Methods.....	28
Results and Discussion.....	30
Conclusions.....	42
Future Directions.....	43
Section Acknowledgements.....	45
IV. NI(II)NTA GOLD AND SILVER NANOPARTICLES AS LOW-RESOURCE MALARIAL DIAGNOSTIC PLATFORMS FOR THE RAPID COLORIMETRIC DETECTION OF <i>PLASMODIUM FALCIPARUM</i> HISTIDINE-RICH PROTEIN-II.....	46

Abstract.....	46
Introduction.....	47
Materials and Methods.....	50
Results and Discussion .....	55
Conclusions.....	72
Section Acknowledgements.....	73
V. COFFEE RINGS AS LOW-RESOURCE DIAGNOSTICS: DETECTION OF THE MALARIAL BIOMARKER <i>PLASMODIUM FALCIPARUM</i> HISTIDINE-RICH PROTEIN-II USING A SURFACE COUPLED RING OF NI(II)NTA GOLD-PLATED POLYSTYRENE MICROPARTICLES .....	75
Abstract.....	76
Introduction.....	77
Materials and Methods.....	79
Results.....	83
Discussion .....	92
Conclusions.....	97
Section Acknowledgements.....	98
VI. PROOF-OF-CONCEPT OF THE CAPTURE-AND-RELEASE OF THE MALARIAL BIOMARKER <i>PLASMODIUM FALCIPARUM</i> LACTATE DEHYDROGENASE .....	99
Introduction - Future Directions to Enhance Malarial RDTs .....	99
Materials and Methods.....	102
Results and Discussion .....	107
Outlook for POC Diagnostics and Rapid Sensing .....	111
REFERENCES .....	115
Appendix	
A. Alternative Microbead Platform Technologies for Detection of the <i>P. falciparum</i> HRP-II Malarial Biomarker .....	127
B. Supplementary Data: Chapter II.....	137
C. Supplementary Data: Chapter IV .....	140
D. Supplementary Data: Chapter V .....	149
CURRICULUM VITAE.....	157

## LIST OF TABLES

Table	Page
1. Sequences of Molecular Recognition Peptides and Their Denoted Abbreviations .....	14
2. Calculation of Dissociation Constants ( $K_D$ ) of Nitroaromatic Target Molecules Adsorbed to Selective Recognition Peptides Using Langmuir Isotherm and Kinetic Models.....	21

## LIST OF FIGURES

Figure	Page
1. Proposed Schematic of Biomimetic Recognition Using a QCM Sensor .....	10
2. Quantitative and Qualitative Analyses of Peptide Adsorption onto a Gold Surface .....	15
3. Nitroaromatic Target Adsorption to a Piranha-Cleaned Gold Surface .....	17
4. Nitroaromatic Target Adsorption to Immobilized Recognition Peptides .....	19
5. Selectivity of Immobilized Nitroaromatic Recognition Peptides .....	20
6. Titrations of Nitroaromatic Target Adsorption to Their Respective Recognition Peptides .....	20
7. Characterization of Colloidal Suspensions of Citrate-Capped AuNPs.....	31
8. Assembly of Citrate-Capped AuNP Films on Au Substrates .....	32
9. Electrochemical Capacitance Measurements of Various AuNP Film Assemblies.....	34
10. Surface UV-vis Spectra of AuNP Film Assemblies .....	34
11. Titrations of TNT Measured via Square Wave Voltammetry .....	37
12. AuNP Film Assembly Sensor Performance.....	39
13. Catalytic Performance of AuNP Film Assemblies .....	41
14. Depiction of Ni(II)NTA AuNP Aggregation Induced by <i>Pf</i> HRP-II, Triggering a Spectrophotometric Redshift and a Red-to-Purple Color Change .....	50

15. Structures and Abbreviations of Spacer Ligands and the NTA Recognition Ligand in This Chapter.....	56
16. Ni(II)NTA AuNP Characterization.....	57
17. Spectrophotometric and Dynamic Laser Light Scattering Spectral Shifts of Ni(II)NTA AuNPs upon Coordination of Ligands to Metal Surface .....	57
18. Aggregation of Ni(II)NTA AuNPs in the Presence of 100 nM rcHRP-II at pH 5.5 ...	59
19. Titration of rcHRP-II with Ni(II)NTA AuNPs Assembled with Varying Spacer Ligands.....	61
20. Stability of Ni(II)NTA AuNPs at 37°C. ....	63
21. Effect of 125 mM Imidazole on Peg <sub>4</sub> :Ni(II)NTA AuNP Aggregation when Induced by rcHRP-II.....	64
22. Workflow of Low-resource Detection of rcHRP-II Using the Peg <sub>4</sub> :Ni(II)NTA AuNP Platform.....	66
23. Titrations of rcHRP-II with Peg <sub>4</sub> :Ni(II)NTA AuNPs when the Biomarker is Dissolved in a Physiological Concentration of Human Serum Albumin and Plasma .....	67
24. Spectrophotometric and Dynamic Laser Light Scattering Spectral Shifts of 20 nm Ni(II)NTA AgNPs upon Coordination of Ligands to Metal Surface .....	69
25. Aggregation of Ni(II)NTA AgNPs upon Reactions with 100 nM rcHRP-II.....	70
26. Titration of rcHRP-II and GST with 80 pM Peg <sub>4</sub> :Ni(II)NTA AgNPs.....	70
27. Stability Studies of 80 pM Peg <sub>4</sub> :Ni(II)NTA AgNPs.....	72
28. Proposed Strategy of Ring Formation for rcHRP-II Detection Using Ni(II)NTA AuPSs.....	78
29. Titration of rcHRP-II against 15 nm Ni(II)NTA AuNP Rings.....	84
30. Proposed Synthesis of Ni(II)NTA AuPSs .....	86
31. Characterization of AuPSs upon Addition of AuNP Seeds and Au Plating.....	87
32. Activity and specificity of Ni(II)NTA AuPSs .....	88
33. Microparticle Flow Patterns at Different Densities .....	89

34. Ni(II)NTA AuPS Ring Assay for Detection of rcHRP-II .....	90
35. Analysis of Ring Formation upon Titrating rcHRP-II with Ni(II)NTA AuPSs .....	92
36. Ni(II)NTA AuPS Ring Assay upon Dissolving rcHRP-II in 4 mg/mL Human Serum Albumin .....	96
37. Schematic of Capture-and-Release of <i>Pf</i> LDH .....	102
38. MALDI-MS Spectrum of Hexa-His Peptide .....	104
39. Real-Time Binding Kinetics of Hexa-His-Tagged Antibody to Ni(II)NTA Sensor Tips .....	108
40. Malstat Assay Exhibits a Colorimetric Response as a Function of Increasing Concentrations of <i>Pf</i> LDH .....	109
41. Titration of <i>Pf</i> LDH upon Capture-and-Release Assay in Lysed Whole Blood.....	111



## Chapter I

### INTRODUCTION

#### **Efforts Towards Point-of-Care Testing and Rapid Sensing**

Within the past few decades, a push towards combating diseases in the developing world along with generous donations has afforded innovative research efforts for drug therapies and point-of-care (POC) diagnostic devices (1). Often times, expensive instruments have the ability to detect diseases, biomarkers, and toxins in an advanced laboratory setting, but they are not applicable in the regions where electricity is intermittent, running water is scarce, and trained personnel are absent. Therefore, a lot of research has focused on developing POC diagnostic techniques and sensors that can operate according to the World Health Organization's (WHO) ASSURED acronym: affordable, sensitive, specific, user-friendly, rapid and robust, equipment-free, and deliverable to those in need in low-income regions (2). For many tropical diseases, accurate diagnosis is essential not only to control the endemic, but also to curb resistance for effective drug therapies. Research efforts to combat these diagnostic issues in the third world have developed paper substrates to rapidly identify small molecules and proteins (3-7). They cost pennies to manufacture, and can be successfully operated by an unskilled user in minutes. Additionally, paper sensors are huge steps for healthcare, because their successful implementation for rapid diagnosis of tropical diseases in the developing world can ultimately be incorporated into western society for diseases such as cancer, stroke, heart disease, etc. However, a movement towards diagnosing disease in

western medicine can only be achieved if the issues in the developing world are solved first using innovative research platforms (1). As healthcare costs soar in this country, rapid and low-cost POC diagnostics and sensors have the potential to more effectively streamline governmental regulations on healthcare, alleviating many of the expenses and energies of modern technology.

The three commonalities in a sensor or a POC device are: a sensing platform or substrate, a molecular recognition element to bind the analyte of interest, and a signal transduction component to generate a digital readout upon molecular recognition (8). A current obstacle in creating sensors and POC devices for the developing world is the lack of available resources, so that innovative technologies are required to produce signal transduction events without electricity and trained personnel. Keeping in mind the intermittent availability of resources of the developing world, this dissertation provides fundamental platform technologies for small molecule explosive sensors and malarial protein biomarkers, respectively, using a common gold substrate.

### **An Ancient Material as a Substrate for Sensor and Diagnostic Development**

The naturally occurring element, gold, has been extensively exploited since antiquity as jewelry, decorative art, and units of currency and exchange (9). In ancient times, the inherent high density of the material was taken advantage of in order to complicate the counterfeiting of gold coins, while its robust integrity persevered over years of commerce and trade. Dating back centuries, men and women have been adorned with gold rings as lifelong commitments to one another. Gold's reflective shine emanated from incident radiation represents an ostentatious entity of monogamy, while its stability

and resistance to tarnishing symbolizes the eternal vows of matrimony. In the production of stained glass art, nanometer-sized gold particles were employed to offer richer, brighter red colors in comparison to alternative metals and dyes that still remain on display today (10-11). Nevertheless, the common denominator associated with gold jewelry, art, and currency is the continuous persistence of this noble metal (12).

In terms of sensor and diagnostic development, a substrate material that possesses the ability to maintain stability in extreme climates over prolonged time periods can greatly aid POC diagnostic testing and real-time sensing applications. Although gold has been displayed as a decorative and flamboyant entity since ancient times, its chemical, physical, and optical properties have only recently been elucidated. As a bulk material, gold obtains its shiny gloss from the dense and stable array of electrons comprising the material. Because there is a small quantity of atoms exposed to the surface in bulk gold, the vast majority of atoms are packed densely within the material's interior, engaging in minimal movement. As incident radiation strikes the bulk material, the dense packing of electrons do not allow the photons to penetrate the interior, thus reflecting off of the surface and generating a metallic luster. In contrast, at the nanoscale, many of the laws of classical physics are broken. When the diameter of a colloidal gold particle (AuNP) is less than the wavelength of visible light, it exhibits unique physical, optical, and chemical properties while maintaining its robust integrity like its bulk counterpart (10-11). In general, nanoparticles (< 100 nm) contain a very high surface area-to-volume ratio, so that a more energetic material is obtained when a large percentage of atoms are exposed to the surface. With such a high energy of surface electrons, nanoparticles often absorb

incident radiation rather than reflect it, opening up doors in optical sensing, catalysis, and probe design.

Upon exposure to incident radiation, the active surface electrons oscillate in-phase with the visible radiation at the particle surface (10,11,13-15). Following fundamental quantum mechanics, the electrons oscillate according to one-dimensional particle-in-a-box theory, where the wave oscillates across the particle diameter. The collective electron oscillation, known as the plasmon resonance band, is responsible for the transmission of bright red colors in solution. To convey this phenomenon in a translational perspective, AuNPs are orders of magnitude brighter than the strongest-emitting organic dyes. Additionally, the surface plasmon resonance band is extremely sensitive to changes in the surrounding environment, so that analyte binding/recognition to AuNPs can trigger a signal by altering the electron oscillation frequency.

Although gold is also well known for its inert characteristics and oxidation resistance, it serves as a weak Lewis acid both in bulk and at the nanoscale, demonstrating high reactivity and affinity for weak Lewis bases such as sulfides and primary amines (16). Organic thiols and disulfide compounds have been extensively studied over the past few decades in conjunction with gold substrates because of their proclivity to spontaneously and rapidly assemble into stable monolayers (17-19). The self-assembly characteristics of alkanethiols can be easily tuned to manipulate charge and/or hydrophobicity of the gold-air interface. Furthermore, the ability to couple thiol groups to molecular recognition agents such as antibodies, nucleic acids, peptides, metals, and small molecules facilitates molecular recognition sensing platforms.

## Scope of dissertation

The theme associated with each chapter is the use of gold as a bulk material or as a nanoparticle to develop cheap platform technologies for POC diagnostics and rapid sensing agents. Although gold is often advertised as an expensive entity with respect to jewelry, the femtomole and picomole quantities required for my assays provide material costs under a dime. Additionally, the aforementioned physical and chemical characteristics propose signal transduction capabilities and resistance to oxidation. Finally, the facile, covalent ligand coupling offers manipulation of the surface for rapid sensing and/or rapid molecular recognition. The first two research chapters delve into bulk gold as a platform for nitroaromatic explosive sensing applications. Although these sensors currently require electricity to operate, initial experiments elucidating the platform electrode development are described. Chapter II investigates using bulk gold as a piezoelectric substrate to assemble molecular recognition peptides for specific detection of nitroaromatic explosive small molecules. Chapter III takes advantage of bulk gold as a conductive electrode for electrochemical sensing, assembling colloidal AuNPs to electrocatalytically enhance the reduction and detection of the explosive molecule, 2,4,6-trinitrotoluene.

The final two chapters stray from using gold as a bulk material and focus on investigating the unique properties of AuNPs by developing POC diagnostic platforms to detect the malarial biomarker, *Plasmodium falciparum* Histidine-Rich Protein-2. The final two chapters address many of the issues associated with current malarial diagnostics and offer solutions to overcome those obstacles. Since biological interactions occur mostly at the nanoscale, the modular development of unique nanomaterials to probe these

interactions provides a framework for the next generation of specific and sensitive diagnostics. Chapter IV focuses on the optical properties of AuNPs and silver nanoparticles (AgNPs) to create a proof-of-concept malarial diagnostic platform that transduces the protein recognition event into a colorimetric signal within minutes. The final chapter explores tailoring a thin gold nanoshell encompassing a polystyrene microsphere to synthesize a lightweight bead as another malarial platform diagnostic. The custom, modular microsphere overcomes the sensitivity problems encountered in Chapter IV using an innovative coffee ring assay to capture and concentrate the malarial biomarker. Finally, chapter VI and the appendices offer future directions for malaria assay development using particle platforms.

## Chapter II

### SELECTIVE BIOMIMETIC RECOGNITION OF NITROAROMATIC EXPLOSIVE MOLECULES USING A QUARTZ CRYSTAL MICROBALANCE SENSOR

#### **Abstract**

Trace detection and identification of explosives is essential for national security in the transportation industry, the neutralization of improvised explosive devices and mines in active combat zones, and the elimination of waste sites following the decommissioning of munitions factories. Although dogs and honeybees reveal extremely selective and sensitive olfactory recognition of explosives in the field, the time and money devoted to training such detectors is immense. Because nature continuously shows the ability to discriminate against explosives, biomimetic molecular recognition is an ideal foundation for sensor development. This chapter describes the selective detection of the nitroaromatic explosive, TNT, and its analogs, DNT and TNB, via biomimetic peptide recognition with a quartz crystal microbalance (QCM) sensor platform. The real-time recognition capabilities of the QCM demonstrate selective nitroaromatic target-receptor binding events in minutes without signal amplification. All nitroaromatic targets exhibit enhanced selectivity to their specific recognition motif peptides over the negative controls, but TNT recognition to its selective biomimetic peptide (TNT-BP) displays three-fold selectivity in comparison to DNT and TNB, possessing a  $K_D$  in the range of 29-44  $\mu\text{M}$ .

## Introduction

Since World War I, the nitroaromatic organic molecule, 2,4,6-trinitrotoluene (TNT), has been one of the most widely utilized explosives due to its stability and facile synthetic route (20). Focus on trace explosives detection has attributed to increased security levels in the transportation industry, as well as the necessary neutralization of bombs and landmines in active battlefields (21,22). In addition, since the decommissioning of numerous munitions factories, TNT runoff has polluted the environment, suppressing the growth of multiple organisms and causing health problems from incessant exposure (23-28). Trace detection of TNT is also complicated by natural photodissociation and microbial degradation to yield byproducts such as 1,3,5-trinitrobenzene (TNB) and 2,4-dinitrotoluene (DNT), respectively (29-31). Even though these degradation mechanisms are understood, the development of sensors for rapid detection of nitroaromatics in polluted areas and combat zones continues to be a challenge (32). Currently, airports and military personnel take advantage of ion-mobility spectrometers for the rapid identification of explosives from a complex matrix, but discrimination between false positives and negatives during drift time remains a primary drawback, and the time required for positive or negative results is often a burden (22,33,34). In the field, dogs, bees, rats, and pigs demonstrate olfactory sensing capabilities specific for TNT and its derivatives at very low limits of detection (35,36). However, training for these animals is expensive and rigorous, but by understanding the proteins and enzymes responsible for identifying explosives in these natural organisms, molecular biology can be manipulated to provide building blocks for explosives recognition.



Biomimetic molecular recognition is an emerging field in sensor development because evolutionary selection often results in significantly better discrimination than seen in most synthetic materials. For example, the *Enterobacter cloacae* PB2 bacteria strain is not only able to grow and reproduce in the presence of TNT as the sole nitrogen source, but its enzyme responsible for binding TNT, PETN reductase, contains a Trp-His-Tyr-Thr active site (37,38). By mimicking this natural aromatic active site, 12-mer peptides were screened via mutational phage display to selectively capture the nitroaromatic compounds, TNT and DNT (39). In addition, other biomimetic 12-mer peptides for TNT and TNB recognition were developed, mimicking the Ile-Val-Phe-Trp C-terminal residues of honeybee's TNT-binding antennal-specific protein-1 (ASP-1) (40,41). Both scaffolds contain aromatic substrates rich in electron density to recognize electron-deficient nitroaromatics, suggesting that binding is driven by donor-acceptor interactions. Additionally, peptides as molecular recognition agents can be synthesized in gram quantities and high yields in comparison to alternative agents such as antibodies and aptamers, reducing production costs. Recently, biomimetic peptides as sensor platforms have been successfully incorporated with carbon nanotube and polydiacetylene substrates, but selectivity was only established for one nitroaromatic analyte (42-44).

In this work, the simple, bottom-up sensor design is demonstrated to discriminate against the nitroaromatic explosives, TNT, DNT, and TNB, using selective biomimetic recognition peptide technology (Figure 1). By utilizing a gold substrate, the peptides can be easily assembled onto the substrate by terminating the recognition sequence with a thiol-containing cysteine residue. These previously screened biomimetic peptides can then be easily assembled onto the gold sensor platform to recognize and quantify small

nitroaromatic molecule binding in solution via a piezoelectric detection instrument, the quartz crystal microbalance (QCM). The QCM operates on the basis of acoustic wave propagation, taking advantage of the piezoelectric properties of quartz. By applying an alternating current to the QCM chip, the quartz oscillates at a resonant frequency, so that a mass adsorption onto the substrate reduces the frequency of oscillations, resulting in a proportional signal transduction (45). My facile experimental design provides a selective platform for sensor development with real-time recognition capabilities to identify multiple nitroaromatic analytes.

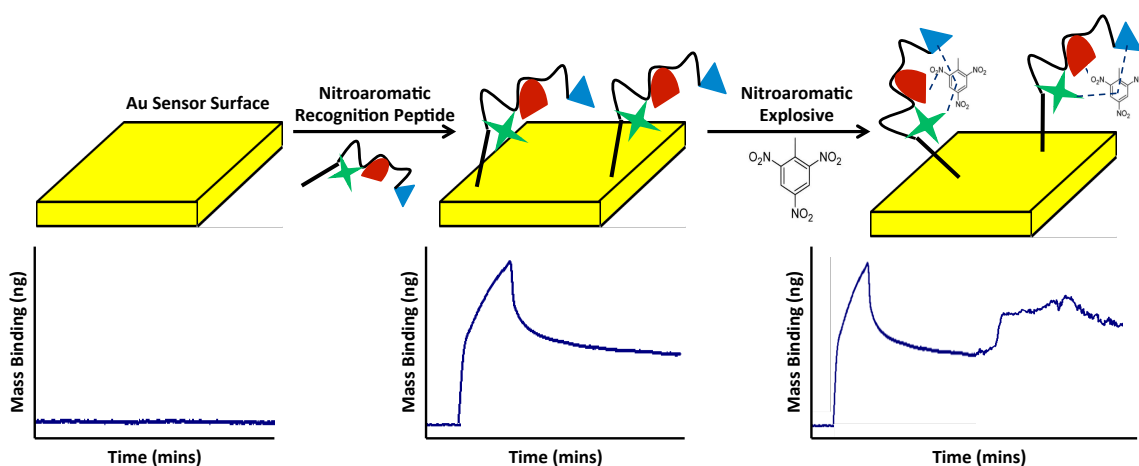


Figure 1. Proposed schematic of biomimetic recognition using a QCM sensor. First, nitroaromatic recognition peptides are immobilized onto the gold by immersing the gold in a peptide solution, and a mass increase is evident by the adsorption of large peptide molecules. Next, molecular recognition is assessed by flowing varying concentrations of nitroaromatic targets over the peptide-functionalized gold surface. Additionally, another mass change is evident via nitroaromatic analyte binding to its respective recognition peptide.

## Materials and Methods

### *Reagents*

Peptide reagents were purchased from AAPTEC Inc. and Advanced ChemTech, save for Fmoc-N-amido-dPEG<sub>8</sub>-acid, which was purchased from Quanta Biodesign Ltd. All nitroaromatic target molecules were of analytical grade dissolved in acetonitrile and purchased from Cerilliant Corporation. 5 MHz quartz/chrome/Au crystals (1 inch) were purchased from Stanford Research Systems, while 9 MHz quartz/Ti/Au crystals (1 inch) were purchased from Infinicon. All other reagents were purchased from Sigma-Aldrich or Fisher Scientific Inc. and used without modification. All buffers were purified through 0.22 µM Millex®-GV filters and degassed under N<sub>2</sub> before use.

### *Synthesis of peptides*

All peptides were synthesized using standard Fmoc solid-phase synthesis methods using an APEX 396 peptide synthesizer on a Cys(Trt)-Wang resin. Cleavage was performed by mixing the functionalized resins with 2 mLs of a 90:5:3:2 ratio of trifluoroacetic acid:thioanisole:anisole:1,2-ethanedithiol) for two hours on an orbital shaker and precipitating the peptides in cold diethyl ether. Purification was performed using a reverse-phase HPLC (Waters Prep LC 4000) with a Waters 2487 dual wavelength detector and C18 column. The purified products were lyophilized and identified with MALDI-TOF mass spectrometry using a 20 mg/mL  $\alpha$ -Cyano-4-hydroxycinnamic acid (CHCA) matrix dissolved in a 1:1 v/v solution of acetonitrile and water.

### *QCM sensor assembly and peptide immobilization*

A Maxtek quartz crystal microbalance was the fundamental basis for peptide assembly and analyte recognition where the liquid-phase sensor assembly has been previously described (46,47). Verification of peptide immobilization onto gold was carried out using a 5 MHz quartz/chrome/Au crystal. First, a 5 MHz QCM electrode was soaked in Piranha solution (3:1 v/v ratio of concentrated H<sub>2</sub>SO<sub>4</sub> and 30% H<sub>2</sub>O<sub>2</sub>) for two minutes and rinsed with deionized water, ethanol, and water before being dried with N<sub>2</sub>. The Piranha-cleaned QCM electrode was then stabilized to its resonant frequency (5 MHz) under a 40 μL/min flow of 0.1 M (4-(2-hydroxyethyl)-1-piperazineethanesulfonic acid) (HEPES) buffer (pH 7.5). After stable frequency oscillations were achieved, peptide dissolved in HEPES was flowed over the electrode, followed by a final buffer wash in order to clear the surface of nonspecifically-bound peptide.

### *Electrochemistry*

Cyclic voltammetry was performed on a CH Instruments model 660A potentiostat. A Ag/AgCl (saturated KCl) reference electrode was coupled with a platinum counter electrode and Au working electrode. Respective voltammograms were taken in potassium phosphate buffer (pH 7.0) on a Piranha-cleaned gold surface and a gold surface containing immobilized target-binding peptides at a sweep rate of 0.1 V/s and an electrode contact area of 0.32 cm<sup>2</sup>.

### *Nitroaromatic target recognition*

First, a Piranha-cleaned 9 MHz QCM chip was immersed in a target-binding peptide solution overnight to promote monolayer assembly. The ensuing morning, the 9 MHz QCM chip was then rinsed with water and dried with N<sub>2</sub>. For nitroaromatic target recognition assays, a buffer solution containing 150 mM NaCl in 50 mM Tris-HCl (pH 7.5) was flowed over the electrode at 40 μL/min until a stable resonant frequency was established. In order to eliminate changes in frequency due to differences in solution viscosity, the buffer solutions contained the same concentration of acetonitrile as the target solution. Next, varying concentrations of nitroaromatic target solutions were flowed over the electrode before a final buffer wash to eliminate non-specific binding to the immobilized peptide.

## **Results and Discussion**

### *Peptide synthesis and immobilization onto Au*

The design of each recognition peptide provides a selective substrate for the detection of TNT, DNT, and TNB, where their sequences are denoted (Table 1). Each peptide begins with a cysteine amino acid at the C-terminus to promote Au-thiol bonding chemistry to the QCM substrate, followed by an octaethylene glycol spacer to not only protect the specific 12-mer recognition sequence from the gold surface, but to also provide a tightly-packed peptide monolayer. The 12-mer peptide recognition sequences specific for TNT, DNT, and TNB have been previously identified via multiple rounds of mutational phage display screening (39,40), but the selective discrimination of these three nitroaromatic explosive analytes has yet to be evaluated. Each recognition peptide is

terminated with aromatic residues, suggesting that electron donor-acceptor pi-pi stacking interactions are the dominant attractive forces. Also synthesized is a negative control peptide, which consists of a scrambled TNT-BP 12-mer sequence. The real-time adsorption of molecular recognition peptides and nitroaromatic targets can be easily detected and quantified with QCM, which dictates that the binding of adsorbed peptide or target is the difference between the final washed mass and the baseline mass.

Table 1. Sequences of molecular recognition peptides and their denoted abbreviations.

Biomimetic Recognition Peptide	Sequence (C to N)	Selective Target	Negative Control Targets
2,4,6-Trinitrotoluene-Binding Peptide (TNT-BP)	C-Peg <sub>8</sub> -I-S-V-P-M-L-P-R-Q-W-H-W		
1,3,5-Trinitrobenzene-Binding Peptide (TNB-BP)	C-Peg <sub>8</sub> -I-V-G-W-L-T-S-P-T-R-H-W		
2,4-Dinitrotoluene-Binding Peptide (DNT-BP)	C-Peg <sub>8</sub> -R-Q-H-L-I-Y-K-S-F-N-P-H		
Scrambled TNT-BP (Scram TNT-BP)	C-Peg <sub>8</sub> -H-I-W-Q-P-W-V-R-M-S-P-L	None	

In order to respectively quantify peptide immobilization using a liquid-phase QCM, 0.1 M HEPES buffer (pH 7.5) is flowed across the 5 MHz QCM gold surface at a constant flow in order to demonstrate that buffer does not bind to the gold. Next, a peptide solution dissolved in HEPES is flowed over the gold, where binding instantly

occurs, followed by a final buffer wash to remove non-specifically bound peptides (Figure 2A). Liquid-phase mass loading ( $\Delta m$ ) is determined by coupling the Sauerbrey equation with solution viscosity considerations from Glassford and Kanazawa,

$$\Delta m = -\frac{(\Delta R + \Delta f)A}{C_f},$$

where  $\Delta f$  is the change in frequency of the crystal's oscillations in Hz,  $A$  is the active electrode area ( $\text{cm}^2$ ),  $\Delta R$  is a resistance factor governed by solution viscosity, and the sensitivity factor ( $C_f$ ) for a 9 MHz crystal is  $0.181 \text{ Hz cm}^2 \text{ ng}^{-1}$  and  $0.566 \text{ Hz cm}^2 \text{ ng}^{-1}$  for a 5 MHz crystal (48-51).

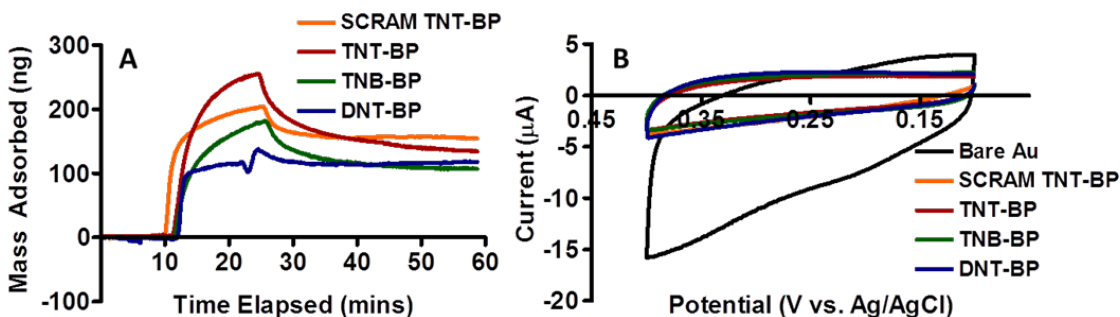


Figure 2. Quantitative and qualitative analyses of peptide adsorption onto a gold surface. (A) Peptide adsorption using 5 MHz QCM chips, where the surface is exposed to 0.1 M HEPES buffer (pH 7.5) for the first 10 minutes, followed by a 15 minute peptide adsorption flow in HEPES, and terminated by a 35 minute wash with buffer. (B) Cyclic voltammograms of Piranha-cleaned gold in comparison to immobilized recognition peptides on gold.

In terms of creating an effective sensor, it is important to be able to manipulate the immobilization of the recognition element in order to optimize the signal-to-noise ratio. It is observed that flowing different initial peptide concentrations over the gold surface yields adsorption of varying monolayer surface coverage. At lower immobilization

concentrations, individual peptides do not compete for gold binding sites, so that surface coverage is low and steric effects are limited. However, at very high concentrations, peptides are competitive for surface binding sites, which also leads to low surface coverage (Appendix B). Because peptide monolayer surface coverage is influenced by size and charge, every peptide forms a different self-assembled monolayer. Peptide immobilization is also qualitatively evaluated by adsorbing peptide solutions onto a gold electrode overnight and measuring the insulating capabilities of organics via cyclic voltammetry electrochemistry (Figure 2B). Since gold is an electrically conductive material, it has the ability to store charge, which is exhibited by the large 15  $\mu\text{A}$  total current difference for Piranha-cleaned gold. When an electrically insulating material such as an organic peptide blocks the surface, the gold loses its capacitance properties, as displayed by the narrow 5  $\mu\text{A}$  total current curves (i.e. current thickness) for adsorbed peptides (52). In comparison to a Piranha-cleaned gold surface, the total current decreases approximately by a factor of three for all immobilized peptides on gold electrodes, suggesting the successful adsorption of recognition peptides.

#### *Nitroaromatic target-binding assays*

For the purpose of quantifying peptide immobilization, a 5 MHz QCM chip is employed, while a more sensitive 9 MHz chip is utilized for the small nitroaromatic molecule-binding assays (Appendix B). The thinner 9 MHz QCM chip is able to oscillate faster, thus providing better sensitivity for the small nitroaromatic molecules. First, a 50 mM Tris-HCl buffer containing 150 mM NaCl and acetonitrile (pH 7.5) is flowed over the gold surface for the first five minutes to demonstrate that buffer molecules do not



adsorb to the peptide nor the gold surface. It is essential that the buffer contain the same concentration of acetonitrile as the target solutions in order to control for false positives attributed to changes in solution viscosity. Next, the nitroaromatic targets, TNT, TNB, and DNT, are flowed over a Piranha-cleaned gold surface, and although some non-specific binding occurs, no positive mass change is evident after buffer washes, indicating that none of the target molecules chemisorb to the surface in the absence of peptide (Figure 3).

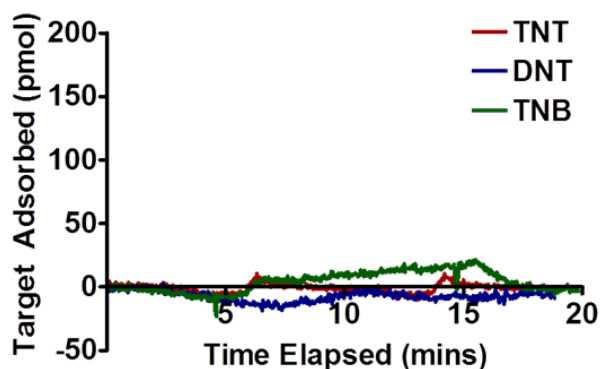


Figure 3. Nitroaromatic target adsorption to a Piranha-cleaned gold surface. For the first five minutes, 50 mM Tris-HCl buffer with 150 mM NaCl containing 11.35 v/v% acetonitrile is flowed over the gold surface, followed by a 500  $\mu$ M target flow for the next 10 minutes, and ending with a 5 minute buffer wash.

Initial nitroaromatic target recognition assays aimed for immobilizing the maximum peptide surface coverage onto the 9 MHz QCM chips. Since the sensor detects a mass adsorption, the rationale was that a greater peptide surface coverage would generate the highest signal. At immobilization concentrations of 500  $\mu$ M, 1000  $\mu$ M, and 200  $\mu$ M for TNT-BP, DNT-BP, and TNB-BP, their respective peptide surface coverage values: are 200 pmol/cm<sup>2</sup>, 275 pmol/cm<sup>2</sup>, and 300 pmol/cm<sup>2</sup> (Appendix B). When the

peptides are in such close proximity to each other, minimal nitroaromatic target binding occurs, most likely due to steric crowding and intermolecular peptide interactions (Appendix B). Although each peptide is positively charged at the N-terminus to provide repulsions between neighboring species, tightly packed terminal aromatic moieties attract each other, which could hinder target-binding regions if the peptides are too densely packed. In order to prevent intermolecular intrusion, the surface coverage of each peptide is reduced to approximately 125 pmol/cm<sup>2</sup> (Appendix B).

At the reduced monolayer surface coverage, there are enough peptides to generate an ideal signal-to-noise ratio because peptide steric effects are limited, freeing up target binding sites. The nitroaromatic targets are first manipulated as positive controls to quantify binding to their selective recognition peptides, followed by utilization as negative controls against all other recognition peptides (Figure 4). For each selective peptide, at a target concentration of 500 μM, its nitroaromatic molecule binding is greatest, while all target binding is greatly reduced when exposed to the negative control peptide, Scram TNT-BP. TNT, DNT, and TNB all exhibit reduced binding when exposed to their respective negative control peptides, confirming that the peptide sequence is responsible for selective recognition. Because the target molecules are so similar in structure, the selectivity of each peptide is evaluated (Figure 5). In order to quantify assay selectivity, nitroaromatic target binding to each biomimetic recognition peptide is normalized to the binding to Scram TNT-BP. All immobilized recognition peptides are titrated with their respective nitroaromatic targets (Figure 6), in which dissociation constants ( $K_D$ ) are calculated using previously described thermodynamic and kinetic models (Table 2) (46,47). TNT has the highest affinity to TNT-BP, as indicated by the

lowest  $K_D$  values, ranging from 29-44  $\mu\text{M}$ . TNB adsorption to TNB-BP has the next greatest affinity, ranging from 49-71  $\mu\text{M}$ , while DNT adsorption to DNT-BP has the lowest affinity, ranging from 81-137  $\mu\text{M}$ . The data suggests that TNT-BP is the most selective peptide, displaying the highest affinity to TNT and three-fold selectivity over DNT and TNB. Jaworski *et al.* demonstrate that after five rounds of mutational phage screening, the 12-mer sequence of TNT-BP is highly selective for TNT over DNT (39).

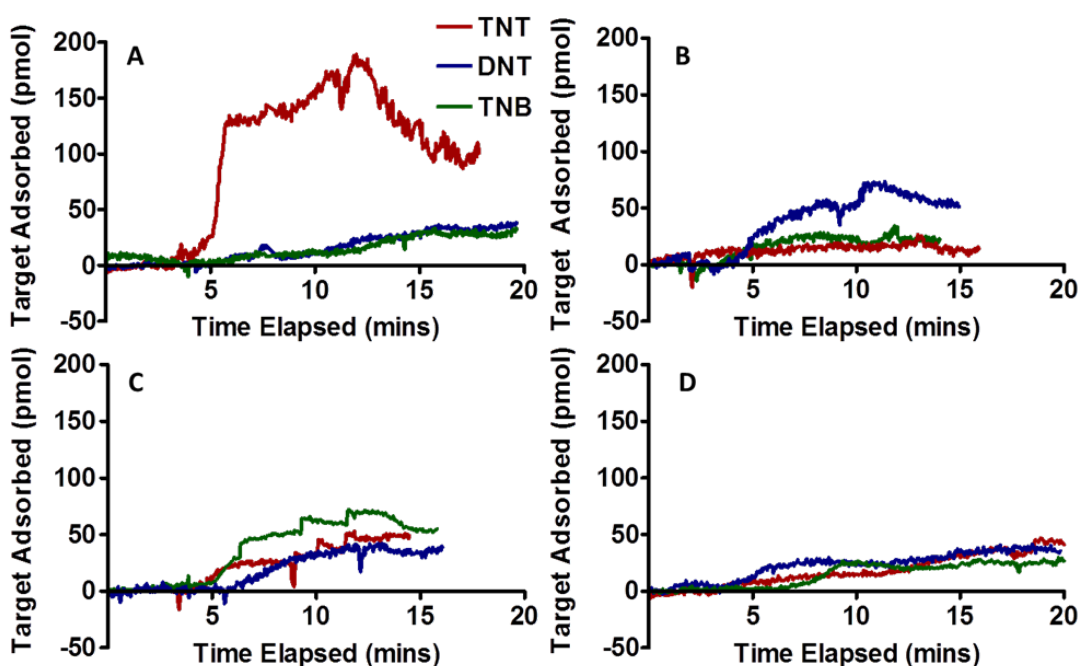


Figure 4. Nitroaromatic target adsorption to immobilized recognition peptides. Adsorption of 500  $\mu\text{M}$  TNT, DNT, and TNB when exposed to (A) 100  $\mu\text{M}$  immobilized TNT-BP, (B) 10  $\mu\text{M}$  immobilized DNT-BP, (C) 75  $\mu\text{M}$  immobilized TNB-BP, and (D) 100  $\mu\text{M}$  immobilized Scram TNT-BP. At these peptide immobilization concentrations, surface coverage for each peptide is approximately 125 pmol/cm<sup>2</sup>. A 50 mM Tris-HCl buffer (pH 7.5) containing 150 mM NaCl and 11.35 v/v% of acetonitrile is flowed over the electrode for the first five minutes, followed by a target flow, and a final buffer wash.

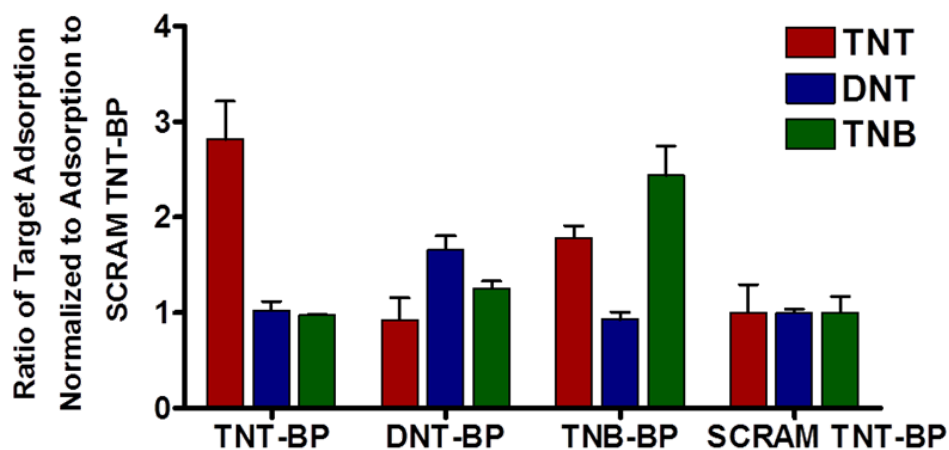


Figure 5. Selectivity of immobilized nitroaromatic recognition peptides. Ratios are calculated by normalizing the binding of each target to the negative control peptide, Scram TNT-BP.

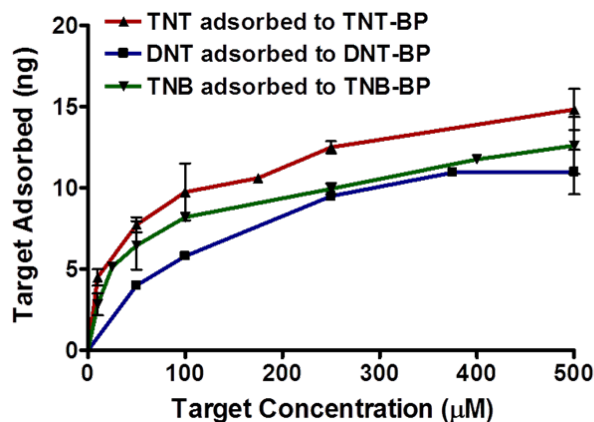


Figure 6. Titrations of nitroaromatic target adsorption to their respective recognition peptides.

Jaworski and coworkers do not screen for TNB affinity, but these results display that the lack of affinity of TNT-BP for TNB is comparable for its lack of affinity for DNT as well. The electron-rich N-terminal Trp-His-Trp motif in TNT-BP attracts the electron-

deficient aromatic TNT molecule, so that binding is dominated by pi-pi stacking interactions from the Trp residues, as shown by NMR studies between the aromatic motif and the TNT complex (44). It is also evident that hydrogen bonding contributes to the multivalent binding because Jaworski and coworkers show that substitution of the His residue in the terminal aromatic trimer decreases affinity for TNT (39). DNT-BP demonstrates a two-fold affinity for DNT over TNT, but still exhibits only 33 percent more selectivity for DNT over TNB. DNT is structurally less similar to its analogs, lacking a nitro group at the 6-carbon position relative to TNT. As a result, the aromatic ring of DNT contains more electron density than the rings in TNT and TNB. It is not surprising that the terminal residues in DNT-BP contain less electron-dense moieties than in TNT-BP and TNB-BP, proposing that pi-pi stacking interactions may not be the dominant attractive forces. DNT-BP contains a Phe-Asn-Pro-His N-terminal motif, suggesting that the Asn and His residues can contribute to hydrogen bonding, while the Phe ring contributes to pi-pi stacking interactions.

**Table 2.** Calculation of dissociation constants ( $K_D$ ) of nitroaromatic target molecules adsorbed to selective recognition peptides using Langmuir isotherm and kinetic models.

Target/Peptide System	Langmuir Isotherm Model ( $\mu\text{M}$ )	Time Constant Kinetics Model ( $k_r/k_f$ ) ( $\mu\text{M}$ )
TNT Adsorption to TNT-BP/Au	$44 \pm 13$	$29 \pm 5$
TNB Adsorption to TNB-BP/Au	$49 \pm 14$	$71 \pm 19$
DNT Adsorption to DNT-BP/Au	$137 \pm 48$	$81 \pm 38$

TNB-BP indicates selectivity for TNB over DNT by a factor of 2.5, but the peptide also has a remarkably high affinity for TNT. TNB-BP only undergoes three rounds of phage display screening by Goldman *et al.* to originally bind TNB, but it is also noted that the 12-mer recognition sequence also elicits an affinity for TNT. TNB-BP contains a very similar N-terminal trimer sequence (Trp-His-Arg) relative to TNT-BP, with the only exception pertaining to an Arg residue substituted for a Trp at the third to last amino acid. Although the only structural difference between TNT and TNB is the substitution of a methyl group at the 1-position in TNT for a hydrogen atom in TNB, the inductive effect dictates that the aromatic ring in TNB is more electron-deficient than in TNT. The larger induced dipole in the nitro groups in TNB can undergo ion-induced dipole interactions with the positively charged guanidinium group in arginine. TNB-BP still contains Trp and His residues to promote respective pi-pi stacking and hydrogen bonding interactions with TNT.

## Conclusions

In this work, the successful biomimetic sensor platform for the selective detection of TNT and discrimination between its analogs, DNT and TNB, using a piezoelectric sensor platform without the dependence on signal enhancement methods is demonstrated. The detection system identifies adsorption through a mass change, and since TNT is the heaviest nitroaromatic molecule investigated in this study, TNB and DNT by default exhibit 6 percent and 20 percent less signal, respectively. The biomimetic recognition sequences specific to each nitroaromatic target suggest that multivalent binding events occur, consisting of pi-pi stacking, hydrogen bonding, or ion-induced dipole interactions.

The real-time recognition capabilities of the QCM sensor design coupled to biomimetic peptide technology provide platforms for future sensors in the transportation industry, polluted areas, and combat zones.

### **Section Acknowledgements**

This work was funded by the Defense Threat Reduction Agency (DTRA) and Vanderbilt University. I would especially like to thank Prof. David Wright for his guidance and mentorship pertaining to this work, along with the opportunity to present this work at a conference (DTRA Chemical and Biological Defense, Science & Technology Conference, November, 2011, Las Vegas, NV). I would also like to thank the collaborating PI's on this project with respect to their suggestions, guidance, and mentorship during the DTRA meetings: Prof. Richard Haglund, Prof. David Cliffler, and Prof. Sokrates Pantelides. I would also like to thank others who have worked on the DTRA project for their support and mentorship: Dr. John Stone, Dr. Krishen Appavoo, Dr. Joyeeta Nag, Dr. Bin Wang, Dr. Jed Ziegler, Keith Warnick, Matthew Bryant, Matt Casey, Joe Keene, and Alex Raubach. Finally, I would like to thank Dr. Josh Swartz for assistance with peptide synthesis and Dr. Stephen Jackson for assistance with the QCM instrument operation.

## Chapter III

### ELECTROCHEMICAL DETECTION OF 2,4,6-TRINITROTOLUENE AT COLLOIDAL GOLD NANOPARTICLE FILM ASSEMBLIES

#### **Abstract**

This chapter investigates citrate-capped, colloidal gold nanoparticle (AuNP) film assemblies of varying particle sizes (5-50 nm) to serve as platform electrochemical sensors to simultaneously detect and reduce TNT to 2,4,6-triaminotoluene (TAT) in solution (53). The high surface area-to-volume ratio of colloidal AuNPs offers applications in electrocatalysis, while the facile immobilization onto a variety of substrates provides rapid and reproducible platform technologies. In order to validate these AuNP film assemblies as electrocatalytic platform sensors, square wave voltammetry is performed to enhance TNT sensitivity and optimize the signal transduction of TNT reduction. Upon TNT reduction on 15 nm AuNP films, the highest sensitivity is observed with nanomolar limits of detection. The formal reduction potential also undergoes a 35 mV shift to more positive potentials in comparison to controls, suggesting that 15 nm AuNPs demonstrate catalytic properties in this application. It is hypothesized that the 15 nm AuNP film assemblies store charge more efficiently because of their large dielectric constant values and capacitance measurements compared to AuNP films of alternative sizes. Additionally, the onset potential shifts nearly 70 mV more positive for 5 nm, 15 nm, and 30 nm AuNP film assemblies, indicating that TNT



begins its reduction process at a lower energy when these particles are assembled on Au substrates compared to controls.

## **Introduction**

The previous chapter delved into the selective detection of nitroaromatic small molecules at a bulk gold substrate electrode. Although specific detection was achieved using the recognition peptide/Au platform, explosives detection was not sensitive enough to be applicable for field-testing and further development. Additionally, the QCM sensor chips correlate to approximately \$5.50/experiment, assuming each chip is used 10 times. However, the real-time binding kinetics generated by the quartz crystal microbalance (QCM) instrument provides the rapid detection timeframes necessitated for environmental and field applications. As described in the previous chapter, a mass-loading event at a chip surface is responsible for decreasing the frequency of sensor oscillations, which subsequently generates an electrochemical response, driving signal transduction. Although the QCM platform cannot detect small explosive molecules in a sensitive manner, this chapter focuses on using an alternative electrochemical detection strategy to not only maintain the rapid sensing element from cheap materials, but to also enhance the signal generated by TNT identification.

Many biosensors, microfluidics, and lab-on-a-chip devices are developed with electrochemical detection readouts because of the rapid response times for analysis and the sensitive detection strategies. Most traditional electrochemical schemes employ a three-electrode system comprising of a reference, counter, and working electrode (52). While the reference electrode standardizes known potentials, the counter electrode acts as

a cathode to assist in current flow between the working electrode and the buffer system. Its reduction potential also conveniently falls outside of the range of most chemical reactions. Most importantly, the working electrode bridges the gap between electricity and chemistry in order to probe reaction kinetics and thermodynamics at a conductive solid-water interface. Signal transduction is generated as a current output and is measured between the working and counter electrodes. However, innovative materials and approaches are essential to enhance signal transduction capabilities in biosensors and microfluidics, so that detection schemes can be universally applied.

As shown in the previous chapter, the conductive nature of gold drives the piezoelectric sensing of a QCM, while the facile self-assembly properties contribute to manipulation at the molecular level (16-19). Gold retains higher conductivity values compared to alternative substrates, contains a large anodic potential range, and can be manufactured very easily (54). In terms of platform sensor development, it is essential for electrons to be effectively shuttled between the electrode-buffer interfaces for optimum signal transduction, but one of the primary drawbacks using gold electrodes is the high background signal (55). To alleviate these issues, organothiolates have been utilized as insulators on gold electrodes to mask the high currents in order to study the redox activity of the metalloproteins, cytochrome c and azurin (56-64). Although adequate signal is provided to study the redox properties of these proteins, the insulating properties of organic thiols often compromises electron transfer kinetics and the signal is reduced. Leopold and coworkers have addressed these issues by adsorbing small monolayer-protected AuNP clusters onto SAMs in order to facilitate the electron transfer kinetics and thermodynamics of cytochrome c and azurin redox proteins (65,66). The high-

dielectric AuNP film assemblies provide a conductive substrate to perform electrochemical reactions, but also minimize background current in comparison to a clean gold substrate. It is hypothesized that electrons slowly tunnel through the low-dielectric (i.e. insulating) organic SAMs, while electrons rapidly hop from nanoparticle to substrate in the AuNP film assemblies, so that the signal is transduced rapidly (66). Leopold further investigates the electrochemical properties of AuNP film assemblies by employing citrate-capped, colloidal particles as a H<sub>2</sub>O<sub>2</sub> sensing platform (67). The large volume AuNP increases the sensitivity of the platform, while the dense monolayer reduces background noise. In addition, this simple and rapid film assembly procedure takes advantage of stable, aqueous materials to offer low synthetic costs.

This chapter exploits the electrochemical and physical properties of electrostatically-bound, colloidal AuNP film assemblies in order to detect TNT using voltammetric techniques. The explosive TNT possesses three known electrochemical reduction peaks, each of which is representative of the 6e<sup>-</sup>/6H<sup>+</sup> reduction process from a nitro to an amine group (68). The energy of surface electrons in AuNPs is significantly higher in comparison to bulk gold, so that it is hypothesized that these films can exhibit electrocatalytic properties with smaller particles, hereby increasing the reduction potentials of TNT and lowering the energy required to reduce the analyte in solution. This chapter elucidates the nanoparticle size dependence on autocatalysis and analytical sensitivity of electrochemical TNT detection at these films.

## Materials and Methods

### *Reagents*

2,4,6-trinitrotoluene (TNT) was purchased from Cerilliant Corporation at a stock concentration of 1000 ppm dissolved in acetonitrile. Citrate-stabilized AuNPs (15 nm, 30 nm, 50 nm) were purchased from Ted Pella, Inc. 5 nm citrate-stabilized AuNPs were purchased from NANOCS. Poly-L-Lysine (PLL) and 11-Mercaptoundecanoic acid (MUA) were purchased from Sigma-Aldrich. All other reagents were purchased from either Sigma-Aldrich or Fisher Scientific and used without further modification. All deionized water used in this investigation was filtered through a 0.22  $\mu\text{m}$  filter at a resistance of 18.2  $\text{M}\Omega\cdot\text{cm}$ .

### *Instrumentation*

Electrochemistry was performed on a CH Instruments potentiostat with Chi660A analysis software. Surface UV-vis spectra were collected on a Varian Cary 5000 UV-vis-NIR spectrophotometer. Liquid-phase UV-vis measurements were performed on an Agilent 8453 spectrophotometer with a photodiode array detector. In order to probe surface topography, a Veeco Dektak 150 profilometer equipped with a diamond-tipped stylus was utilized. Images of AuNPs were captured with a Tecnai Osiris transmission electron microscope. Images of suspended AuNPs were captured with an iPhone 4S camera.

### *AuNP film assembly*

Unmodified gold substrates evaporated on silica wafers were first Piranha-cleaned (3:1 v/v ratio of concentrated H<sub>2</sub>SO<sub>4</sub>: 30% H<sub>2</sub>O<sub>2</sub>) for 30 minutes and washed thoroughly with water. Next, a 5 mM MUA solution in ethanol was assembled overnight on the gold substrates. After washing with ethanol and water, the MUA-functionalized gold was immersed in a 1 mg/mL poly-L-lysine (PLL) solution for 20 minutes. After washing with water, the gold films were immersed in stock solutions of citrate-stabilized AuNPs (15 nm, 30 nm, 50 nm) for one hour and subsequently washed with water. They were further stored in aqueous solutions to preserve their stability. For the assembly of 5 nm AuNPs, the particles were spun down for 99 minutes at 16,100 gs one time and resuspended in 10 mM Tris buffer. The particles were then drop-cast and allowed to dry on the MUA-PLL/Au substrate overnight. The subsequent morning, they were washed thoroughly with water.

### *Electrochemical cell*

The AuNP film immobilized on a Au substrate served as the working electrode ( $A = 0.2 \text{ cm}^2$ ), a Pt wire served as the counter electrode, and a Ag/AgCl (sat. KCl) reference electrode comprised the electrochemical cell. The buffer was comprised of phosphate buffer with 100 mM KCl.

### *Double layer capacitance measurements*

Using the electrochemical cell described above, capacitance measurements were performed using cyclic voltammetry and scanning from +0.1 and +0.4 V vs. Ag/AgCl (beginning at +0.1 V) at a scan rate of 0.1 V/s in the aforementioned phosphate buffer.

### *Detection of 2,4,6-Trinitrotoluene at AuNP film assemblies*

Electrochemical detection of TNT was performed using square wave voltammetry between -0.2 and -0.9 V vs. Ag/AgCl at a step potential of 4 mV, an amplitude of 25 mV, and a frequency of 15 Hz. TNT was dissolved in phosphate buffer containing 0.1 M KCl and 2.2% v/v acetonitrile (pH = 7.0). Background measurements consisted of phosphate buffer with 0.1 M KCl containing 2.2% v/v acetonitrile. TNT measurements were background-subtracted for optimized sensitivity.

## **Results and Discussion**

### *Stability and monodispersity of colloidal AuNPs*

The incorporation of a AuNP film adsorbed to a layer of poly-L-lysine (PLL) provides a facile and rapid electrode assembly process exploiting electrostatic interactions from low-cost materials. Leopold *et al.* have assembled AuNP films on Au electrodes for enhanced electron transfer kinetics, but the catalytic activity of these assemblies has never been investigated (65-67). In order to optimize the AuNP film for both sensing and catalysis, four different AuNP sizes are examined between 5-50 nm. There is a direct correlation between nanoparticle diameter and the ability to absorb light, as the molar absorptivity is directly proportional to the molecule or particle surface area.

However, smaller particles contain a larger percentage of surface electrons, which possess a proclivity for catalysis.

When suspended in aqueous buffers, the citrate particles demonstrate stability and monodispersity, as indicated by the captured TEM images, narrow plasmon resonance band in the UV-vis spectra, and bright red colors (Figure 7). These aqueous, monodisperse particles serve as ideal building blocks for rapid and reproducible sensor development.

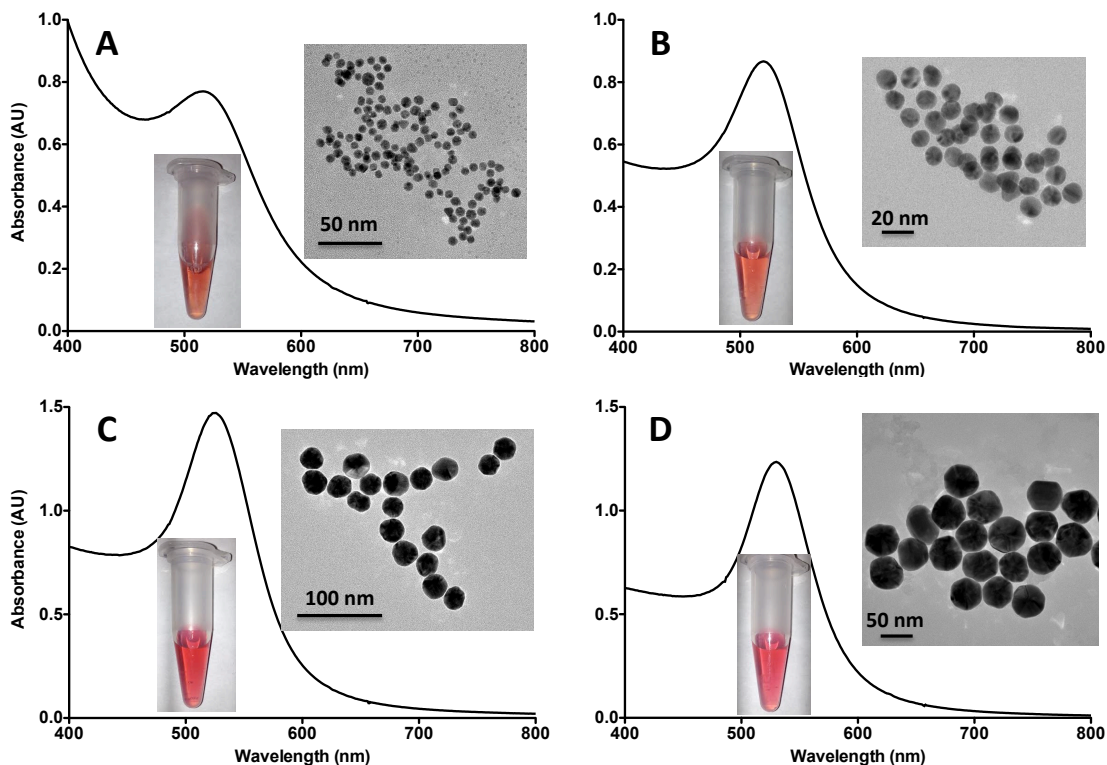


Figure 7. Characterization of colloidal suspensions of citrate-capped AuNPs. UV-vis spectra, TEM images, and photographs of suspended AuNPs of (A) 5 nm, (B) 15 nm, (C) 30 nm, and (D) 50 nm AuNPs.

### *AuNP film assembly and characterization*

The synthesis of the film is carried out according to the procedure elucidated by Schmidt *et al.* (67). Each gold substrate is first exposed to a fresh solution of Piranha for 30 minutes, which essentially oxidizes all of the organic molecules adsorbed on the surface, increasing their water solubility and desorbing them from the surface. Next, a mercaptoundecanoic acid (MUA) alkanethiol is incubated with the clean gold for two days in order to assemble a stable monolayer on the surface (Figure 8). Afterwards, a positively charged poly-L-lysine polymer (1 mg/mL) is incubated with the MUA/Au film for 20 minutes before incubating a stock solution of negatively charged, citrate-stabilized colloidal AuNPs for one hour.

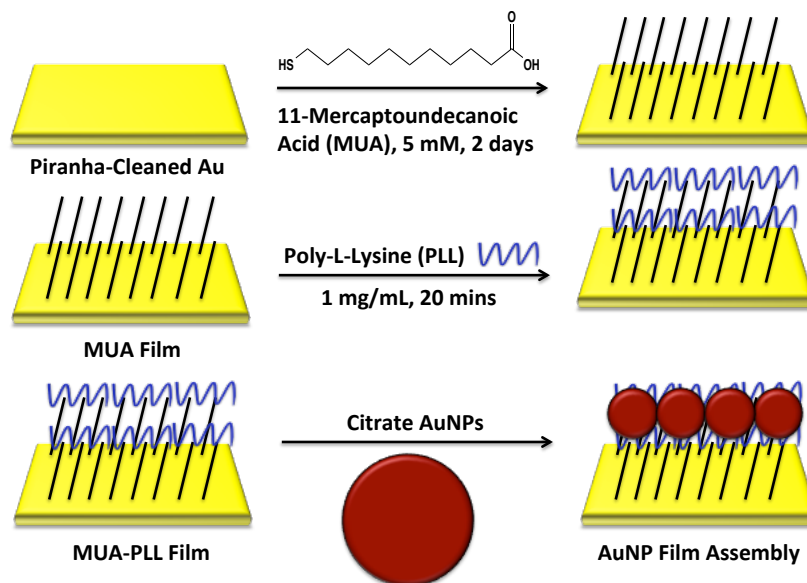


Figure 8. Assembly of citrate-capped AuNP films on Au substrates.

Film characterization is first carried out electrochemically by treating the AuNP assembly like a capacitor. This can be performed using cyclic voltammetry to measure



the background current (i.e. non-Faradaic current) at a potential range where little redox activity occurs. The potential range is first scanned from +0.1 to +0.4 V vs. Ag/AgCl at each electrode system (Figure 9). First, it is interesting to note that a clean gold substrate possesses a high background current with significant variability, as indicated by the large error bars. Additionally, a reduction peak and an oxidation peak are both evident on bare Au, which correlates to water splitting at the electrode surface. With no material to mask natural interferents at the electrode surface, analytes such as water and oxygen can easily diffuse to the electrode, which contribute to the high background current. When organic insulating molecules such as MUA-PLL are adsorbed to gold, the capacitance decreases significantly with little variability, as indicated by the small error bars and the small total current measurements. Additionally, water splitting redox peaks are not observed because the SAM creates a dense molecular blocking layer, shielding background effects of interfering analytes. When the AuNPs are adsorbed to the MUA-PLL/Au substrates, the total current (i.e. current thickness) increases inversely proportional relative to particle diameter. The 50 nm AuNP film assemblies display identical total current values relative to the organic MUA-PLL. However, as particle size decreases, the total current increases. Assemblies of 15 nm and 5 nm AuNP films, respectively, possess similar background currents, which suggests that there may be a threshold maximum non-Faradaic current for these colloidal film assemblies. Nonetheless, the AuNP films (5 nm, 15 nm, and 30 nm) exhibit an ability to store charge in a larger capacity relative to films of MUA-PLL and 50 nm AuNPs, while also simultaneously masking the surface from interfering analytes such as water and oxygen.

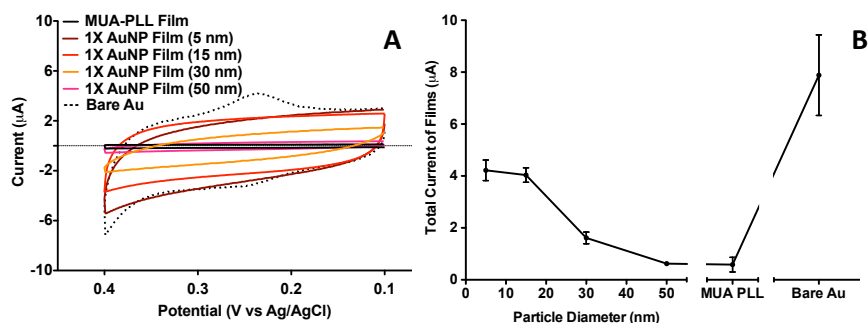


Figure 9. Electrochemical capacitance measurements of various AuNP film assemblies. (A) Representative cyclic voltammograms of AuNP film assemblies, MUA-PLL film, and a bare Au electrode from +0.1 to +0.4 V vs. Ag/AgCl at a scan rate of 0.1 V/s and an electrode area of 0.2 cm<sup>2</sup>. (B) Total current of each film or current thickness from the cyclic voltammograms obtained for each of the electrode assemblies performed in triplicate.

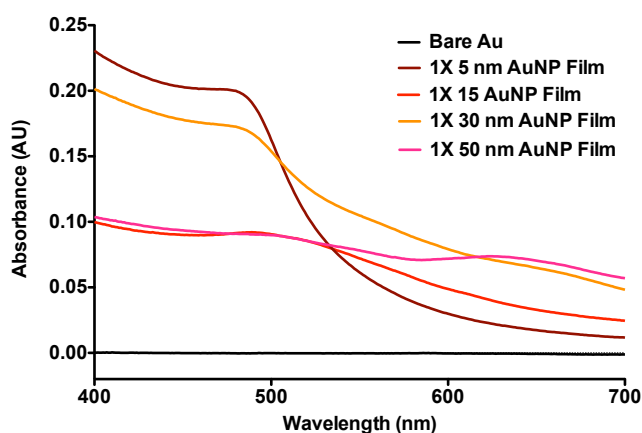


Figure 10. Surface UV-vis spectra of AuNP film assemblies.

In order to further probe the AuNP assembly characteristics of this platform sensor, surface UV-vis spectra are generated to understand how the particles behave at the gold surface (Figure 10). The 5 nm, 15 nm, and 30 nm AuNP films exhibit a localized SPR peak near 500 nm, which correlates to their SPR peak upon suspension in an aqueous solution. This indicates that not only are the particles adsorbed to the film, but they also maintain their monodisperse, catalytically active nature. In contrast, the 50 nm AuNP film assemblies possess two peaks, one at 500 nm and an additional at 625 nm.

The presence of the additional peak indicates that the particles undergo some level of aggregation at the electrode surface, which most likely is attributed to their small current thickness and weak overall capacitance, similar to that of an organic SAM. The monodisperse nature of AuNPs drives their fascinating chemical and physical properties, so that upon aggregation, the particles veer towards the banal optical and catalytic characteristics of the bulk material. Additionally, film thickness measurements of the assemblies via profilometry reveal that the exploitation of the non-specific electrostatic adsorption of AuNPs does not create a single monolayer of particles at the electrode surface. For 5 nm, 15 nm, 30 nm, and 50 nm AuNPs assemblies, the film thicknesses are: 80 nm, 100 nm, 150 nm, and 150 nm, respectively. These results indicate that during the electrostatic adsorption process, the particles are non-specifically stacking on top of each other, which creates a thicker film than originally intended and a long-range electron transfer material.

#### *Electrochemical detection of TNT using platform AuNP film assemblies*

Previous electrochemical strategies have developed complex, expensive electrodes for TNT detection, including but not limited to: boron-doped diamond, graphene supports, and innovative carbon-based supports (69-72). Since bulk gold substrates in addition to nanoparticles have been so heavily investigated since the 1980's, this accessible material provides a sensing platform with commercially available materials at low purchasing costs. In order to determine the performance of these films, electrochemical TNT reduction is probed at each film assembly. The electrochemical technique, square wave voltammetry (SWV), is investigated because it provides better

sensitivity than alternative voltammetry and polarography techniques. The ubiquitous cyclic voltammetry technique generates constant forward and reverse scans between two potentials, generating a single current value for each scanned potential value. As described by Bard and Faulkner, SWV contrastingly measures current two times per cycle in the forms of a forward and reverse current (52). These values are subtracted from one another to yield a difference current, often resulting in better analyte sensitivity due to suppressed noise.

Varying concentrations of TNT are first titrated in the buffer system using the film assemblies as a working electrode and subsequently measured electrochemically with SWV (Figure 11). Although bare Au displays a high current output at 100  $\mu\text{M}$  TNT concentrations, only one peak is resolved due to the high background noise. Reduced species of TNT can easily diffuse to the electrode, because bare Au is completely exposed to the buffer medium. On the other hand, molecular oxygen ( $\text{O}_2$ ) attributes significantly to background noise at high TNT concentrations, as the broad peak shape does not follow a Gaussian distribution. Below 10  $\mu\text{M}$  TNT at a bare Au surface, no reduction peaks are observed because the TNT signal is masked by high background species.

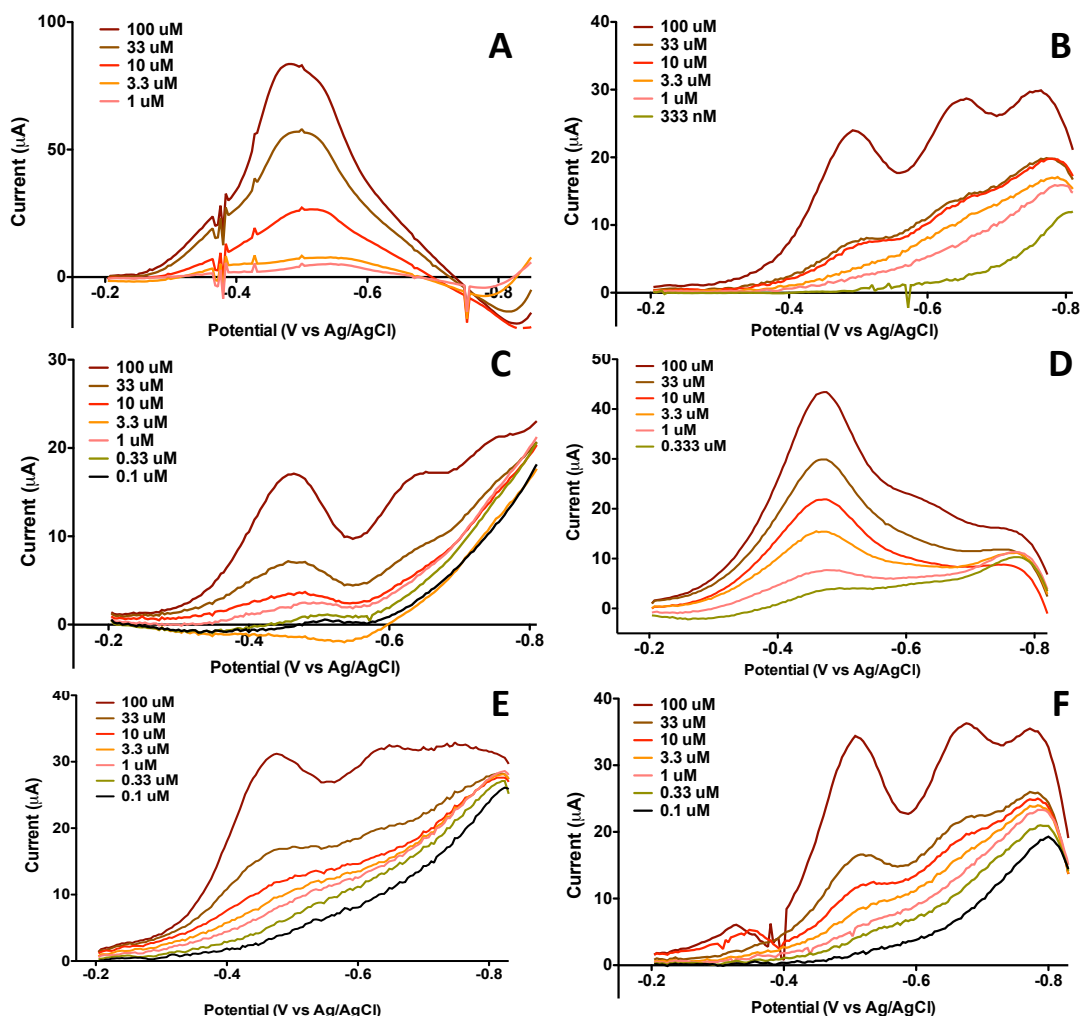


Figure 11. Titrations of TNT measured via square wave voltammetry at (A) Bare Au, (B) MUA-PLL, (C) 5 nm AuNP film assembly, (D) 15 nm AuNP film assembly, (E) 30 nm AuNP film assembly, and (F) 50 nm AuNP film assembly.

Contrastingly, at a MUA-PLL organic film, background current is almost entirely suppressed, generating excellent three-peak resolution at high TNT concentrations, each one representative of the  $6e^-/6H^+$  reduction from a nitro to amine group (Figure 11B). However, at the lower concentrations, current output decreases significantly, most likely due to the weak electron tunneling effects through organic insulating molecules. It is also interesting to note that the peak height intensity is smaller with every subsequent

reduction peak, as the stability of each reduced species becomes increasingly weaker. Upon adsorption of colloidal AuNPs, at high TNT concentrations, all three reduction peaks are observed (Figures 11C-F). The first reduction peak is especially evident below 1  $\mu$ M TNT in the 5 nm and 15 nm AuNP assemblies, while the 30 nm and 50 nm AuNP films exhibit visible peak heights down to 1  $\mu$ M. Additionally, sensitivity also increases when the AuNPs are adsorbed to gold substrates (Figure 12). The fact that sensitivity increases at the AuNP films refutes the electron tunneling mechanism through these films and supports the electron hopping mechanism. The electrons are shuttled on the order of 100 nm at the AuNP assemblies in comparison to less than a 5 nm distance with bulk Au and organic SAM films. It is also observed that the 15 nm AuNP films exhibit the greatest sensitivity, which challenges my hypothesis. I originally hypothesized that the 5 nm AuNP films would display the highest sensitivity because the particles possess the largest relative surface area and a higher relative concentration of high-energy surface electrons. The high surface energy of the 5 nm AuNP film assemblies would therefore shuttle electrons more efficiently. However, the 15 nm AuNP films exhibit the highest saturated signal and sensitivity, offering a detection limit of 336 nM, approximately two orders of magnitude greater than TNT detection via the QCM instrument. The 5 nm AuNP films also demonstrate high nanomolar limits of detection, but with lower sensitivity and signal-to-noise. Further investigations are necessitated to identify the packing of these particles, as the 15 nm AuNPs may pack more favorably than the 5, 30, and 50 nm AuNPs.

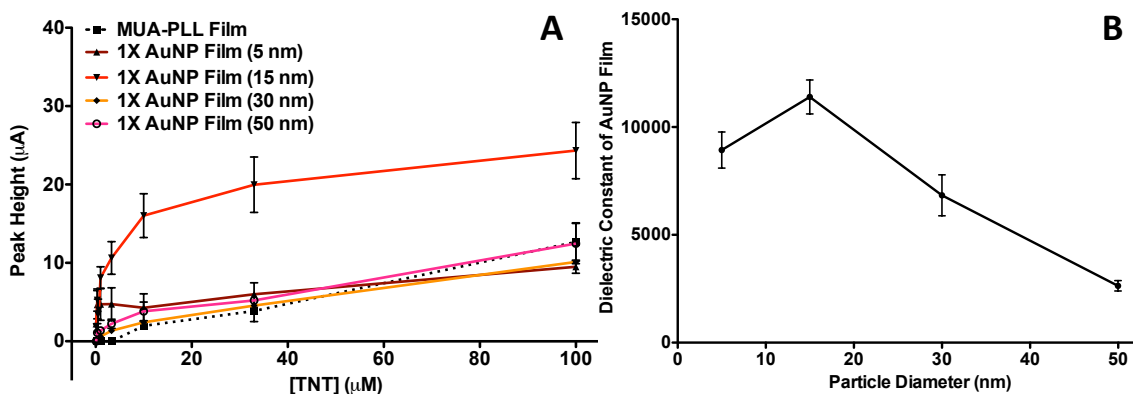


Figure 12. AuNP film assembly sensor performance. (A) TNT titrations as a function of the first reduction peak height and (B) calculation of a theoretical dielectric constant for each AuNP film.

After further investigations of the TNT titrations, the capacitance data of these films was revisited. The 5 and 15 nm AuNP films exhibit high double layer capacitance values, meaning they can store charge efficiently. This value can be calculated by modeling these films after a double-plate capacitor, so

$$C_{dl} = \frac{I_{Tot}}{2 \cdot \nu} = \frac{A \cdot \epsilon \cdot \epsilon_0}{d},$$

where  $C_{dl}$  is the double-layer capacitance in Farads,  $I_{Tot}$  is the total current or current thickness value (Amps),  $\nu$  is the cyclic voltammetry scan rate (V/s),  $A$  is the electrode area ( $\text{cm}^2$ ),  $d$  is the film thickness (m),  $\epsilon_0$  is the vacuum permittivity of free space constant, and  $\epsilon$  is the dielectric constant of the material (52,65,73,74). The values  $I_{Tot}$  and  $d$ , are measured experimentally via cyclic voltammetry and profilometry, respectively. After substituting these values into the above equation, the value for dielectric constant can be solved. It is interesting to note that the 15 nm AuNP films exhibit the highest dielectric constant, which suggests better charge storing capabilities than any other particle assembly (Figure 12B). The 5 nm and 30 nm AuNP films exhibit similar

dielectric constant values, while the 50 nm AuNP film exhibits the lowest dielectric constant. This can be attributed to the large particle's poor assembly and aggregation properties at the electrode surface, as determined by surface UV-vis analysis. However, this also could suggest that there is a size-dependent aspect for particle packing efficiency using this experimental design.

#### *Catalytic properties of AuNP film assemblies*

After evaluating the sensing properties of the AuNPs via TNT titrations, it is observed that the reduction peaks across each film assembly are not uniform. At MUA-PLL electrodes, the formal potential of the first reduction peak occurs at -500 mV vs. a Ag/AgCl reference electrode, while the reduction peak presents itself at -490 mV at bare Au. In conventional electrochemistry, higher free energy corresponds to more negative potentials, while a lower free energy corresponds to more positive potentials. If a reduction occurs at more positive potentials, a smaller amount of energy is required to electrochemically reduce the analyte of interest, which is indicative of catalysis. This is not surprising because MUA-PLL films are significantly more insulating compared to bare Au, so more energy is required to reduce TNT at the insulating SAMs. However, as AuNPs are adsorbed to the film, the formal potential of TNT reduction shifts in a more positive direction, requiring a smaller amount of energy to reduce TNT.

There are reported studies elucidating size-dependent catalytic applications of AuNPs, but TNT catalysis at AuNP films has never been investigated (75-78). Also interesting to note is that there are conflicting reports of AuNP size-dependence, suggesting that catalysis is application-specific. I hypothesized that the 5 nm AuNP film



would generate the largest catalytic activity (i.e. largest positive shift in reduction potential) because these particles contain the highest amount of relative surface atoms compared to the larger particles. My original hypothesis is supported only in terms of the formal potential shift, because at saturated concentrations of TNT, the formal reduction potential increases up to 50 mV to more positive potentials relative to MUA-PLL films as particle size decreases (Figure 13). To put these values in perspective, the reduction potentials of the first TNT peak at 5 nm and 15 nm films are more positive than previously mentioned boron-doped diamond and carbon electrodes.

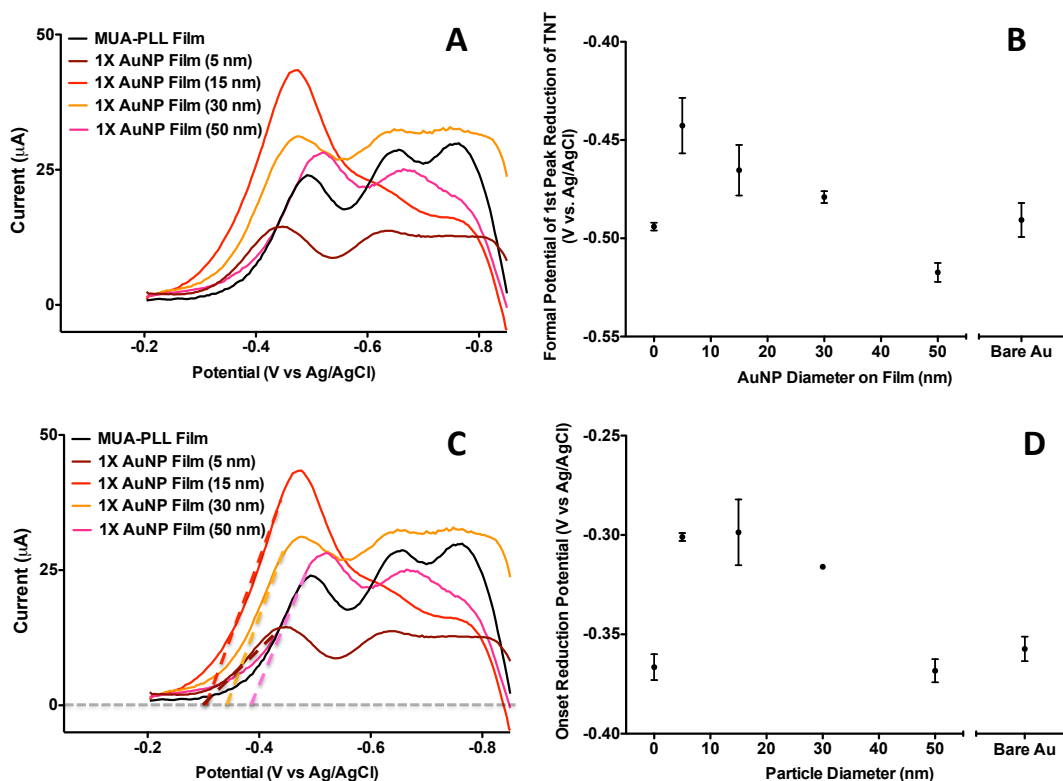


Figure 13. Catalytic performance of AuNP film assemblies in the presence of 100  $\mu\text{M}$  TNT. (A) Square wave voltammograms of at various assemblies, (B) Formal reduction potential of first TNT peak, (C) Visual representation of calculation of onset potential for the first reduction peak of TNT. A line is fitted to the peak shape of reduction and the value of the x-intercept denotes the onset potential. (D) Plot of onset reduction potential of first TNT peak as a function of particle size. (0 diameter particle size corresponds to MUA-PLL film).

Although positive peak shifts are evident, the formal reduction potential may not be the best indicator of electrocatalysis because the peak intensities are not uniform across the AuNP films. The calculation of onset reduction potential is a better indicator of catalytic activity because at this potential, the analyte begins its electrochemical reduction process. By fitting a line to the peak shape of the reduction peak and subsequently solving for the value of the x-intercept, onset reduction potential can be determined for each AuNP film assembly (Figures 13C-D). At 5 nm, 15 nm, and 30 nm AuNP film assemblies, the onset reduction potentials of TNT are similar, shifting approximately 70 mV more positive relative to bare Au and MUA-PLL controls. The 50 nm AuNP film shows an insignificant shift in onset potential and zero catalytic activity, which suggests that particles of that size do not assemble well onto the gold. Between 5 nm and 30 nm, colloidal AuNP assemblies act as catalysts for electrochemical TNT reduction because of their high surface energy due to their monodisperse nature after assembly.

## **Conclusions**

Herein, this chapter describes the facile platform sensor development for TNT detection using cheap, stable AuNPs with a facile electrostatic adsorption assembly. The particles demonstrate two functions: creating a blocking layer similar to a SAM to shield non-specific signal effects but to also maintain conductivity like the bulk Au counterpart. At 5 nm, 15 nm, and 30 nm AuNP film assemblies, electrocatalysis is evident by the shifts in reduction formal potential and onset potential of the first TNT peak. A ‘sweet spot’ also emerges concerning nanoparticle diameter in assembling these films, as the 15 nm AuNP films exhibit the highest sensitivity, lowest limits of detection, most positive

onset reduction potential, and largest calculated dielectric constant. Although further investigation is needed, it is hypothesized that the stable 15 nm particles can pack more efficiently at the gold surface due to its high dielectric constant. The 5 nm, 15 nm, and 30 nm AuNP assemblies also require less energy to electrochemically reduce TNT, with more positive reduction potentials compared to previously published glassy carbon, boron-doped diamond, graphene, and graphite electrodes. Additionally, there may be a threshold size related to nanoparticle stability at these films, as the 50 nm AuNPs show onsets of aggregation and zero catalytic activity. There may also be a threshold particle size that supports the ‘electron hopping’ mechanism. Nonetheless, the innovation inspired by utilizing cheap materials has the ability to streamline sensor development for a wide variety of analytes, in addition to offering novel catalysts at solid interfaces and in synthetic reactions.

### **Future Directions**

The QCM chapter investigates a very specific molecular recognition platform sensor, while the platform sensor described in this chapter is non-specific. One strategy to improve both sensitivity and specificity in the format described in this chapter would be to incorporate recognition elements with the AuNPs for improved capture at the electrode-liquid interface. The successful capture of nitroaromatics using recognition ligands at the electrode interface provides an initial pre-concentration mixing step without instrumental bias. To also enhance sensitivity, an electrochemical bias can be performed by holding the electrode at constant positive or negative potentials for upwards

of two minutes. This allows for all of the dissolved analyte to be attracted to the electrode, increasing sensitivity but also increasing noise.

One of the most important aspects of TNT sensor development is the successful transition between detection in the liquid phase and the gas phase. The vast majority of references mentioned in these chapters have developed platform sensors for TNT detection in solution, because it is significantly easier compared to gas-phase detection. While nitroaromatics such as 1,3,5-trinitrobenzene, 1,3-dinitrobenzene, and 2,4-dinitrotoluene possess relatively high vapor pressures, the vapor pressure of TNT is two orders of magnitude lower than its analogues. The low vapor pressure of TNT immensely complicates many detection strategies, so that pre-concentration or priming steps are necessitated. In order to increase the volatility of this small molecule, TNT must be heated significantly to increase its vapor pressure. Fortunately, TNT is stable at high temperatures, as its detonation temperature is upwards of 200°C.

In the past couple of years, a group developed a gas-phase detection strategy for pre-concentrating TNT and identifying it using SWV at solid-state electrodes (79). They heat TNT in a confined space and release the gaseous molecules into a modular device where the electrode is housed. Afterwards, the solid-state electrode is exposed to electrochemical measurements and demonstrates a concentration dependent detection of TNT. The attractive feature of this design is that the electrode is housed downstream in the instrumental setup, so that it is not exposed to the extreme heat required for increasing TNT volatility. Since my electrode design contains organic materials, exposing the assembly to temperatures above 100°C will most likely degrade my film. However, it is

essential to store the electrode at temperatures where the integrity of the organic molecules remains stable and the AuNPs do not aggregate.

### **Section Acknowledgements**

I would like to thank the Bill and Melinda Gates Foundation, the Defense Threat Reduction Agency, the North Atlantic Treaty Organization, and Vanderbilt University for funding, resources, and the opportunity to present this work at an international conference (NATO Advanced Research Workshop on Nanotechnology to Aid in Chemical and Biological Defense, September 22-26, 2014, Antalya, Turkey). I would also like to thank Prof. David Wright for giving me the opportunity to present this work, but also to allow me to independently formulate my own ideas and approaches concerning this project. I would also like to thank my fellow collaborators, Prof. David Cliffel along with his student, Evan Gizzie, for mentorship and guidance with regards to experimental design, hypothesis formulation, and data analysis. In addition, I would also like to thank them for providing me with unlimited access to their Chi660A potentiostat. Finally, I would like to thank Alexis Wong for capturing the nanoparticle images for this chapter on the Tecnai Osiris transmission electron microscope (NSF EPS 1004083).

## Chapter IV

### NI(II)NTA GOLD AND SILVER NANOPARTICLES AS LOW-RESOURCE MALARIAL DIAGNOSTIC PLATFORMS FOR THE RAPID COLORIMETRIC DETECTION OF *PLASMODIUM FALCIPARUM* HISTIDINE-RICH PROTEIN-II

#### Abstract

Devoid of antibodies and thermally sensitive materials, this chapter presents a robust, colorimetric diagnostic platform for the detection of a malarial biomarker, *Plasmodium falciparum* Histidine-Rich Protein-II (*Pf*HRP-II) using only pennies worth of material. The assay exploits the optical properties of gold and silver nanoparticles, covalently coupling them to a Ni(II)NTA recognition element specific for *Pf*HRP-II. This chapter builds off of our previously published paper that created colorimetric assays for detection of histidine-rich peptides (80,81). In the presence of the recombinant malarial biomarker (rcHRP-II), the Ni(II)NTA Au and AgNPs begin to crosslink and aggregate in as little as one minute, triggering color changes in solution. For enhanced assay sensitivity and platform stability suitable for low-resource regions, the Ni(II)NTA particles were assembled with varying spacer ligands in a mixed monolayer presentation. When assembled with a negatively charged Peg<sub>4</sub>-thiol ligand, the Ni(II)NTA AuNPs demonstrate low nanomolar limits of rcHRP-II detection in physiological concentrations of human serum albumin and maintain excellent stability at 37°C when stored for four weeks. Although the Ni(II)NTA AgNPs exhibit high picomolar limits of detection, the particles lack stability in high-temperature conditions. To further provide a low-resource

element to the Ni(II)NTA AuNP platform, detection of the malaria biomarker was also measured by capturing and processing images of aggregated gold nanoparticles with a smartphone camera. By utilizing a smartphone camera and image processing application, there is also no significant difference in assay sensitivity and rCHRP-II limit of detection in comparison to a spectrophotometer.

### **Introduction**

In the developing world, early, rapid, and accurate diagnosis is essential to control epidemics and curb resistance for diseases such as tuberculosis, HIV/AIDS, and malaria. Unfortunately, high healthcare costs in these regions compounded with a lack of reliable electricity, a lack of skilled technicians, and a minimal infrastructure burdens disease diagnosis. For malaria, a parasitic disease that threatens most of the developing world and is responsible for approximately one million deaths per year in low-resource regions, rapid point-of-care diagnostic devices are necessitated. In order to combat diagnosis issues presented in the developing world, immunochromatographic rapid diagnostic strip tests (RDTs) have been distributed to detect malarial infection in as little as 15-30 minutes by capturing *Plasmodium falciparum* malarial parasitic antigens in patient blood samples (82). These RDTs take advantage of antibody-antigen interactions to sandwich an antigen in between a paper substrate and AuNPs, providing a chromogenic readout for results indicating infectivity. In 2011, the World Health Organization (WHO) implemented an assessment of these strip tests and determined that only 20% retained the 200-2000 parasites/ $\mu$ L threshold range in patient blood samples recommended by the WHO (83). It was concluded that discrepancies in manufacturing standards, along with

instability from long-term storage in low-resource regions, are possible explanations for test failure. Recent discoveries have also revealed that *P. falciparum* strains in Senegal and India have exhibited genetic diversity, and polymorphisms in the *Pf*HRP-II antigen have been discovered, which further complicates diagnosis via immunoassay platforms (84,85). Based on these recent findings, innovative, sensitive, and robust approaches for antigen recognition are necessitated for sensitive and accurate malaria diagnosis.

Upon infection, the *Plasmodium falciparum* parasite secretes ~97% of a biomarker protein, Histidine-Rich Protein-2 (*Pf*HRP-II), into the host's blood, offering an attractive biomarker for disease diagnosis (86). Approximately ~85% of the primary structure of *Pf*HRP-II is comprised of AHH and AHHAAD repeats, so that targeting these histidine subunit repeats offers an alternative approach for molecular recognition (87). Ni(II)Nitrilotriacetic acid (NTA) chelation is a well established as a strategy to extract and isolate His-tagged proteins, and this octahedral organometallic complex retains micromolar affinity to histidine by coordinating two amino acid subunits per molecule (88-91). Considering *Pf*HRP-II is a naturally occurring His-tagged protein, Ni(II)NTA complexes can coordinate multiple repeats per protein.

The coupling of a Ni(II)NTA recognition component to a robust and sensitive platform would alleviate many of the aforementioned issues with existing RDTs and offer a POC diagnostic platform. Colloidal gold nanoparticles offer a desirable signal transduction approach because of their unique optical properties and biologically inert surface. In the presence of visible light, the electrons at the AuNP particle surface oscillate in-phase with the incident radiation, so that monodisperse colloids exhibit a narrow localized surface plasmon resonance (LSPR) band in the visible spectrum, thus



transmitting bright red colors in solution. The LSPR signal is sensitive to changes in the dielectric environment encompassing the particles, inspiring applications in both sensor and diagnostic development. Shifting the LSPR band can be induced by the physical aggregation of as little as 2-10 particles, which ultimately triggers a color change in solution (13-15). By exploiting these properties, colloidal gold nanoparticles have been well established as aggregation-induced colorimetric sensors for detection of nucleic acids, proteins, small molecules, and metal ions (92-96). The facile ligand coupling via covalent Au-thiol chemistry provides a robust and stable interface capable of enduring the extreme climates typically found in South America, sub-Saharan Africa, and southern Asia where malaria is endemic.

In this chapter, I discuss a robust, low-resource colorimetric platform for malaria diagnosis by selectively and rapidly aggregating Ni(II)NTA Au and AgNPs only in the presence of a recombinant *Pf*HRP-II (rcHRP-II) biomarker, triggering a spectrophotometric redshift and subsequently, a red-to-purple color change (Figure 14). A custom, thiolated Ni(II)NTA recognition ligand has been previously synthesized and validated in our lab as a proof-of-concept design with Ni(II)NTA Au and AgNPs by inducing aggregation in the presence of histidine-rich peptide mimics (80). However, the activity of Ni(II)NTA AuNPs has never been assessed against *Pf*HRP-II and the limits of detection for the peptide mimics are outside of the clinically relevant range (0.2-1 nM *Pf*HRP-II) for malaria diagnosis. I also aspire to optimize the AuNP platform with varying spacer ligands for enhanced signal and stability, along with validating the diagnostic utility of these particles in a complex physiological matrix, mimicking patient samples. Finally, battery-powered smartphones are emerging as rapid detection

technologies in the medical industry, especially through the use of high dynamic range cameras and image processing applications. The rapid colorimetric detection of explosives, pH, and disease biomarkers has been previously detected and analyzed using smartphone technology and processing (97-100). The ability to capture a color image of aggregated nanoparticles with a smartphone and subsequently analyze the respective signal intensity using a downloaded application would reduce user bias and aid in low-resource diagnosis of infectious diseases.

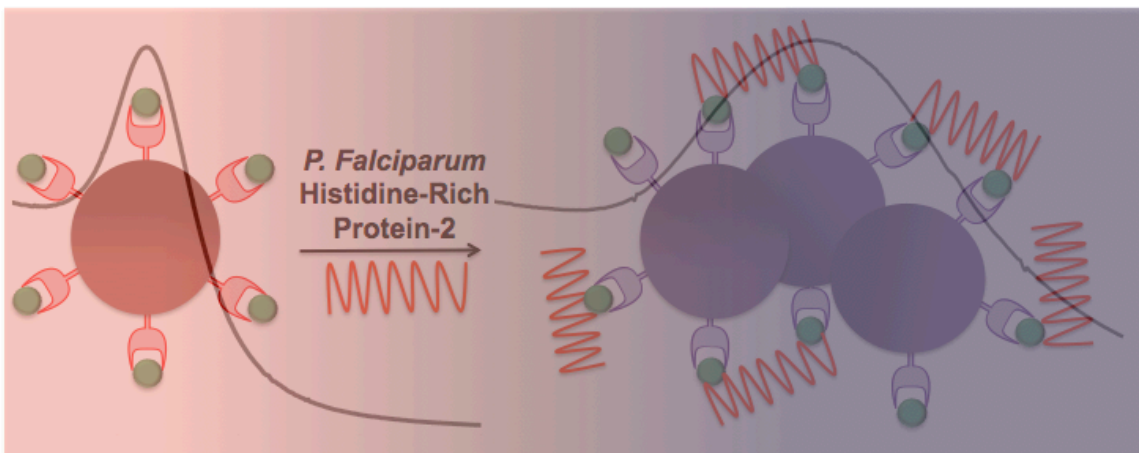


Figure 14. Depiction of Ni(II)NTA AuNP aggregation induced by *Pf*HRP-II, triggering a spectrophotometric redshift and a red-to-purple color change.

## Materials and Methods

### *Materials and reagents*

Citrate-stabilized gold nanoparticles (15 nm) and silver nanoparticles (20 nm) were purchased from Ted Pella, Inc. Recombinant *P. falciparum* Histidine-Rich Protein-II (rcHRP-II) was purchased from CTK Biotech. The thiolated NTA recognition ligand was synthesized previously in our lab along with mercaptoundecanoic-triethylene glycol

(MUA-Peg<sub>3</sub>) (80). Thiol-dPeg<sub>4</sub>-acid (Peg<sub>4</sub>) and m-dPeg<sub>4</sub>-thiol (Peg<sub>4</sub>-methyl) were purchased from Quanta Biodesign, Ltd. 11-Mercaptoundecanoic acid (MUA), 6-mercaptohexanol (MHOL), 11-mercaptoundecanol (MUD), were both purchased from Sigma Aldrich. The confounding proteins, human serum albumin (HSA) and glutathione-S-transferase (GST), were purchased from Sigma Aldrich. All other materials/buffers were purchased from either Sigma Aldrich or Fisher Scientific. All deionized water was used with a resistivity greater than 18 MΩ•cm.

#### *Instrumentation and equipment*

UV-vis spectra were taken with an Agilent 8453 spectrophotometer with a photodiode array detector. Spectrophotometric assays were performed in Corning 384 well plates and measured with a Bio-Tek Synergy H4 plate reader. Electron microscopy images were taken with a CM 20 transmission electron microscope at 200 kV. A Malvern Zetasizer was utilized for in-solution dynamic laser light scattering size distribution measurements. An Eppendorf 5415D microcentrifuge was used to centrifuge AuNPs in 1.5 mL Eppendorf tubes. A Thermo Reciprocal Shaking Bath was utilized to store the particles at 37°C. Photographs of suspended Ni(II)NTA AuNPs were taken with an iPhone 4S smartphone (Apple, CA).

#### *Synthesis of 15 nm Ni(II)NTA AuNPs*

A 2 nM aliquot of 15 nm citrate-stabilized AuNPs was incubated with 5 μM thiolated NTA ligand and 5 μM spacer ligand and allowed to assemble on the particle surface overnight. For synthesis of the 100% Ni(II)NTA AuNPs, 10 μM thiolated NTA

ligand was incubated with the particles and assembled overnight. The next morning 1 mL aliquots of NTA-functionalized AuNPs were washed by centrifugation at 7200 gs for 45 minutes. The supernatant was removed and the particles were resuspended in 0.1 M 4-(2-hydroxyethyl)-1-piperazineethanesulfonic acid (HEPES) buffer containing 0.025% Tween 20 (pH 7.4). This process was repeated three additional times and the particles were finally suspended in 0.1 M HEPES containing 0.025% v/v Tween 20 (pH 7.4). Next, 10  $\mu\text{M}$   $\text{NiCl}_2$  was added to the particles and incubated for 2 hours. After charging with  $\text{Ni}^{2+}$ , the particles were washed three times with 0.1 M HEPES buffer containing 0.025% Tween 20 (pH 7.4). After decanting the final supernatant, the particles were suspended in 0.1 M 2-(N-morpholino) ethanesulfonic acid (MES) buffer containing 0.025% v/v Tween 20 (pH 5.5). The particles were finally filtered through a 0.22  $\mu\text{m}$  syringe filter.

#### *Synthesis of 20 nm Ni(II)NTA AgNPs*

A 120  $\mu\text{M}$  aliquot of 20 nm citrate-stabilized AgNPs was incubated with 5  $\mu\text{M}$  thiolated NTA ligand and 5  $\mu\text{M}$  spacer ligand and allowed to assemble on the particle surface overnight. The next morning 1 mL aliquots of NTA-functionalized AgNPs were washed by centrifugation at 5000 gs for 20 minutes. The supernatant was removed and the particles were resuspended in 0.1 M HEPES buffer containing 0.025% Tween 20 (pH 7.4). This process was repeated three additional times and the particles were finally suspended in 0.1 M HEPES containing 0.025% v/v Tween 20 (pH 7.4). Next, 10  $\mu\text{M}$   $\text{NiCl}_2$  was added to the particles and incubated for 2 hours. After charging with  $\text{Ni}^{2+}$ , the particles were washed three times with 0.1 M HEPES buffer containing 0.025% Tween

20 (pH 7.4). After decanting the final supernatant, the particles were suspended in 0.1 M 2-(N-morpholino) ethanesulfonic acid (MES) buffer containing 0.025% v/v Tween 20 (pH 5.5). The particles were finally filtered through a 0.22  $\mu\text{m}$  syringe filter.

#### *rcHRP-II-induced aggregation assays with Ni(II)NTA Au and AgNPs*

A 5  $\mu\text{L}$  volume of rcHRP-II dissolved in deionized water was mixed with a 45  $\mu\text{L}$  volume of 1.15 nM AuNPs or 80 pM AgNPs in a Corning 384 well plate. The plate was shaken for 15 minutes before taking absorbance measurements 600 nm and 525 nm for Ni(II)NTA AuNPs and 407 nm and 520 nm for Ni(II)NTA AgNPs. A background measurement consisted of 45  $\mu\text{L}$ s of 0.1 M MES with 0.025% Tween 20 (pH 5.5) plus 5  $\mu\text{L}$  deionized water. After the background was subtracted, the aggregation signal was assessed by taking the ratio of the two selected wavelengths ( $A_{600\text{nm}}/A_{525\text{nm}}$  for AuNPs and  $A_{520\text{nm}}/A_{407\text{nm}}$  for AgNPs) and normalizing the samples containing no protein to 1. All measurements were performed in triplicate, while 6 replicates of blank measurements were recorded.

#### *rcHRP-II-induced aggregation assays with Ni(II)NTA AuNPs in complex matrices*

A 5  $\mu\text{L}$  volume of rcHRP-II dissolved in 37 mg/mL HSA was mixed with a 45  $\mu\text{L}$  volume of 1.15 nM Peg<sub>4</sub>:Ni(II)NTA AuNPs in a Corning 384 well plate. Particles were suspended in 0.1 M MES buffer containing 125 mM imidazole and 150 mM NaCl with 0.025% Tween 20 (pH 5.5). The plate was shaken for 15 minutes before taking absorbance measurements 600 nm and 525 nm for Ni(II)NTA AuNPs. A blank measurement consisted of 45  $\mu\text{L}$ s of 0.1 M MES in 125 mM imidazole and 150 mM

NaCl with 0.025% Tween 20 (pH 5.5) plus 5  $\mu$ L 37 mg/mL human serum albumin. After the blank was subtracted, the aggregation signal was assessed by taking the ratio of the two selected wavelengths ( $A_{600}/A_{525}$ ) and normalizing the samples containing no rcHRP-II to 1. All measurements were performed in triplicate, while 6 replicates of blank measurements were recorded.

#### *Low-resource Ni(II)NTA AuNP aggregation analysis with iOS application*

The Peg<sub>4</sub>:Ni(II)NTA AuNPs were titrated against rcHRP-II in a white Costar 96 well plates. A 180  $\mu$ L Peg<sub>4</sub>:Ni(II)NTA AuNP suspension (1.15 nM) in 0.1 M MES containing 125 mM imidazole and 150 mM NaCl with 0.025% Tween 20 (pH 5.5) was added to a white Costar 96 well plate. Next, 20  $\mu$ Ls of a rcHRP-II protein solution was added to the wells before incubating for 15 minutes. High dynamic range images of the AuNPs were captured with an iPhone 4S camera with the iOS 7.0.6 platform. For color analysis, the commercially available iPhone application, Color Companion (Digital Media Interactive, LLC), was downloaded onto the iOS 7.0.6 platform for analysis of the red, blue and green signal intensities of gold nanoparticle suspensions in each well. Analysis was calculated by averaging the green and blue signal intensities and dividing it by the red signal intensity. Blank measurements (no protein added to wells) were normalized to values of one.

## Results and Discussion

### *Ni(II)NTA AuNP characterization*

The functionalization of gold nanoparticles with a thiolated Ni(II)NTA recognition ligand specific for the *Pf*HRP-II malarial biomarker has the potential to create a rapid, robust diagnostic, capable of withstanding the extreme climates encountered in low-resource regions of the world. Moreover, manipulation of the gold particle surface with varying spacer ligands has the ability to improve both assay sensitivity and long-term stability in the developing world. All of the ligands used in this chapter are shown below (Figure 15). The hydrophobic alkanethiols, mercaptoundecanoic acid (MUA), mercaptohexanol (MHOL), and mercaptoundecanol (MUD) possess strong self-assembly characteristics because the van der Waals interactions between methylene units on neighboring ligands promote a strong and stable monolayer adsorbed to the gold surface (19). MUA contains a terminal negative charge, enhancing stability of colloidal particles, while MHOL and MUD both possess a terminal alcohol, facilitating crosslinking interactions and hydrogen bonding between the protein-particle interfaces. Thiol-dPeg<sub>4</sub>-Acid (Peg<sub>4</sub>) and dPeg<sub>4</sub>-thiol (Peg<sub>4</sub>-methyl) possess hydrophilic character and are readily water-soluble, promoting favorable interactions among aqueous colloidal nanomaterials. In addition, polyethylene glycol molecules are well-known for their anti-fouling and repellent properties versus protein and cell adsorption, further enhancing stability and reducing the risk of non-specific binding in this assay (101-104). Finally, the mercaptoundecanoic acid-triethylene glycol (MUA-Peg<sub>3</sub>) amphiphilic ligand provides strong self-assembly characteristics in addition to anti-fouling properties. Many of the spacer ligands display similar performances when assembled onto AuNPs, so for the

purposes of brevity, the activities of MUA, MHOL, and Peg<sub>4</sub> are discussed in this chapter, while the data for MUA-Peg<sub>3</sub>, MUD, and Peg<sub>4</sub>-methyl is presented in the supplemental data in appendix C.

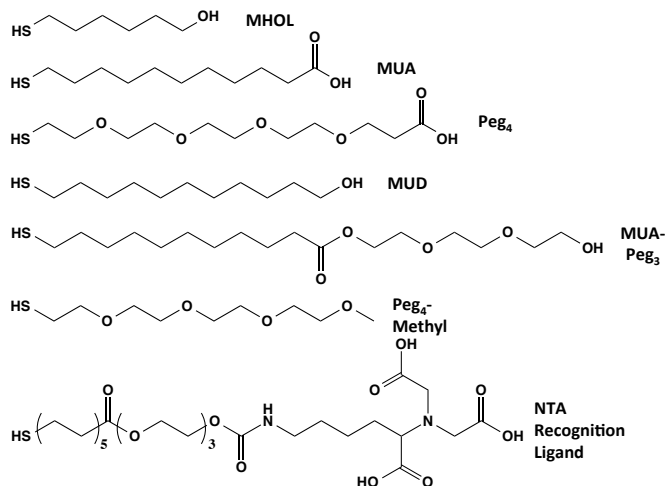


Figure 15. Structures and abbreviations of spacer ligands and the NTA recognition ligand in this chapter.

Upon functionalization with 50:50 ratios of Ni(II)NTA recognition ligand relative to varying spacer ligands, the particles are stable, as indicated by the bright red colors in solution, the narrow surface plasmon resonance band in the UV-vis spectra, and the monodisperse particle size distribution in the electron microscopy images (Figure 16). Relative to citrate-stabilized gold nanoparticles, the Ni(II)NTA-functionalized particles undergo a 3-5 nm red shift in the UV-vis spectrum, which correlates to the coordination of a dielectric monolayer to the particle surface, as indicated by the 3-5 nm hydrodynamic diameter increase in laser light scattering experiments (Figure 17).



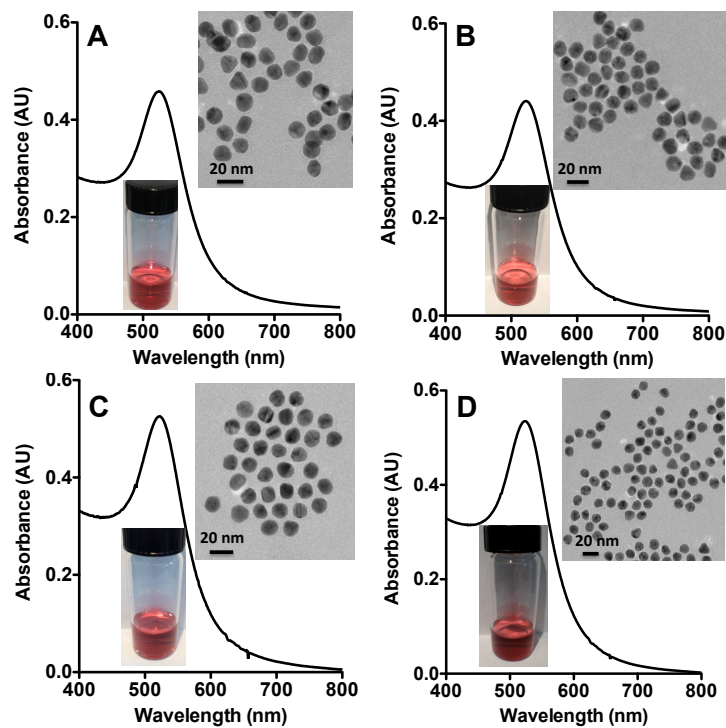


Figure 16. Ni(II)NTA AuNP characterization in 0.1 M MES with 0.025% Tween 20 (pH 5.5). UV-vis spectra, TEM images and suspended AuNP images of monodisperse (A) 100% Ni(II)NTA AuNPs, (B) 50:50 MHOL:Ni(II)NTA AuNPs, (C) 50:50 Peg<sub>4</sub>:Ni(II)NTA AuNPs, and (D) 50:50 MUA:Ni(II)NTA AuNPs.

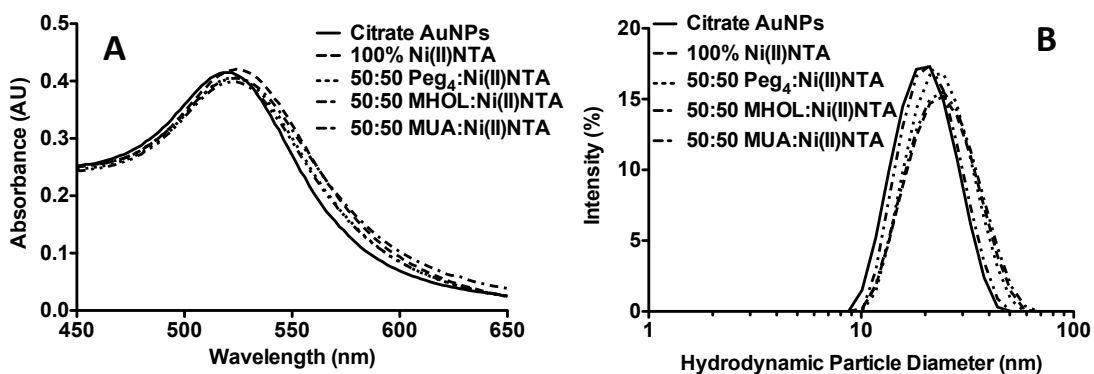


Figure 17. (A) Spectrophotometric and (B) dynamic laser light scattering spectral shifts of Ni(II)NTA AuNPs upon coordination of ligands to metal surface. 1 nM concentrations of AuNPs were suspended in 0.1 M MES buffer with 0.025% Tween 20 (pH 5.5).

### *Ni(II)NTA AuNP aggregation induced by rcHRP-II*

The previous Ni(II)NTA Au and AgNP platform demonstrating the aggregation activity of *Pf*HRP-II peptide mimics highlights the importance of pH in the assay (80). Below the isoelectric point of histidine (~6), the positively charged free imidazole side chains create a hydrogen bond network among neighboring proteins, thus facilitating crosslinking interactions between the Ni(II)NTA moieties on neighboring particles and the protein. In addition, below pH 7, *Pf*HRP-II primarily adopts a  $\alpha$ -helical structure *in vitro*, orienting histidine units on the surface of the protein (105). *Pf*HRP-II also coordinates as many as 15-17 Fe(II) heme molecules *in vitro* via bishistidyl axial ligation, ultimately adopting a  $3_{10}$ -helical secondary structure in the process (104). The slightly acidic pH nature of the assay gives rise to protein orientations for favorable Ni(II)-histidine coordination and reduced steric effects, while the heme binding studies validate M(II) affinity as a recognition component.

Upon reacting the Ni(II)NTA AuNPs with 100 nM rcHRP-II at pH 5.5, all particles exhibit aggregation. Indicated by the spectrophotometric red shift, the particles physically change color from red to purple, due to plasmon band coupling from rcHRP-II-induced aggregation (Figure 18). Protein-induced aggregation is further confirmed by TEM images and the substantial shift in size distribution of particles in dynamic laser light scattering experiments. Nearly 50% of the spectrophotometric signal given off by particle aggregation occurs after one minute, as indicated by a substantial red shift in the UV-vis spectra (Appendix C). Final absorbance measurements are taken after 15 minutes, as the spectrophotometric signal begins to level off. The rapid timeframe required to

generate a signal induced by particle aggregation compares very well with the 15-30 minute timeframe for current RDT's.

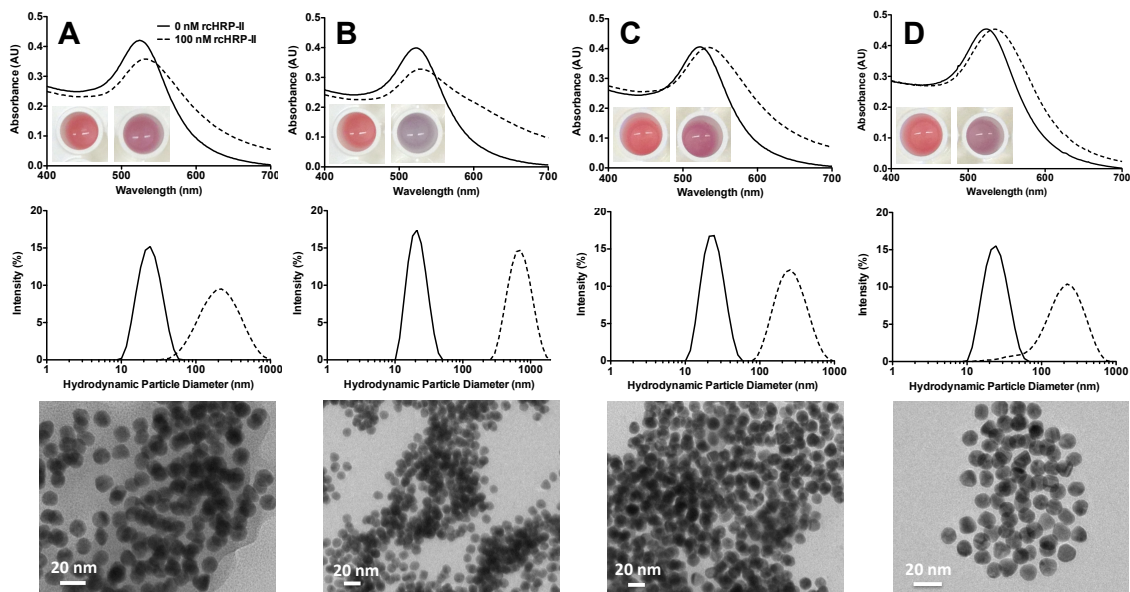


Figure 18. Aggregation of Ni(II)NTA AuNPs in the presence of 100 nM rcHRP-II at pH 5.5 for (A) 100% Ni(II)NTA AuNPs, (B) 50:50 MHOL:Ni(II)NTA AuNPs, (C) 50:50 Peg<sub>4</sub>:Ni(II)NTA AuNPs, and (D) 50:50 MUA:Ni(II)NTA AuNPs. The top graphs represent UV-vis spectra before (solid line) and after (dashed line) adding rcHRP-II. The images on the left are the color changes the particles undergo before (left) and after (right) aggregation. The middle graphs represent dynamic laser light scattering particle size distributions before (solid line) and after (dashed line) rcHRP-II-induced aggregation. The bottom row shows TEM images of rcHRP-II-induced aggregated Ni(II)NTA AuNPs.

In order to determine the activity of the Ni(II)NTA AuNPs with varying spacer ligands, rcHRP-II is titrated against each Ni(II)NTA AuNP platform (Figure 19). After 15 minutes incubation with rcHRP-II, the spectrophotometric signal is measured by taking a ratio of two selected absorbance wavelengths ( $A_{600\text{nm}}/A_{525\text{nm}}$ ) and normalizing the blank values to 1. With the assembly of all spacer ligands, the assay limit of detection increases by an order of magnitude relative to the 100% Ni(II)NTA AuNPs (Appendix C). The

MHOL:Ni(II)NTA AuNPs exhibit the highest sensitivity along with the largest signal-to-noise at the saturated rcHRP-II concentrations. In contrast, the 100% Ni(II)NTA AuNPs display the lowest sensitivity, signal-to-noise, and the highest limit of rcHRP-II detection. The Peg<sub>4</sub>:Ni(II)NTA AuNPs and MUA:Ni(II)NTA AuNPs exhibit excellent limits of detection, but decreased signal and sensitivity in comparison to MHOL:Ni(II)NTA AuNPs. It is hypothesized that steric crowding of the 100% Ni(II)NTA ligand monolayer is responsible for the reduced sensitivity and detection limits. When Ni(II)NTA AuNPs are assembled with MUA and Peg<sub>4</sub> spacer ligands, the terminal negative charge on the spacer ligand most likely repels the particles, decreasing their overall signal and sensitivity relative to the MHOL:Ni(II)NTA AuNPs. The assembly of Ni(II)NTA AuNPs with the small MHOL reduces steric crowding and its terminal alcohol facilitates hydrogen-bonding interactions among the protein-particle interface, ultimately favoring aggregation in the presence of rcHRP-II. Compared to the high nanomolar limits of detection against histidine-rich peptide mimics, the Ni(II)NTA AuNP platform assembled with spacer ligands increases the rcHRP-II limits of detection by two orders of magnitude into clinically relevant ranges.

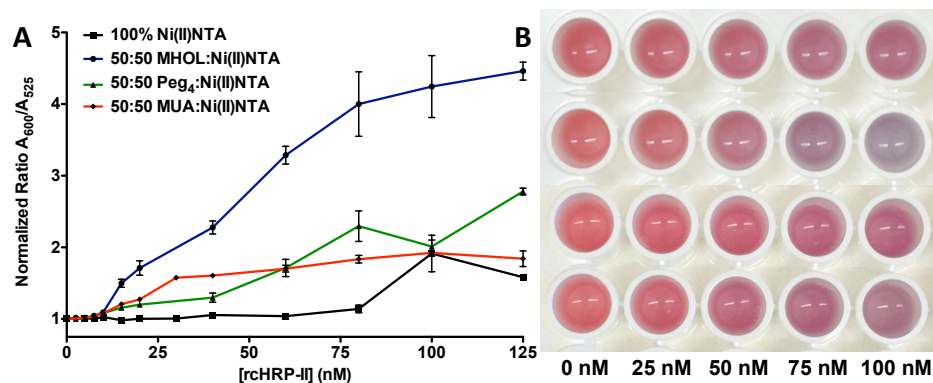


Figure 19. Titration of rcHRP-II with Ni(II)NTA AuNPs assembled with varying spacer ligands in 0.1 M MES with 0.025% Tween 20 (pH 5.5). (A) Spectrophotometric titrations and (B) Colorimetric titrations ranging from 0-100 nM rcHRP-II concentrations. From top, 100% Ni(II)NTA AuNPs, 50:50 MHOL:Ni(II)NTA AuNPs, 50:50 Peg<sub>4</sub>:Ni(II)NTA AuNPs, and 50:50 MUA:Ni(II)NTA AuNPs.

#### *Ni(II)NTA AuNP stability*

In order to determine the viability of the Ni(II)NTA AuNPs as a malarial diagnostic, the particles with varying spacer ligands are evaluated in conditions mimicking the environments encountered in low-resource settings. All of the particles are stored in a water bath (37°C) for a four-week time period, mimicking low-resource regions with the most extreme temperatures and humidity. At two-week and four-week intervals, the aggregation activity of the particles is assessed upon exposure to 100 nM rcHRP-II (Figure 20). Ni(II)NTA AuNPs assembled with the negatively charged MUA and Peg<sub>4</sub> spacer ligands maintain consistent aggregation activity over the four-week time period. It is hypothesized that the stable self-assembled monolayer along with the negative terminal charge prevents particle aggregation in solution in order to maintain stability. In addition, the 100% Ni(II)NTA AuNPs also preserve stability at the elevated temperature because the Ni(II)NTA complex is partially negatively charged. In contrast, the MHOL:Ni(II)NTA AuNPs lose approximately two-thirds of their aggregation activity

after two weeks and nearly 100% activity after four weeks. It has been recently understood that colloidal AuNPs assembled with short-chained alkanethiols lose stability due to their overwhelming van der Waal interactions between neighboring ligands, and aggregation ultimately occurs (107). This study also affirms that colloidal AuNPs assembled with longer MUA and Peg<sub>4</sub> ligands retain stability. The AuNP stability is further tracked by measuring variances in the UV-vis spectra at the aforementioned time intervals. The LSPR peak associated with the MHOL:Ni(II)NTA AuNPs begins to redshift after one week at 37°C. After four weeks elapsed time, these particles lose significant absorbance in the UV-vis spectrum, and the LSPR redshifts approximately 65 nm, indicating complete aggregation and a lack of stability in these conditions (Appendix C). In contrast, the 100% Ni(II)NTA AuNPs and MUA:Ni(II)NTA AuNPs maintain >80% of their LSPR absorbance after four weeks, while the Peg<sub>4</sub>:Ni(II)NTA AuNPs possess >90% of their LSPR absorbance after four weeks.

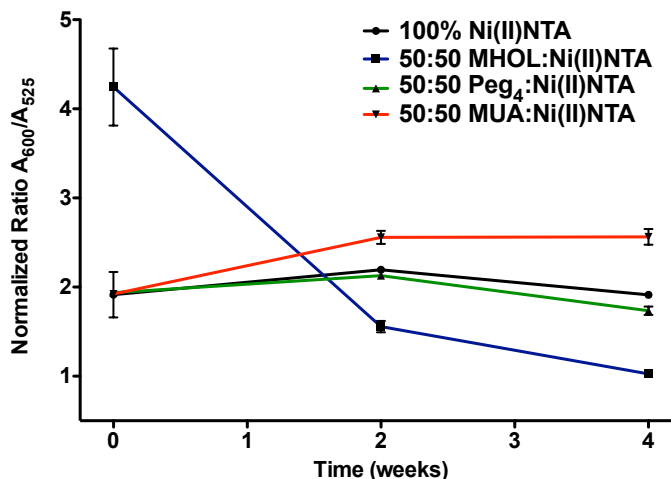


Figure 20. Stability of Ni(II)NTA AuNPs at 37°C. 1 nM Ni(II)NTA AuNP suspensions at pH 5.5 are stored in sealed 1.5 mL Eppendorf tubes in a water bath at 37°C for four weeks. At two-week intervals, the particles are reacted with 100 nM rcHRP-II for 15 minutes before taking absorbance measurements at 525 nm and 600 nm.

#### *Peg<sub>4</sub>:Ni(II)NTA AuNP assay performance in imidazole*

Peg<sub>4</sub>:Ni(II)NTA AuNPs are chosen for further assays in human serum albumin (HSA) and plasma complex matrices because of their consistent stability and activity when stored at elevated temperatures. The Peg<sub>4</sub>:Ni(II)NTA AuNPs retain the highest relative LSPR peak absorbance after four weeks incubation in addition to their consistent aggregation activity at 37°C. Moreover, Peg molecules are well established as anti-fouling agents, further reducing non-specific binding in our assay. A series of blocking conditions is first established for the Peg<sub>4</sub>:Ni(II)NTA AuNPs. Imidazole is known to have millimolar affinity for Ni(II)NTA and serves as a blocking agent to physiological confounding proteins such as HSA (108). When incubated in 0.1 M MES buffer containing imidazole and NaCl, the Peg<sub>4</sub>:Ni(II)NTA AuNPs are stable up to 250 mM concentrations, whereas above 250 mM imidazole, the Ni(II)NTA sites become

overwhelmed by imidazole, and aggregation ultimately occurs (Appendix C). In the presence of 100 nM rcHRP-II, imidazole enhances assay performance linearly from 0 mM to 50 mM imidazole. Between 50 mM and 250 mM imidazole, the maximum assay signal plateaus, whereas above 250 mM, assay signal decreases due to imidazole-induced aggregation (Appendix C). A blocking condition of 125 mM imidazole is chosen because at this concentration, the signal-to-noise ratio is optimized and the particles are monodisperse (Figure 21).

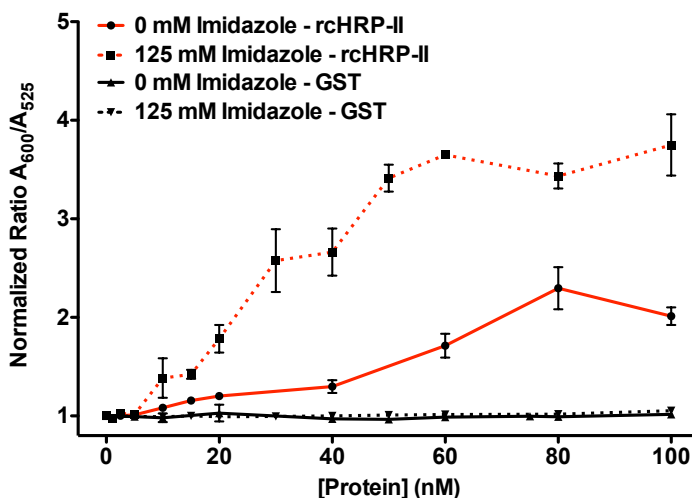


Figure 21. Effect of 125 mM imidazole on Peg<sub>4</sub>:Ni(II)NTA AuNP aggregation when induced by rcHRP-II. The particles are suspended in 125 mM imidazole and 150 mM NaCl in 0.1 M MES buffer with 0.025% Tween 20 (pH 5.5) upon being incubated with varying concentrations of rcHRP-II. After 15 minutes, absorbance measurements are taken at 525 nm and 600 nm.

The particles are first titrated against rcHRP-II and demonstrate a three-fold increase in sensitivity and a two-fold saturated signal-to-noise enhancement (Appendix C). The protonated imidazole cations at high concentrations aid in rcHRP-II-induced Ni(II)NTA AuNP aggregation by facilitating the cation-hydrogen bond network among



neighboring proteins, thus increasing assay sensitivity. To control for non-specific interactions, the Ni(II)NTA AuNPs are titrated against the fusion protein tagged onto recombinant rcHRP-II, glutathione-S-transferase (GST), and no significant aggregation is evident.

#### *Peg<sub>4</sub>:Ni(II)NTA AuNP colorimetric analysis with smartphone application*

Although Peg<sub>4</sub>:Ni(II)NTA AuNP activity can be easily measured with a spectrophotometer in a laboratory setting, inconsistent electricity burdens this analytical technique in low-resource regions. However, the physical color transitions of Peg<sub>4</sub>:Ni(II)NTA AuNP aggregates upon rcHRP-II incubation can be captured with a battery-powered iPhone and subsequently quantified with image processing applications, further making this diagnostic platform applicable to low-resource areas. Taking advantage of a commercially available iPhone application, Color Companion, photographs of suspended nanoparticles are uploaded and processed for analysis of the RGB color intensities. To achieve a raw signal intensity value, the blue and green intensities are averaged and divided by the red intensity. The rcHRP-II biomarker is titrated with the Peg<sub>4</sub>:Ni(II)NTA AuNPs in a white, opaque 96-well plate for enhanced contrast (Appendix C). The wells containing AuNPs with no protein added are normalized to values of one. The signal generated by the Color Companion application yields a linear response between 0-40 nM rcHRP-II concentrations before saturation, similar to the signal generated by a spectrophotometer (Figure 22). There is also no significant difference between the sensitivity (0.038 Signal/nM) and limit of detection (5.2 nM) in comparison to spectrophotometric detection. The image capturing and

processing using this smartphone platform are capable of processing and quantifying molecular recognition events in future colorimetric assays.

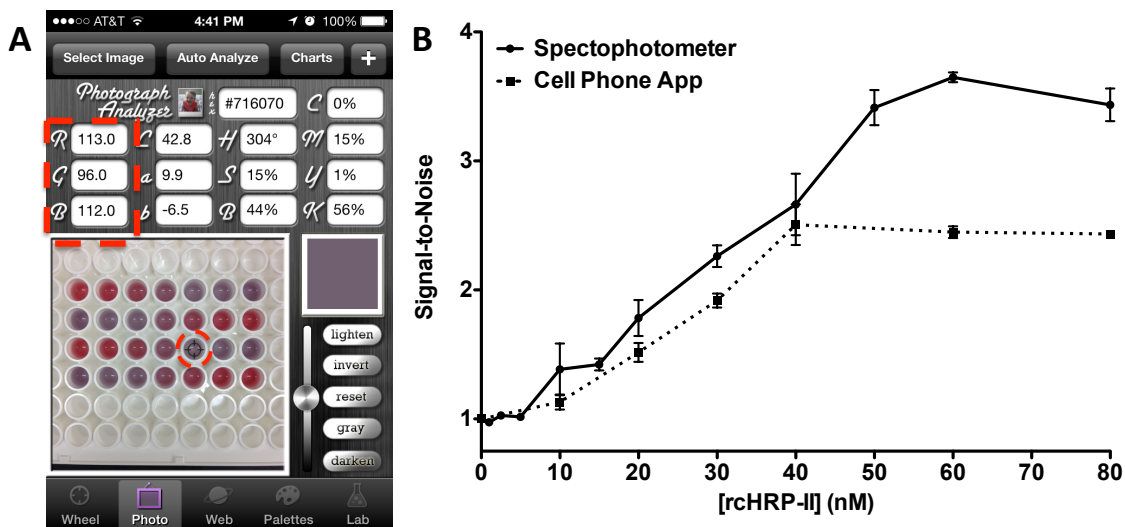


Figure 22. Workflow of low-resource detection of rcHRP-II using the Peg<sub>4</sub>:Ni(II)NTA AuNP platform. (A) The Peg<sub>4</sub>:Ni(II)NTA AuNPs (1 nM, 0.1 M MES containing 125 mM imidazole, 150 mM NaCl, and 0.025% Tween 20) were titrated with rcHRP-II and after 15 minutes, images of the suspended particles were captured with an iPhone 4S camera and uploaded into the Color Companion commercial application. In order to process the color change induced by rcHRP-II, the bulls-eye cursor (highlighted with the dashed red circle) was moved over a well in a white 96 well-plate and RGB signal intensities were conferred (highlighted with the dashed red box). To calculate raw signal, the green and blue signal intensities were averaged and divided by the red signal intensity values. (B) Plot of signal intensity measured with a spectrophotometer and the Color Companion commercial application. There is no significant difference in sensitivity and rcHRP-II limit of detection between the spectrophotometer and the commercial application.

#### *Peg<sub>4</sub>:Ni(II)NTA AuNP assay performance in complex matrices*

In order to mimic a potential patient sample, rcHRP-II is dissolved in the physiological concentrations of HSA (37 mg/mL) and human plasma, respectively. When dissolved in physiological concentrations of HSA, the Peg<sub>4</sub>:Ni(II)NTA AuNP colorimetric assay has the same rcHRP-II sensitivity versus 0 mg/mL HSA, as

demonstrated by the spectrophotometric linear dynamic range and the similar color change upon reactions with rcHRP-II (Figure 23). There is also no significant difference in limits of detection when rcHRP-II is dissolved in 37 mg/mL versus 0 mg/mL HSA, demonstrating the robust, selective nature of the Peg<sub>4</sub>:Ni(II)NTA AuNP platform (Appendix C). The 125 mM imidazole concentration provides adequate blocking in the HSA biological matrix, but does not interfere with rcHRP-II-induced aggregation when dissolved in 37 mg/mL HSA. However, the particles show little activity when rcHRP-II is dissolved in plasma. The high viscosity of plasma makes particle aggregation difficult because Ni(II)NTA only has micromolar affinity to histidine subunits. However, the low nanomolar limits of rcHRP-II detection in HSA are competitive with the WHO's upper threshold limit of detection of 2000 parasites/ $\mu$ L, which corresponds to approximately 1 nM *Pf*HRP-II. In order to make an impact in the developing world, the *Pf*HRP-II biomarker limit of detection must be 200 pM and below in order to identify asymptomatic carriers of the disease, as per recommendation by the WHO.

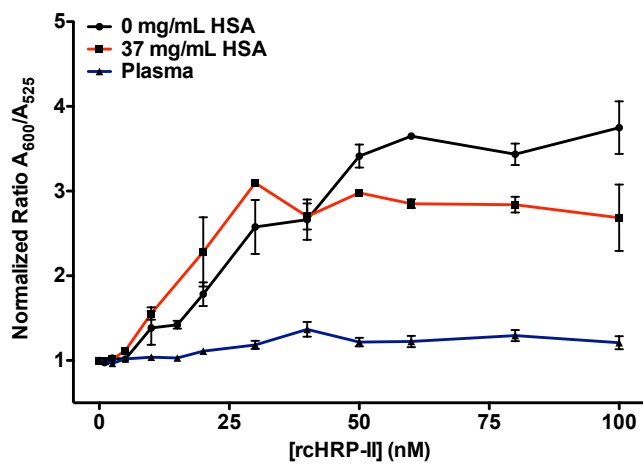


Figure 23. Titrations of rcHRP-II with Peg<sub>4</sub>:Ni(II)NTA AuNPs when the biomarker is dissolved in a physiological concentration of human serum albumin and plasma.

### *20 nm Peg<sub>4</sub>:Ni(II)NTA AgNP rationale for enhanced assay signal*

The WHO recommends a lower operational threshold detection of 200-2000 parasites/ $\mu$ L for RDT use in the developing world, which correlates to 0.2-1 nM *Pf*HRP-II in a patient blood sample. In order to be provide utility in low-resource regions, the limit of rcHRP-II detection must be enhanced by at least an order of magnitude. Silver nanoparticles (AgNPs) offer an attractive solution because not only do they exhibit the surface plasmon resonance phenomenon, but also their molar extinction coefficient is approximately an order of magnitude greater than AuNPs of the same size, which could potentially increase the sensitivity of rcHRP-II detection. AgNPs have demonstrated excellent scattering properties and as a result, possess a very strong electromagnetic field at the particle surface, which has provided applications in surface-enhanced Raman spectroscopy, colorimetric sensing, and near-field fluorescence enhancement (11,80). In addition, the noble metal silver also has a strong proclivity for thiols, promoting facile ligand coupling onto the particle surface with the well-characterized Ni(II)NTA recognition ligand. Since Peg<sub>4</sub> demonstrates optimum stability when adsorbed onto AuNP surfaces, it is mixed in a 1:1 ratio of Ni(II)NTA recognition ligand and assembled onto AgNP surfaces (Figure 24).

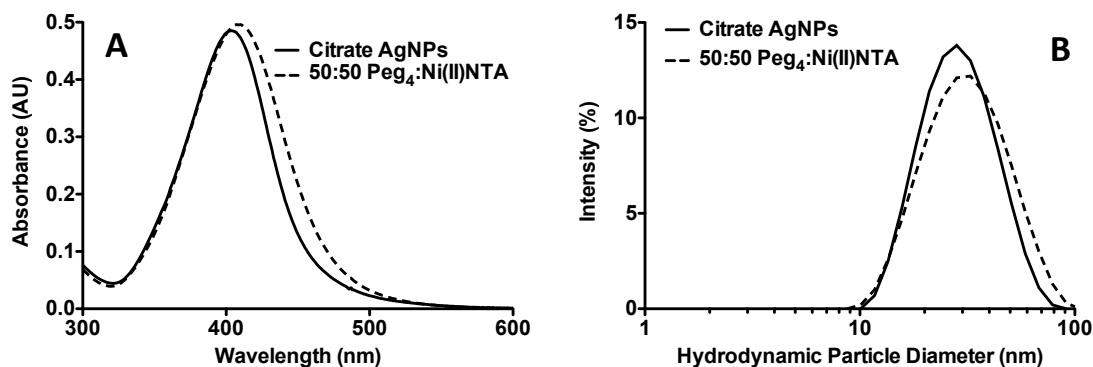


Figure 24. (A) Spectrophotometric and (B) dynamic laser light scattering spectral shifts of 20 nm Ni(II)NTA AgNPs upon coordination of ligands to metal surface. 100 pM concentrations of AgNPs were suspended in 0.1 M MES buffer with 0.025% Tween 20 (pH 5.5).

#### *Peg<sub>4</sub>:Ni(II)NTA AgNPs assays with rcHRP-II*

The Peg<sub>4</sub>:Ni(II)NTA AgNPs ligand is easily assembled onto the Ag surface, as shown by the spectrophotometric redshift and the hydrodynamic particle increase in DLS experiments. The Peg<sub>4</sub>:Ni(II)NTA AgNPs rapidly aggregate upon rcHRP-II incubation, inducing a spectral redshift, and a yellow-to-red color change in solution (Figure 25). Characterized similarly to the Ni(II)NTA AuNPs upon reacting with rcHRP-II, the aggregated AgNPs demonstrate a large UV-vis spectral shift and a substantial increase in hydrodynamic particle diameter. Additionally, a second peak begins to arise in the UV-vis spectral profile at 500 nm, generating the potential for an enhanced sensitivity.

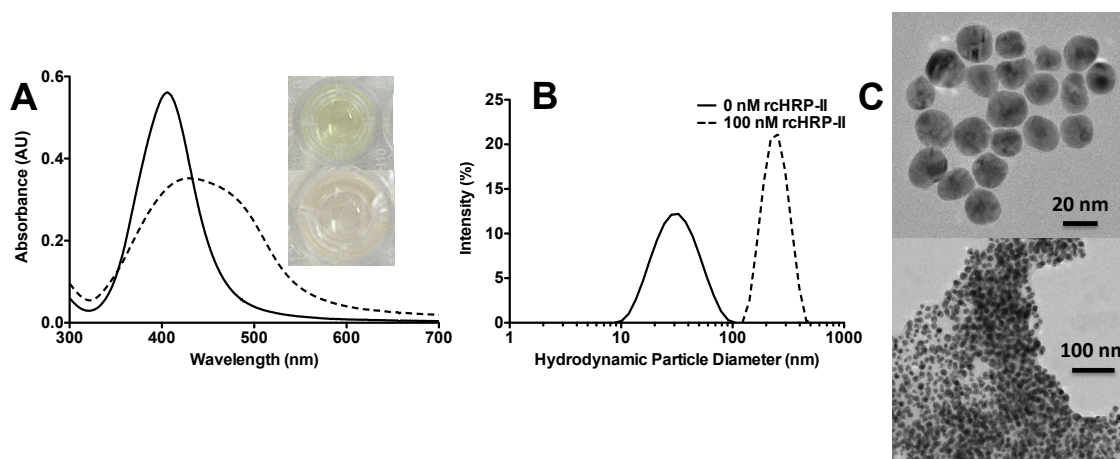


Figure 25. Aggregation of Ni(II)NTA AgNPs upon reactions with 100 nM rcHRP-II. Particles (80 pM) are suspended in 0.1 M MES with 0.025% Tween 20 (pH 5.5). (A) Spectrophotometric shift before (solid line) and after (dashed line) adding rcHRP-II. The picture on the top depicts AgNPs before aggregation while the picture on the bottom is indicative of aggregated AgNPs. (B) Dynamic laser light scattering before (solid line) and after (dashed line) adding rcHRP-II. (C) TEM images before (top) and after (bottom) adding rcHRP-II.

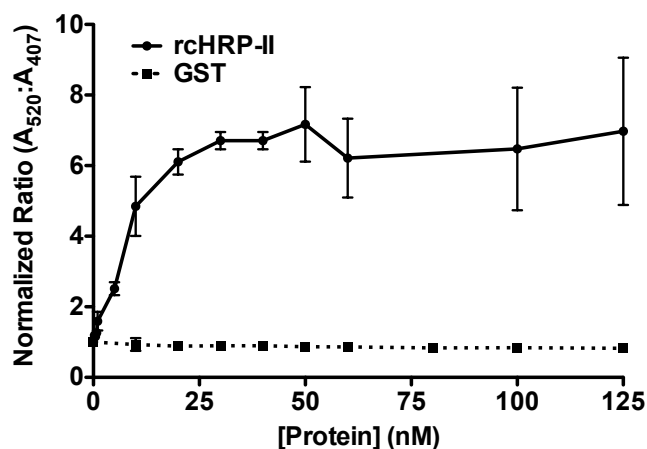


Figure 26. Titration of rcHRP-II and GST with 80 pM Peg<sub>4</sub>:Ni(II)NTA AgNPs.

After reacting with particles with high concentrations of biomarker, they are titrated with rcHRP-II and the negative control protein, GST (Figure 26). The saturated signal-to-noise nearly triples relative to the AuNPs, while GST exhibits zero aggregation

activity. The 0.79 nM limit of detection and the 0.36 AU/nM sensitivity, respectively, are approximately an order of magnitude greater than the Peg<sub>4</sub>:Ni(II)NTA AuNPs under identical reaction conditions, falling within the 0.2-1 nM range recommended by the WHO. In addition, they display similar levels of specificity relative to the AuNPs, showing zero activity when reacted with GST and validating the specificity of the Ni(II)NTA platform. In order to probe for stability, the particles are stored in conditions mimicking intense climates in the developing world (Figure 27). After four weeks at room temperature, the particles lose approximately one-third of their initial absorbance value, while at 37°C, the absorbance diminishes by a factor of two-thirds. Although silver exhibits an order of magnitude signal enhancement, the particles are not stable. The volatility associated with Peg<sub>4</sub>:Ni(II)NTA AgNPs reveal higher error bars at saturated rCHRP-II conditions. These results suggest two possible explanations for the high levels of variability. First, silver does not possess the completely inert characteristics like gold and is more prone to oxidation (109). Second, ligands are adsorbed in unfavorable assemblies (110). While alkanethiols assemble at a 60° angle relative to the gold surface, the efficient ligand packing creates optimized van der Waal interactions, and as a result, a stable monolayer. Silver, on the contrary, packs ligands at 75-85° angles relative to the surface, reducing the van der Waal interactions and diminishing the overall monolayer strength (110). The subsequent S-C bond on AgNPs is also more strained because the ligands assemble in a more perpendicular fashion, further reducing monolayer stability. These problems demonstrate that only the AuNP platform demonstrates utility in the developing world. These results also indicate that the failure of

RDTs is most likely due to antibody degradation, and not particle degradation or aggregation.

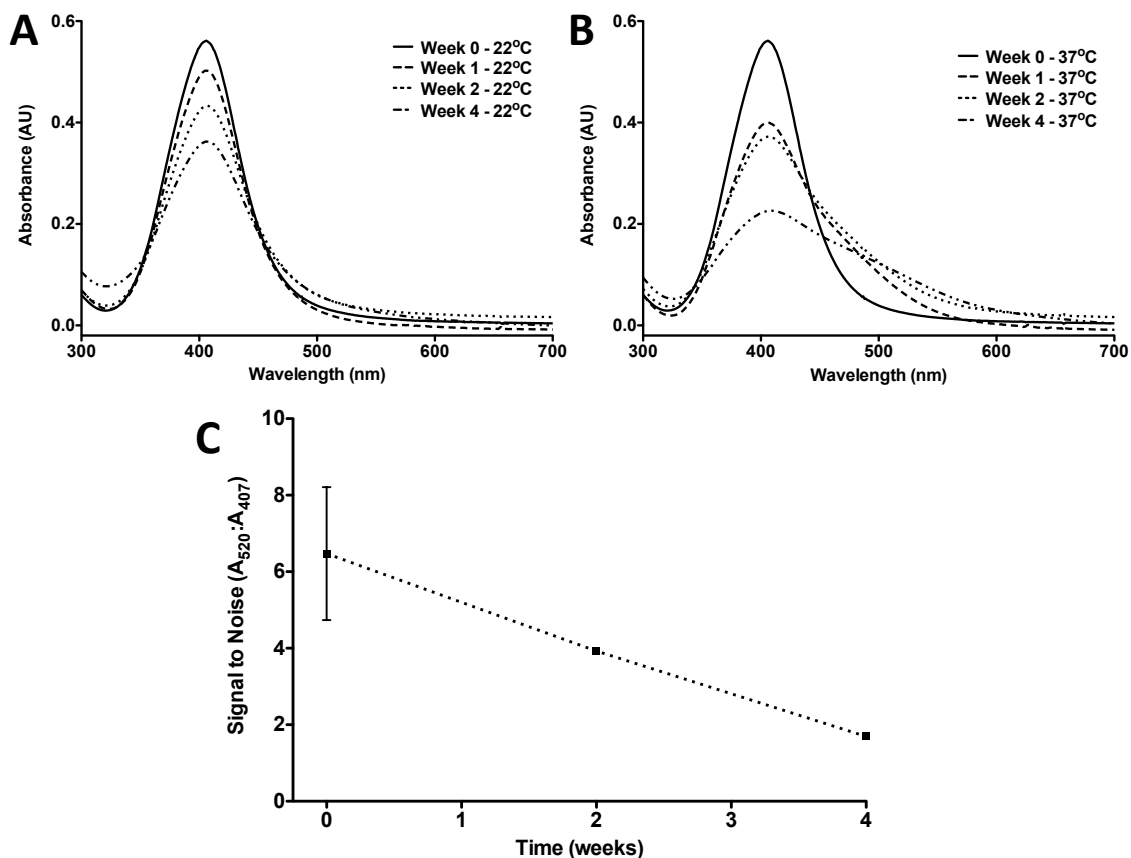


Figure 27. Stability studies of 80 pM Peg<sub>4</sub>:Ni(II)NTA AgNPs suspended in 0.1 M MES with 0.025% Tween 20 (pH 5.5). (A) UV-vis spectra when AgNPs are stored at 22°C and (B) 37°C. (C) Aggregation activity when reacted with 100 nM rCHRP-II after two week intervals. These particles were stored at 37°C.

## Conclusion

In this chapter, I optimized the Ni(II)NTA AuNP platform for detection of a malarial biomarker, recombinant *Pf*HRP-II, by incorporating various spacer ligands onto the surface of AuNPs for optimum stability and sensitivity. With the negatively charged, water-soluble Peg<sub>4</sub> spacer ligand assembled onto the particle surface, the Ni(II)NTA



AuNPs retain excellent stability when stored at 37°C for four weeks, suggesting that this diagnostic platform can endure the harsh climates encountered in low-resource regions. In the presence of rcHRP-II, the Ni(II)NTA AuNPs aggregate in as little as one minute, while the 15-minute timeframe required to level the spectrophotometric signal is very competitive with existing malaria RDTs. The Peg<sub>4</sub>:Ni(II)NTA AuNPs also exhibit low nanomolar limits of rcHRP-II detection when dissolved in the physiological concentration of the most abundant interfering protein, human serum albumin, overlapping the WHO's upper threshold detection limit of 2000 parasites/μL or 1 nM *Pf*HRP-II. Finally, the signal generated by aggregated AuNPs can be digitized with an iPhone camera and processed with a commercially available application, demonstrating similar sensitivity and limits of detection in comparison to a spectrophotometer. With the stable Peg<sub>4</sub> platform, signal enhancement is achieved with AgNPs, but the lack of stability complicates this platform as a low-resource diagnostic platform. Nonetheless, the simple user interface of this diagnostic platform coupled with the rapid response times of rcHRP-II-induced NP aggregation may be amenable to low-resource regions if sensitivity can be achieved without compromising stability.

### **Section Acknowledgements**

I would like to thank the Bill & Melinda Gates Foundation and Vanderbilt University for providing funding and resources to this project. I would also like to thank Prof. David Wright for his guidance and support in addition to him allowing me to take the reigns on this project. Dr. Josh Swartz has been integral in this project in terms of getting it off of the ground, mentorship, and ligand synthesis. I would also like to thank

Kim Fong for providing plasma and I would like to thank Shellie Richards for critical comments concerning my original manuscript. Finally, I would like to thank the board of directors from Digital Media Interactive, LLC, as they allowed me to use their commercially available Color Companion iPhone application in my manuscript concerning this work.

## Chapter V

### COFFEE RINGS AS LOW-RESOURCE DIAGNOSTICS: DETECTION OF THE MALARIAL BIOMARKER *PLASMODIUM FALCIPARUM* HISTIDINE-RICH PROTEIN-II USING A SURFACE COUPLED RING OF NI(II)NTA GOLD-PLATED POLYSTYRENE MICROPARTICLES

#### Abstract

This chapter elucidates a novel, low-resource malaria diagnostic platform inspired by the coffee ring phenomenon, selective for *Plasmodium falciparum* Histidine-Rich Protein 2 (*Pf*HRP-II), a biomarker indicative of the *P. falciparum* parasite strain. In this diagnostic design, a recombinant HRP-II (rcHRP-II) biomarker is sandwiched between 1  $\mu\text{m}$  Ni(II)Nitrilotriacetic acid (NTA) gold-plated polystyrene microspheres (AuPS) and Ni(II)NTA-functionalized glass (111). After reacting rcHRP-II malaria biomarkers with Ni(II)NTA-functionalized particles, a 1  $\mu\text{L}$  volume of the particle-protein conjugate solution is deposited onto a functionalized glass slide. Drop evaporation produces the radial flow characteristic of coffee ring formation and particle-protein conjugates are transported toward the drop edge, where, in the presence of rcHRP-II, particles bind to the Ni(II)NTA-functionalized glass surface. After evaporation, a wash with deionized water removes non-specifically bound materials, while maintaining the integrity of the surface-coupled ring produced by the presence of protein biomarker. The dynamic range of this design spans three orders of magnitude and rings are visible with the naked eye down to 10 pM protein concentrations, an order of magnitude below the 100 pM *Pf*HRP-

II threshold recommended by the World Health Organization (WHO). This robust, antibody-free assay offers a simple user interface and clinically relevant limits of biomarker detection, two critical features required for a low-resource malaria detection.

## **Introduction**

The previous chapter elucidates the Ni(II)NTA Au and AgNPs as platform sensors for malaria diagnostics. One of the biggest shortcomings is that the sensitivity falls outside of clinically relevant ranges for rCHRP-II detection. In this chapter, the design of an antibody-free format for a malaria test based on the everyday phenomenon that form coffee ring stains on a kitchen counter is described. The ability to capture and concentrate a biomarker using a ring of particles not only enhances assay sensitivity, but an untrained user would be able to diagnose malaria in times comparable to existing rapid diagnostic tests. As originally described by Deegan and coworkers, evaporating colloidal drops contain an outwardly-directed radial flow to replenish solvent which evaporates at a greater rate from the edge of the drop. These radial flows transport materials in solution to the periphery of the drop where they become concentrated and form a characteristic ring pattern (112-114). Earlier studies have shown that drying drops containing biological material form patterns with possible applications for separations and diagnostics (115-122). However, none of these publications fully apply their assay to detection of biomarkers in a low-resource setting, often requiring the use of a fluorescence microscope and other laboratory equipment.

In this investigation, a simplified enzyme-linked immunosorbent assay (ELISA) format overcomes the sensitivity obstacles established in the previous chapter by

coupling particles to a functionalized glass surface at the edge of an evaporating drop only in the presence of the *Pf*HRP-II malaria biomarker. The design incorporates a unique and robust Ni(II)NTA Au-plated polystyrene microsphere (AuPS) platform and a simple water wash step after evaporation to rinse non-specific materials from the glass surface, leaving behind a visibly detectable ring indicating a positive test result. Figure 28 outlines a proposed strategy for ring formation in the presence of malaria biomarker, where recombinant HRP-II (rcHRP-II) is first reacted and sandwiched between Ni(II)NTA AuPSs in solution (Figure 28). Next, this biomarker-particle conjugate solution is deposited onto a Ni(II)NTA-functionalized glass slide and allowed to evaporate, where the natural radial flow transports the particles to the drop edge, elucidating a ring (Figure 28B). The final water rinse step after evaporation maintains the integrity of the ring in the presence of rcHRP-II, whereas non-specific materials are washed away from the surface. After rinsing, the protein biomarker remains sandwiched between the Ni(II)NTA-functionalized particles and glass slide, elucidating a ring of particles (Figure 28C). The results presented in this report demonstrate detection of the recombinant malaria biomarker at a clinically relevant limit of detection.

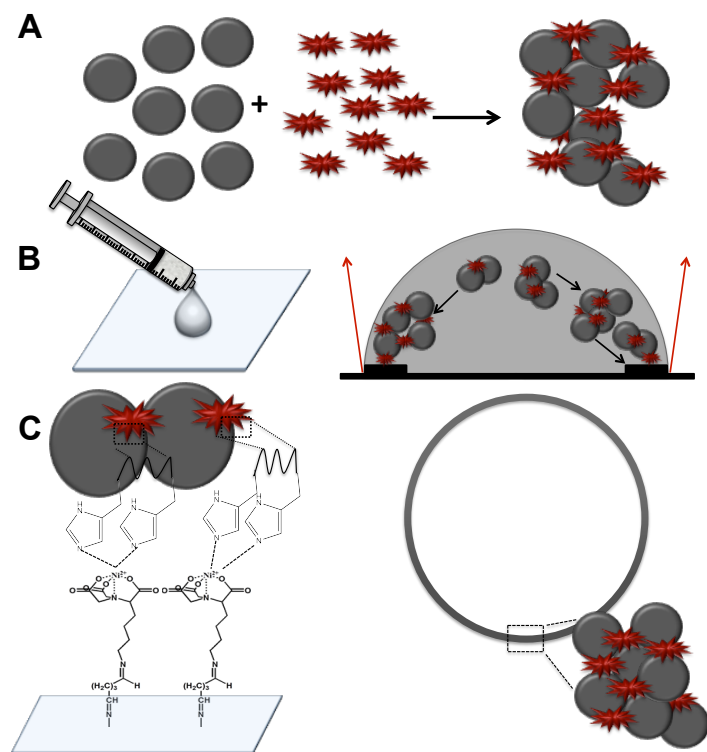


Figure 28. Proposed strategy of ring formation for rHRP-II detection using Ni(II)NTA AuPSs. (A) A solution of Ni(II)NTA AuPSs is reacted with rHRP-II, inducing crosslinking between particles, and ultimately aggregation. (B) A small volume of this particle-protein aggregate solution is deposited onto a Ni(II)NTA-functionalized glass slide (left) and allowed to dry. The right animation displays that evaporation occurs the most rapidly at the edge of the drop (red arrows), so that fluid from the center of the drop migrates to the edge to compensate for the sudden evaporative loss. As a result, a surface tension gradient is created, hereby pulling the particle-protein conjugates towards the edge and forming a ring. (C) After the drop fully dries, the glass is washed with deionized water, and the integrity of the ring is maintained because the rHRP-II is sandwiched between the Ni(II)NTA-functionalized glass and Ni(II)NTA-functionalized AuNPs, mimicking an enzyme-linked immunosorbent assay. The left animation is a side view upon washing the glass, elucidating the coordination of the histidine residues on rHRP-II to Ni(II)NTA on the glass. The animation on the right is a top view, displaying a ring elicited by the formation of aggregated Ni(II)NTA AuPSs.

## Materials and Methods

### *Materials and reagents*

Ni(II)NTA-functionalized glass was purchased from Xenopore. 1.1  $\mu\text{m}$  amine-terminated polystyrene spheres were purchased from Life Technologies Corporation (Invitrogen). Micron-sized beads were also purchased from Spherotech, Polysciences Inc., and Bangs Laboratories. Recombinant *P. falciparum* Histidine-Rich Protein-II containing a glutathione-S-transferase (GST) fusion tag was obtained from CTK Biotech. Human serum albumin (HSA), GST, and  $\alpha$ 2-Macroglobulin (A2M) were purchased from Sigma-Aldrich. Thiol-dPEG<sub>4</sub>-acid was purchased from Quanta Biodesign. N-Cyclohexyl-2-aminoethanesulfonic acid (CHES) and 2-(N-morpholino)ethanesulfonic acid (MES) buffers were purchased from Sigma. All other reagents are of analytical grade and used as received from either Sigma-Aldrich or Fisher Scientific. Ultrapure water with a resistivity greater than 18 M $\Omega$ •cm was used for all experiments.

### *Instrumentation*

Transmission electron microscopy (TEM) images were captured using a Phillips CM20 microscope at 200 kV. Size distributions of suspended particles were determined by dynamic laser scattering (DLS) using a Malvern Nano Zetasizer. Spectral characterization was performed on either an Agilent 8453 UV-vis spectrophotometer or a Bio-Tek Synergy H4 plate reader. Ring images were captured with a 2X objective on a Nikon TE2000U inverted microscope with a charge coupled device (CCD) camera (Hamamatsu Photonics model C7780-20).

### *Synthesis of THPC-functionalized AuNP seeds*

2-4 nm tetrakis(hydroxymethyl)phosphonium chloride (THPC) functionalized AuNPs were synthesized in a 100 mL round bottom flask by combining 500  $\mu$ L of 1 M NaOH and 1 mL of 0.95% (v/v%) THPC to 45 mLs DI H<sub>2</sub>O. To the vigorously stirred solution, 10 mLs of 5 mM HAuCl<sub>4</sub> was added rapidly, changing the color from clear to dark brown in seconds. The solution was stirred for an additional minute and the pH was decreased to 5.5 with concentrated hydrochloric acid.

### *Synthesis of Au-plated polystyrene microspheres (AuPSs)*

The plating of gold nanoshells, first pioneered by Halas *et al.*, has been subsequently modified to accommodate 1  $\mu$ m polystyrene spheres (123-127). A seed mediated adsorption onto polystyrene was achieved by combining a 5 mL solution of stock THPC-functionalized AuNPs (pH 5.5) to a 25  $\mu$ L stock solution (45 pM) of amine-terminated polystyrene microspheres. After stirring vigorously for 24 hours, the solution was centrifuged at 1200 gs (3400 RPM) for 10 minutes. The polystyrene spheres were washed by decanting the AuNP supernatant and suspending in 5 mL H<sub>2</sub>O. This process was repeated four additional times, in which the final AuNP-seeded polystyrene particle suspension was 25  $\mu$ Ls in H<sub>2</sub>O. To achieve a uniform gold nanoshell encompassing the polystyrene microsphere, an electroless plating solution was first prepared separately by dissolving 50 mgs of K<sub>2</sub>CO<sub>3</sub> in 185 mLs DI H<sub>2</sub>O and stirring for 5 minutes. Next, 15 mLs of 5 mM HAuCl<sub>4</sub> was added to the solution and stirring ceased. Over the course of 30 minutes, the solution turned from light yellow to clear, indicating the reduction of Au(III) to Au(I). This solution was aged overnight in the dark to prevent photocatalytic reduction



of Au(I) to Au(0). In a conical tube, 25  $\mu\text{L}$ s of the AuNP-seeded polystyrene spheres were suspended in 5 mLs of the aged electroless plating solution before adding 10  $\mu\text{L}$ s of 37% formaldehyde to promote the reduction of Au(I) onto the AuNPs adsorbed to polystyrene. This solution was vortexed for 2 minutes and subsequently turned black, indicating the plating of a thin gold nanoshell encompassing the polystyrene. Next, the 5 mLs of solution was centrifuged for 5 minutes at 1200 gs. The supernatant was then decanted and the Au-plated particles were suspended in 3 mLs DI  $\text{H}_2\text{O}$ . The centrifugation process was repeated three additional times before suspending in 1 mL DI  $\text{H}_2\text{O}$  to achieve a 1 pM particle concentration.

#### *Synthesis of Ni(II)NTA AuPSs*

To achieve a Ni(II)NTA recognition platform, a 5 mM concentration of Thiol-dPEG<sub>4</sub>-acid was mixed with 5 mM of a modular, thiolated NTA ligand that was previously synthesized in our lab (80). To the 1 pM Au-plated polystyrene suspension, 10  $\mu\text{L}$ s (100  $\mu\text{M}$  total ligand) of the ligand solution was added and incubated overnight. Three washes were performed by centrifuging the particles at 1200 gs for 5 minutes and resuspending in 3 mLs of water. The NTA-functionalized particles were suspended in 1 mL 0.1 M CHES buffer (pH 9.0) and 100  $\mu\text{M}$   $\text{NiCl}_2 \cdot 6\text{H}_2\text{O}$  was added. The particles were incubated overnight and subsequently washed four times at 1200 gs for 5 minutes with water.

### *Quantifying Gold Concentrations on AuPSs*

In order to quantify the average gold concentration on each polystyrene particle, 100  $\mu\text{L}$  aliquots of 1 pM suspensions of AuNP-seeded polystyrene particles and  $\text{NH}_2$ -terminated polystyrene spheres were treated with 400  $\mu\text{L}$  of 8 mM KCN and agitated for 15 minutes. Next the particles were centrifuged at 16,100 gs for 5 minutes and the supernatant was decanted. The supernatant was then filtered through a 0.22  $\mu\text{m}$  filter. The UV spectrum of the  $\text{K}[\text{Au}(\text{CN})_2]$  complex has known extinction coefficients at 204, 211, 230, and 240 nm (128,129). In order to quantify the average gold concentration on each AuPS, a 50  $\mu\text{L}$  aliquot of a 1 pM suspension of AuPSs was treated with 450  $\mu\text{L}$  of 8 mM KCN and agitated for 15 minutes. Next the particles were centrifuged at 16,100 gs for 5 minutes, the supernatant was then decanted, and filtered through a 0.22  $\mu\text{m}$  filter. The UV spectrum of the  $\text{K}[\text{Au}(\text{CN})_2]$  complex was then measured with an Agilent 8453 spectrophotometer.

### *Dynamic Laser Light Scattering Assays with Ni(II)NTA AuPSs*

A 90  $\mu\text{L}$  aliquot of 1 pM Ni(II)NTA AuPSs suspended in 0.1 M MES buffer containing 125 mM imidazole and 0.02% Tween 20 (pH 5.5) was reacted against 10  $\mu\text{L}$  of a protein solution for 15 minutes. Afterwards, size distribution profiles of the particles were taken where an average hydrodynamic particle diameter was determined.

### *Ring assays with Ni(II)NTA AuPSs*

A 1 pM concentration of Ni(II)NTA AuPS containing 0.02% Tween 20 was reacted against varying concentrations of rHRP-II and GST for 15 minutes at pH 5.5.

Afterwards, 1% glycerol was added to the solution and a 1  $\mu\text{L}$  suspension of the microsphere-protein conjugate was pipetted onto a Ni(II)NTA glass slide and allowed to evaporate for one hour, yielding a total assay time of 75 minutes. Afterwards, the glass slides were rinsed thoroughly with water and the glass was subsequently imaged with Image Pro Plus (v. 7).

#### *Ring image analysis for polystyrene spheres and 15 nm AuNPs*

The distribution of the Ni(II)NTA particle aggregates in evaporated droplets was analyzed using Image Pro Plus (v. 7) processing software by representing the AuNPs within the image as positive pixel density or signal intensity. Background noise is determined by measuring intensity in four predefined areas of interest (AOI) at the corner of each image. Signal intensity is measured with two concentric, pre-defined AOIs: an outer AOI that includes the entire drop, and an inner AOI centered inside the drop. After subtracting background noise, ring annulus intensity is calculated by subtracting the inner AOI from the outer AOI. Signal, defined as the presence of a ring, is calculated by dividing the ring annulus intensity by the ring annulus intensity of the blanks. Signal values are normalized so a value of one corresponds to minimum ring formation.

## **Results**

#### *Choosing a microparticle platform for the coffee ring assay*

The coffee ring-inspired assay for biomarker detection is built off of the work elucidated in the dissertation by Joshua Swartz (130). Originally, rcHRP-II is titrated against 15 nm Ni(II)NTA AuNPs and the protein-particle conjugate solution is deposited

onto the Ni(II)NTA-functionalized glass (Figure 29). Although this assay possesses a narrow dynamic range (48-88 nM) outside of clinically relevant limits of detection for *Pf*HRP-II, these results generate significant insight for enhancing future assay performance. Below 48 nM rcHRP-II, there is not enough protein to anchor the particles to the glass. This limitation is also attributed to the low individual surface area of gold nanoparticles. Above 88 nM rcHRP-II concentrations, rings are not evident because the dense gold aggregates settle to the center of the drop faster than radially flowing to the drop edges.

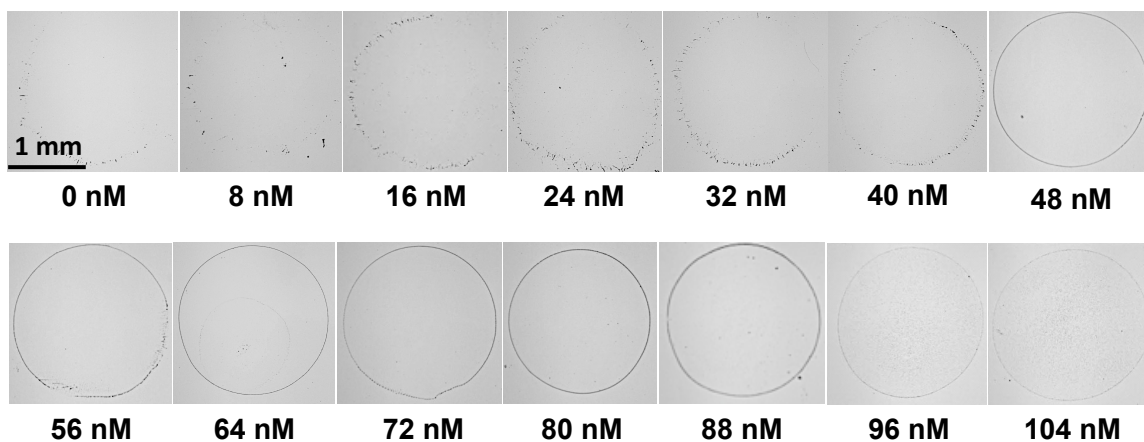


Figure 29. Titration of rcHRP-II against 15 nm Ni(II)NTA AuNP rings. (Reproduced from the dissertation of Dr. Joshua Swartz). A 2 nM concentration of Ni(II)NTA AuNPs containing 0.020% Tween 20 and 1.75% glycerol was reacted with varying concentrations of rcHRP-II for 15 minutes. Afterwards, a 0.5  $\mu$ L drop was deposited onto a Ni(II)NTA AuNP slide and allowed to evaporate. The images presented here are representative of rings after washing with deionized water.

According to Stokes' equation for the settling rate of a spherical particle suspended in solution,

$$v_s = \frac{2(\rho_p - \rho_f)gR^2}{9\mu},$$

where  $v_s$  is the settling velocity in m/s,  $\rho_p$  is the particle density,  $\rho_f$  is the fluid density,  $g$  is the gravitational constant,  $R$  is the particle radius, and  $\mu$  is the fluid viscosity. Above 88 nM protein concentrations, where the vast majority of the beads settle to the center of the drop, 270 nm AuNP aggregates (measured via dynamic light scattering) settle at a velocity of  $7.3 \times 10^{-5}$  cm/s. It is hypothesized that a larger bead would increase assay sensitivity because it contains a greater two-dimensional surface area than a nanoparticle. Micron-sized particles are an attractive alternative for this assay because they are commercially available, spherical, monodisperse, and can be appended with a variety of surface functionalities. However, the particle must be lightweight and cannot exceed a density of approximately 2.0 g/mL for the coffee ring-inspired assay to function, as hypothesized by substituting the settling velocity value of aggregated 15 nm AuNPs into the Stokes equation to solve for particle density of a micron-sized bead. Gold possesses a density of 19 g/mL, while iron oxide (8 g/mL), silica (2 g/mL), and proprietary magnetic Dynabeads (2.5 g/mL) all possess densities outside of the desired range. Since organic microspheres are light, polystyrene is a suitable choice, possessing a density of 1.06 g/mL with monodisperse and spherical characteristics. In order to maintain the integrity of our well-characterized Au/Ni(II)NTA interface, tailoring a thin gold nanoshell encompassing a polystyrene sphere would add an inert element, capable of reducing non-specific interactions.

### *Synthesis of AuPSs*

The microparticle synthesis begins with a seed-mediated approach by first electrostatically adsorbing 2-4 nm THPC-functionalized AuNPs onto amine-terminated

polystyrene microspheres purchased from Invitrogen, followed by reducing Au(I) onto the adsorbed AuNPs with the reducing agent, formaldehyde (Figure 30). The subsequent oxidation and dehydrogenation of formaldehyde is facilitated in the presence of a catalytic metal such as gold (131), so that the product is a tailored, thin gold nanoshell encompassing the polystyrene. Upon reacting the amine-terminated polystyrene spheres with THPC-functionalized AuNPs, the color of the solution changes slightly from bright to dark yellow, and TEM images display the THPC-functionalized AuNP seeds adsorbed to the surface of the amine-terminated microspheres (Figure 31). AuNP-seeded polystyrene spheres then undergo an electroless plating deposition in the presence of AuOH, where TEM images reveal a thin gold nanoshell encompassing the polystyrene (Figure 31C). There are an average of  $8.3 \times 10^8$  total Au atoms/particle, as determined by UV-vis spectroscopy, equating to an average density of 1.49 g/mL and an average particle settling velocity of  $3.2 \times 10^{-5}$  cm/s (Appendix D).

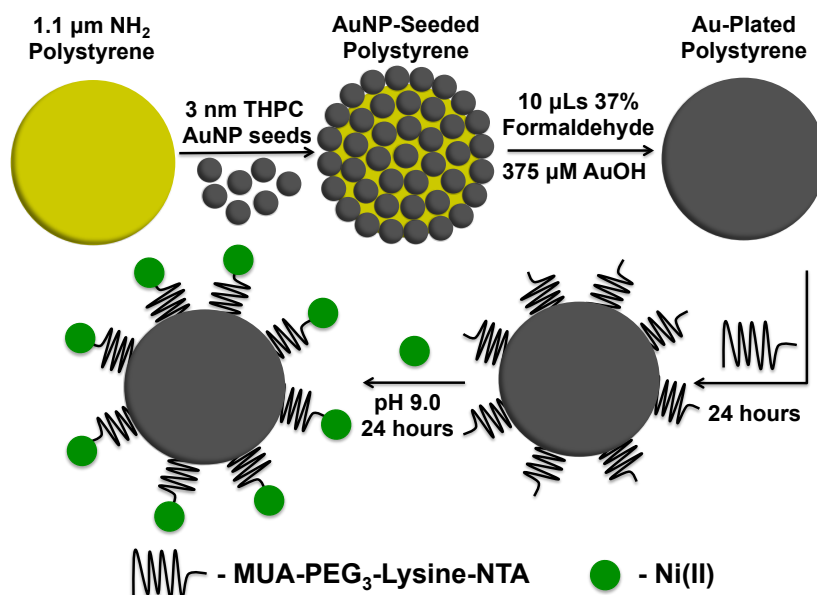


Figure 30. Proposed synthesis of Ni(II)NTA AuPSs.

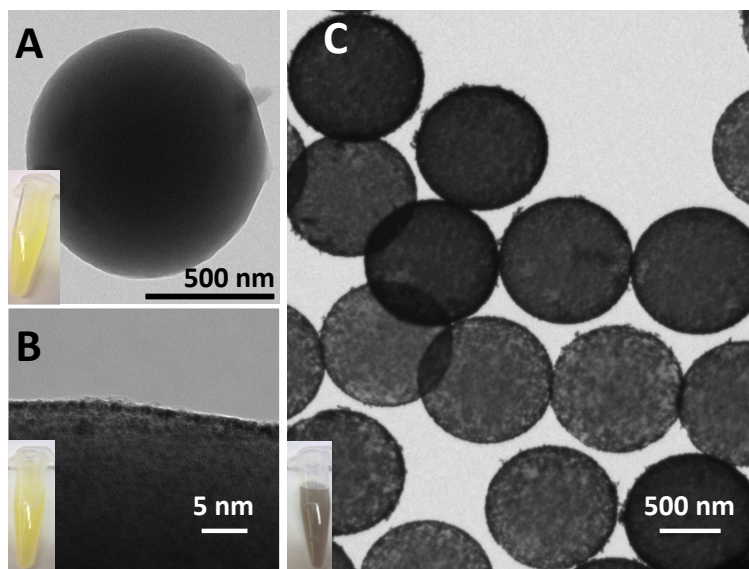


Figure 31. Characterization of AuPSs upon addition of AuNP seeds and Au plating. TEM images of (A) an amine-terminated polystyrene sphere, (B) the surface of a polystyrene sphere with adsorbed 2-4 nm AuNPs, and (C) Au-plated polystyrene spheres (AuPSs). The pictures inset on the bottom left of each image show the color of a 1 pM suspension of each type of microsphere.

#### *Aggregation assays with Ni(II)NTA AuPSs*

The modular alkanethiol-peg-Ni(II)NTA ligand provides an ideal, validated recognition element to create the particle/biomarker capture interface. The Ni(II)NTA recognition ligand is incubated in a 50:50 ratio with the Peg<sub>4</sub>-thiol spacer ligand, as this spacer ligand has demonstrated the highest stability, elucidated in Chapter IV. Upon functionalization with this Ni(II)NTA recognition element, the particles are stable and monodisperse, as shown by TEM images (Figure 32). When the Ni(II)NTA AuPSs are reacted with rCHRP-II at pH 5.5, significant aggregation is first observed at high rCHRP-II concentrations via Ni(II)-histidine crosslinking between rCHRP-II and the particles, as shown by TEM images and dynamic laser light scattering experiments (Figures 32B-D). Dynamic laser light scattering also validates the specificity of the Ni(II)NTA ligand

appended to the gold nanoshell towards the biomarker, as a shift in size distribution of the Ni(II)NTA AuPSs is insignificant when reacted at the physiological concentrations of HSA (37 mg/mL) and  $\alpha_2$ -Macroglobulin (A2M, 2 mg/mL) (Figures 32C-D). Controls against the fusion protein, Glutathione-S-Transferase (GST), show no aggregation, highlighting the specificity of the Ni(II)NTA/Au interface towards the biomarker.

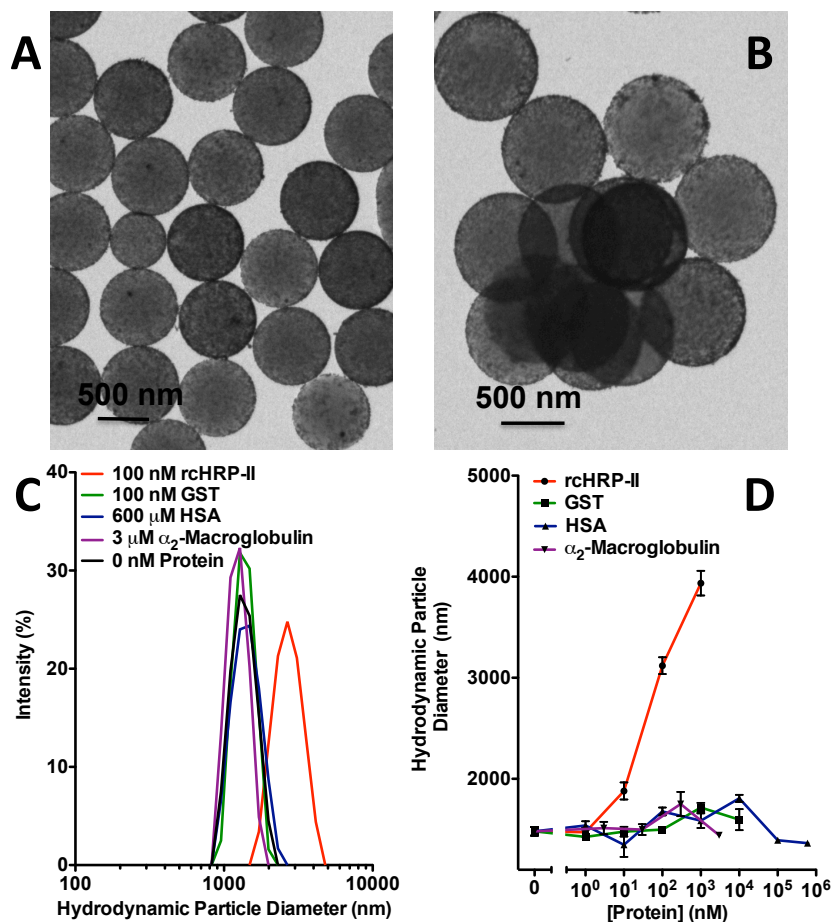


Figure 32. Aggregation activity and specificity of Ni(II)NTA AuPSs. TEM images of Ni(II)NTA AuPSs (A) before and (B) after addition of 1  $\mu$ M rCHRP-II. (C) Dynamic laser light scattering size distribution profiles of Ni(II)NTA AuPSs in the presence of various confounding proteins at their respective physiological concentrations. (D) Titrations of rCHRP-II in addition to confounding proteins as measured by dynamic laser light scattering.



### *Ring assays with a 1.1 $\mu\text{m}$ Ni(II)NTA AuPS platform*

After plating a thin nanoshell onto a polystyrene microsphere, the density of the bead jumps to approximately 1.5 g/mL, still below the 2.0 g/mL density threshold. Validation of this density model is demonstrated for micron-sized magnetic Dynabeads (2.5 g/mL density) and the gold-plated polystyrene spheres (1.5 g/mL density) under identical drop conditions (Figure 33).

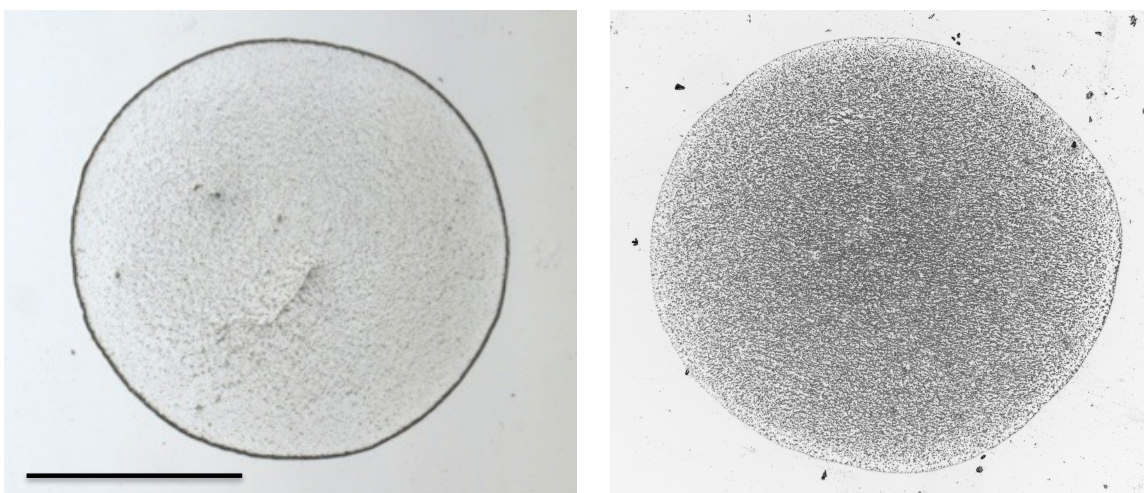


Figure 33. Microparticle flow patterns at different densities. One  $\mu\text{L}$  drops deposited onto a Ni(II)NTA slide containing 0.020% Tween 20 and 1% glycerol, where the drop on the left is a 1 pM concentration of 1  $\mu\text{m}$  Ni(II)NTA Au-plated polystyrene (1.5 g/mL density), while the image on the right is a 1 pM concentration of a 1  $\mu\text{m}$  Co(II)NTA magnetic Dynabead (2.5 g/mL density). The black bar on the left scales to 1 mm.

It is clearly evident that nearly all of the Dynabeads settle to the center of the drop rather than radially flow to the drop edges. The denser Dynabeads settle three times faster at a rate of  $8.2 \times 10^{-5}$  cm/s compared to the Au-plated polystyrene spheres ( $2.7 \times 10^{-5}$  cm/s). Considering the lightweight nature of polystyrene and its density is barely above that of water, organic beads are a suitable option for this coffee ring-inspired assay.

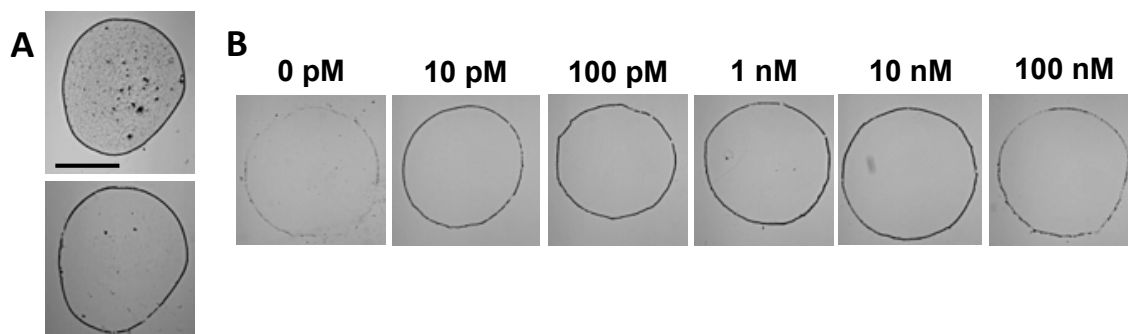


Figure 34. Ni(II)NTA AuPS ring assay for detection of rcHRP-II. (A) A 1 pM solution of Ni(II)NTA AuPSs containing 0.02% Tween and 1% glycerol is reacted with 10 nM rcHRP-II and a 1  $\mu$ L drop is deposited on a Ni(II)NTA-functionalized glass slide. After one hour, the slide is rinsed thoroughly with deionized water. The top image shows the drop before washing while the bottom image shows the drop after washing in the presence of rcHRP-II biomarker. The black bar scales to 1 mm. (B) Logarithmic titration of rcHRP-II using the above conditions. The images show an example of the rings after washing.

After demonstrating that the Ni(II)NTA AuPSs form rings, they are evaluated in the coffee ring assay. After 15 minutes of incubation of the Ni(II)NTA AuPSs with rcHRP-II, the particle-protein conjugate solution is deposited onto a Ni(II)NTA-functionalized glass slide, and the drop edge is pinned to the glass surface via topographical and chemical heterogeneities. As evaporation is greatest at the drop edge, solution from the middle of the drop migrates toward the contact line to compensate for the rapid fluid loss. Suspended Ni(II)NTA AuPS-protein conjugates flow radially towards the drop edge and accumulate at the contact line, as shown by images of a drop of particles at different time points during evaporation (Appendix D). When rcHRP-II is present, the particles are captured by the functionalized glass surface. Rinsing the glass slide with deionized water after depositing and evaporating 1  $\mu$ L of a AuPS-protein conjugate solution washes away non-specific binding on the surface (Figure 34). At 10 nM rcHRP-II concentrations, the integrity of the ring is maintained via conjugate

coupling to the Ni(II)NTA glass surface (Figure 34A). In the presence of rcHRP-II, the polystyrene spheres exhibit ring formation spanning over three orders of magnitude of target biomarker after washing (Figure 34B). The titration of rcHRP-II with Ni(II)NTA AuPSs exhibits an optical detection limit of 10 pM rcHRP-II concentrations. The assay signal intensity increases linearly after 10 pM rcHRP-II before saturating between 100 pM and 10 nM concentrations. At the high concentration regime of the assay, 100 nM rcHRP-II concentrations aggregate the particles, so that the protein-particle conjugates settle vertically ( $6.0 \times 10^{-5}$  cm/s) to the center of the drop rather than radially flowing towards the edge upon drop deposition. Upon washing, the large aggregates are displaced, as there is not enough particle surface area contact with the Ni(II)NTA glass to coordinate the particle-protein conjugates to the surface, resulting in faint rings. Image processing further allows for quantitation and validation of the assay, as indicated by a titration curve between 10 pM and 10 nM rcHRP-II concentrations (Figure 35). Non-specific interactions are evaluated with the fusion protein, GST. Particle aggregation does not occur in the presence of GST and ring signal generated upon reactions with GST does not exceed the background noise. Finally, overlaid is the signal generated from the 15 nm Ni(II)NTA AuNP ring assay, where the dynamic range is clearly limited to the mid nanomolar concentration regime.

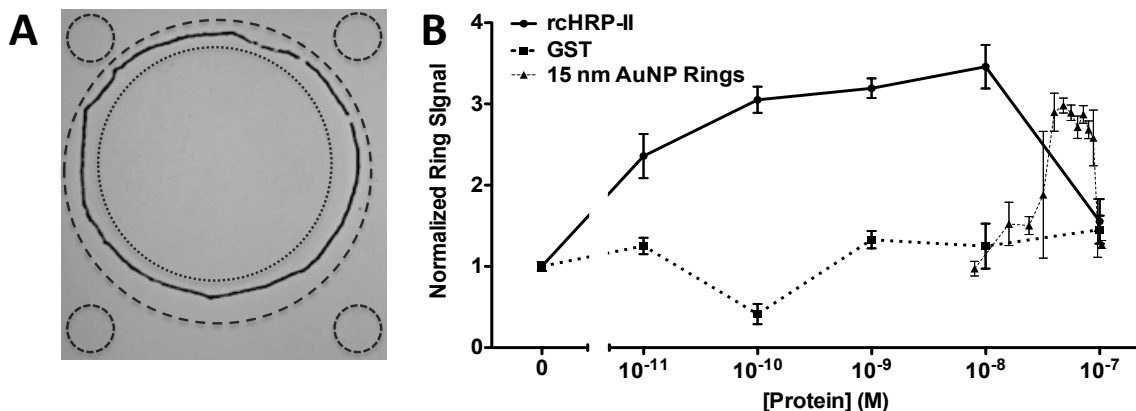


Figure 35. Analysis of ring formation upon titrating rcHRP-II with Ni(II)NTA AuPSs. (A) Ring signal generated by subtracting the intensity of the inner circularly dotted annulus from the outer dashed annulus with respect to the minimum mean background (four dashed corner circles). The solid ring in the image is an example of concentrated Ni(II)NTA AuPSs in a ring in the presence of rcHRP-II after washing. (B) Compiled signal intensity generated from the difference between the dotted annulus inside of the ring with from the dashed outer annulus with respect to the minimum mean background signal. Also overlaid is the signal analysis from the 15 nm Ni(II)NTA AuNP ring assay in Figure 29, showcasing its small dynamic range.

## Discussion

### *Rationale behind Ni(II)NTA AuPS ring assay performance*

This simple antibody-free design originally inspired by the coffee ring phenomenon overcomes many of the obstacles associated with existing RDTs by manipulating the molecular recognition interface for optimum specificity and improved sensitivity. The ring assay simplifies an ELISA by eliciting a chromogenic response from concentrated polystyrene microspheres. In our low-resource design, a ring of Ni(II)NTA AuPSs sandwich a rcHRP-II malarial biomarker to Ni(II)NTA-functionalized glass via Ni(II)-histidine coordination. Most importantly, the integration of a water wash step after drop evaporation significantly reduces non-specific binding to the glass surface, but maintains the integrity of the strong Ni(II)-histidine coordination in the presence of biomarker. This assay not only detects biomarker concentrations at the operational range

of malaria diagnostics (0.2-1 nM rCHRP-II) recommended by the WHO, but rings are even visible with the naked eye at 10 pM rCHRP-II concentrations. This 10 pM viewable limit of detection is one order of magnitude below the WHO's lower recommended threshold concentration, so that our format possesses utility diagnosing malaria in asymptomatic patients. At the high concentration regime, the assay's ring signal decreases due to particle aggregation and gravitational vertical settling to the center of the drop. However, it has been determined that for adults and children infected with uncomplicated and severe malaria, the median concentration of *Pf*HRP-II found in blood is between 1-20 nM protein concentrations (132-134), which is the most sensitive regime of our assay.

To achieve a detection limit below 0.1 nM *Pf*HRP-II concentrations using a microfluidic ring assay, an aqueous polystyrene microsphere is a desirable particle platform because of the high degree of uniformity, low density, and large particle surface area. The low density of the spherical, monodisperse particle favors ring formation, while the large surface area creates a viewable two-dimensional ring that provides the assay's signal. A spherical, monodisperse bead also provides reproducible and predictable particle flow in evaporating drops, so the assay can be easily tuned and manipulated. In addition, coating the polystyrene particle in a gold nanoshell to promote facile thiol-based ligand functionalization offers a robust interface that can withstand the extreme conditions encountered in low-resource areas. Finally, this inert gold nanoshell minimizes non-specific interactions and validates the integrity of our previously explored Ni(II)NTA AuNP molecular recognition interface (80).

The introduction of the additives, tween and glycerol, enhances particle stability, reproducible particle flow, and signal-to-noise. It has been previously demonstrated that the incorporation of surfactants and polymers into particle droplet suspensions can promote and prevent ring formation during drop evaporation (135-137). Manipulating such factors lead to improved ring reproducibility and robustness by controlling the rate of evaporation and blocking non-specific substrate binding. In the current format, incorporating 0.02% Tween 20 to the particle suspension maintains particle stability, while aiding in contact line pinning during drop evaporation for reproducible ring sizes. Additionally, the incorporation of 1% glycerol promotes specific Ni(II)-histidine coordination to the glass, but also provides adequate blocking on the functionalized glass surface to limit non-specific binding. In contrast to an ELISA in which proteins are often used to block non-specific sites, our assay takes advantage of the robust hydrogen-bonding network of glycerol/water as a blocking agent, further modifying this assay for use in low-resource areas. Finally, the viscous nature of glycerol reduces the rate of evaporation to optimize kinetics of particle transport to the drop edge for increased signal.

#### *Applying the Ni(II)NTA AuPSs to a low-resource setting*

Thus far, the coffee ring-inspired assay using Ni(II)NTA AuPSs has only functioned with a purified protein sample dissolved in water. However, the likelihood of receiving a patient sample devoid of interfering proteins, small molecules, and buffers is infinitesimal. In order to take the next step, rCHRP-II is dissolved in the most common interfering protein found in blood, HSA. When rCHRP-II is dissolved in physiological

concentrations of HSA (37 mg/mL) and subsequently reacted with Ni(II)NTA AuPSs, the particles do not elicit a characteristic ring upon drop deposition. The solution is too viscous for the particles to produce their natural radial flow patterns for ring formation. Therefore, rcHRP-II needs to be dissolved in 4 mg/mL HSA so that upon reactions with the Ni(II)NTA AuPSs and subsequent drop deposition onto glass, the particles can elicit their natural flow patterns. The titration of rcHRP-II dissolved in 3.7 mg/mL HSA using the Ni(II)NTA AuPS ring assay is able to detect mid-picomolar concentrations of rcHRP-II (Figure 36). Although the assay can detect mid-picomolar quantities of rcHRP-II using the image analysis described in Figure 35, the ring images do contain large amounts of HSA inside the annulus and do not contain the aesthetic appeal as the rings with zero background interferences. The maximum ring signal is only two-thirds of the maximum signal obtained in Figures 34-35. At 3.7 mg/mL HSA, the interfering protein binds non-specifically to the glass, demonstrating that a simple water wash is not able to fully remove all contaminants from the Ni(II)NTA-functionalized glass slide. In addition, the assay conditions are altered significantly in order to yield the highest signal. Even with my “optimized” conditions, the error bars are larger as a result of the large concentrations of background interference on the slide.

However, these results are a step in the right direction towards creating an antibody-free, POC diagnostic because not only are clinically relevant concentrations of rcHRP-II are detectable, the 2 mm diameter rings on the slide can be easily imaged with an iPhone 4S camera (Figure 36C). As portable camera technology improves with every generation of smartphone, the image processing applications also improve. Moving

forward, innovative strategies and multiple perspectives are required, opening up avenues in sample preparation and new particle applications.

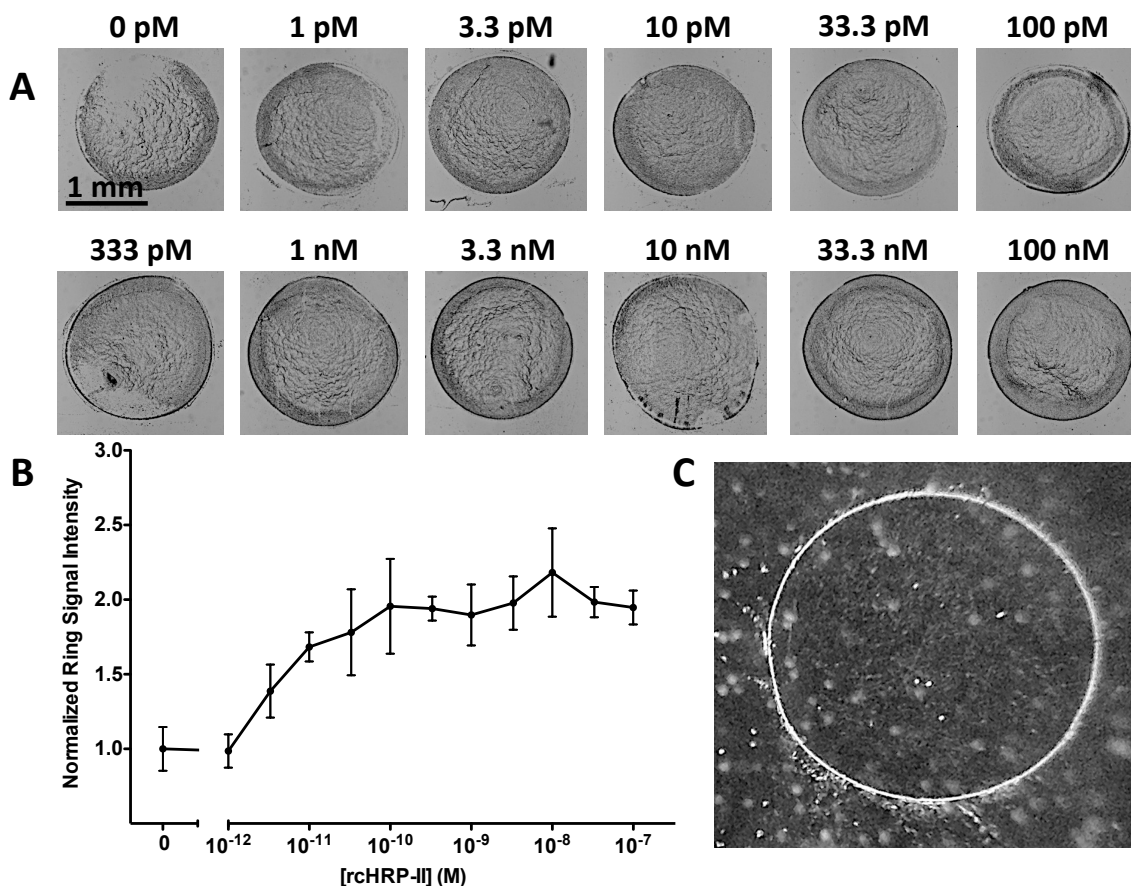


Figure 36. Ni(II)NTA AuPS ring assay upon dissolving rcHRP-II in 4 mg/mL HSA, an order of magnitude below physiological protein concentration. (A) Images of Ni(II)NTA AuPS rings after washing with water upon titration of rcHRP-II dissolved in 4 mg/mL HSA. Ni(II)NTA AuPSs are dissolved in 0.020% Tween 20 and 0.025% glycerol. After reacting the rcHRP-II with the Ni(II)NTA AuPSs for 15 minutes, a 1  $\mu$ L drop is deposited onto a Ni(II)NTA-functionalized glass slide and allowed to dry. The drying time for this assay consists of 16 hours (overnight). (B) Ring analysis using the aforementioned methods in Figure 35. (C) Image of a Ni(II)NTA AuPS ring on Ni(II)NTA-functionalized glass using a cell phone camera (iPhone 4S).



## Conclusion

The coffee ring inspired diagnostic strategy described in this work delivers a unique approach for overcoming challenges associated with existing rapid diagnostic tests, particularly in low-resource settings. Enabled by the stable Au-thiol interface and the monodisperse, spherical distribution of colloidal gold nanoparticles, rings of 1  $\mu\text{m}$  Ni(II)NTA AuPSs detect as little as 10 pM concentrations of the rcHRP-II malarial biomarker, an order of magnitude lower than current diagnostic standards. The inert gold surface provides a stable and selective Ni(II)NTA molecular recognition element towards rcHRP-II that resists the extreme conditions in low-resource regions. The assay offers a simple user interface through complementary Ni(II)-histidine coordination on the glass surface, where the signal is enhanced significantly by reducing background noise with a final water wash. Overall assay performance is additionally enhanced through the judicious use of additives. Furthermore, applying the image processing algorithms upon ring identification to cell phone technology has the potential to further enhance the simple user interface and reduce user bias in low-resource settings. However, when a complex matrix is introduced to the ring assay, the Ni(II)NTA AuPSs display high picomolar limits of rcHRP-II detection and still contain a high background signal. Nevertheless, the assay time required to generate positive or negative results is comparable to currently available RDTs, so that coupling this format to a self-contained extraction device specific for *Pf*HRP-II from a whole blood matrix would greatly improve the ability of the technique to operate as a malarial diagnostic.

## Section Acknowledgements

I would like to thank the Bill and Melinda Gates Foundation for financial support and Vanderbilt University for providing available resources for laboratory space and instrumentation. I would firstly like to thank Prof. David Wright and Prof. Rick Haselton for spearheading this project. Additionally, I would also like to thank both of them for their guidance, mentorship, and patience in the publishing of this paper. Although the initial experiments began in 2011, a polished article was not published until almost three years later. I am grateful that both of them were willing to work together effectively to keep an open mind about experiments, results, and timelines. I would also like to thank Dr. Josh Swartz, who began the ring experiments with 15 nm AuNPs. His mentorship and guidance facilitated my transition into this project. Additionally I would like to thank Keersten Davis and Dr. Joshua Trantum for being open-minded, allowing me to throw ideas off of them, and assisting with image analysis/editing. I also would like to thank Phoebe Penamon, who began the gold-plating of polystyrene microparticles. Finally, I would also like to thank Alexander Denton for providing insight with respect to spacer ligand assembly on particles and Corey Peak with respect to image analysis. Thanks again to VINSE, which has been integral with respect to the electron microscopy of particles and DLS data in this chapter.

## Chapter VI

### PROOF-OF-CONCEPT OF THE CAPTURE-AND-RELEASE OF THE MALARIAL BIOMARKER *PLASMODIUM FALCIPARUM* LACTATE DEHYDROGENASE

#### **Introduction - Future Directions to Enhance Malarial RDTs**

Chapters IV and V have described the development of innovative particle platform technologies for the detection of the malaria biomarker, *P. falciparum* HRP-II. Devoid of antibodies and thermally sensitive reagents, the 15 nm Ni(II)NTA AuNP platform demonstrates specificity at the cost of sensitivity. To increase sensitivity, micron-sized Ni(II)NTA Au-plated polystyrene spheres capture the malaria biomarker, and upon drop deposition, the particles concentrate and sandwich the biomarker to the glass substrate. Although this assay exhibits excellent sensitivity with a pure protein sample, the assay loses sensitivity in a complex matrix because interfering proteins stick non-specifically to the glass. While I have investigated new methods for rapid detection of *Pf*HRP-II, true innovation is often achieved by improving upon existing technologies. The previous two chapters have highlighted many of the drawbacks of RDTs, specifically their low sensitivities in the developing world. Nonetheless, RDTs continue the persistent technology of sandwiching a biomarker in-between two antibodies and eliciting a chromogenic response, a technique practiced regularly by nearly every molecular biology laboratory for protein identification and quantification.

In this dissertation, I have aimed to create new platform technologies, while my lab members have achieved success in increasing the sensitivity of currently existing

assays. Davis and Gibson have recently shown that by concentrating and purifying *Pf*HRP-II from a whole blood matrix, the limit of detection of many brands of *Pf*HRP-II malarial RDTs are enhanced by an order of magnitude (138). Approximately 20% of the RDTs available on the market meet the 200 parasite/ $\mu$ L threshold recommended by the WHO, while the vast majority fall outside of the necessary detection range. By employing the concentration and purification extraction technology developed by our lab and depositing that sample onto a RDT, six different brands of RDTs were discovered to detect parasites below 50/ $\mu$ L from a whole blood matrix, which is over four times more sensitive than the WHO's recommendation. Currently, the extraction workflow takes approximately 30 minutes of time, followed by another 15-30 minutes to receive results from the RDT. A one-hour timeframe to gain a discernible signal is longer than the 15-30 minute slot recommended by the WHO. However, the ultralow detection limits generated from this technology overcome the sensitivity issues in a low-resource setting, allowing for the tracking of asymptomatic disease carriers and providing a framework for a universal enhancement strategy for RDTs of various diseases.

The preliminary work presented in this chapter provides a one-step platform assay to capture and subsequently release a malarial biomarker. For a downstream malarial diagnostic, the biomarker will be captured, concentrated, and subsequently released onto an RDT for rapid enhancement. In order to provide a proof-of-concept platform to capture a biomarker from a blood sample and release it onto a RDT, I decided to target the malarial biomarker *P. falciparum* Lactate Dehydrogenase (*Pf*LDH). This ubiquitous parasitic protein is secreted into patient's blood samples upon infection like *Pf*HRP-II, but is only present when the parasite is viable in the body (139). *Pf*HRP-II, on the other

hand, can linger in the blood for up to two weeks even after antimalarial drugs eliminate the parasite. Because LDH is essential for glycolysis and aids in the conversion of pyruvate to lactate, successful elimination of the parasite clears this protein immediately, which has advantageous implications in diagnosis before and after drug therapies. The proof-of-concept platform involves a Hexa-Histidine-tagged monoclonal antibody that can specifically capture *Pf*LDH from a whole blood matrix. The histidines appended to the antibody bind Co(II)NTA-functionalized magnetic microbeads for concentrating and purifying the biomarker. A magnet can concentrate and separate the antibody-antigen-functionalized beads so that the biomarker-antibody complex can be released by high concentrations of imidazole (Figure 37). The side chain of histidine, imidazole, possesses micromolar affinity to M(II)NTA, so that at high enough concentrations, imidazole can replace the bound histidine subunits on the beads (M=Co, Ni). Although these preliminary studies are new and do not show enhancement to RDTs just yet, the platform provides a proof-of-concept to capture and release an LDH biomarker from whole blood. Theoretically, this platform can be applied to capture and release a wide variety of biomarkers using catch-and-release microparticle technology.

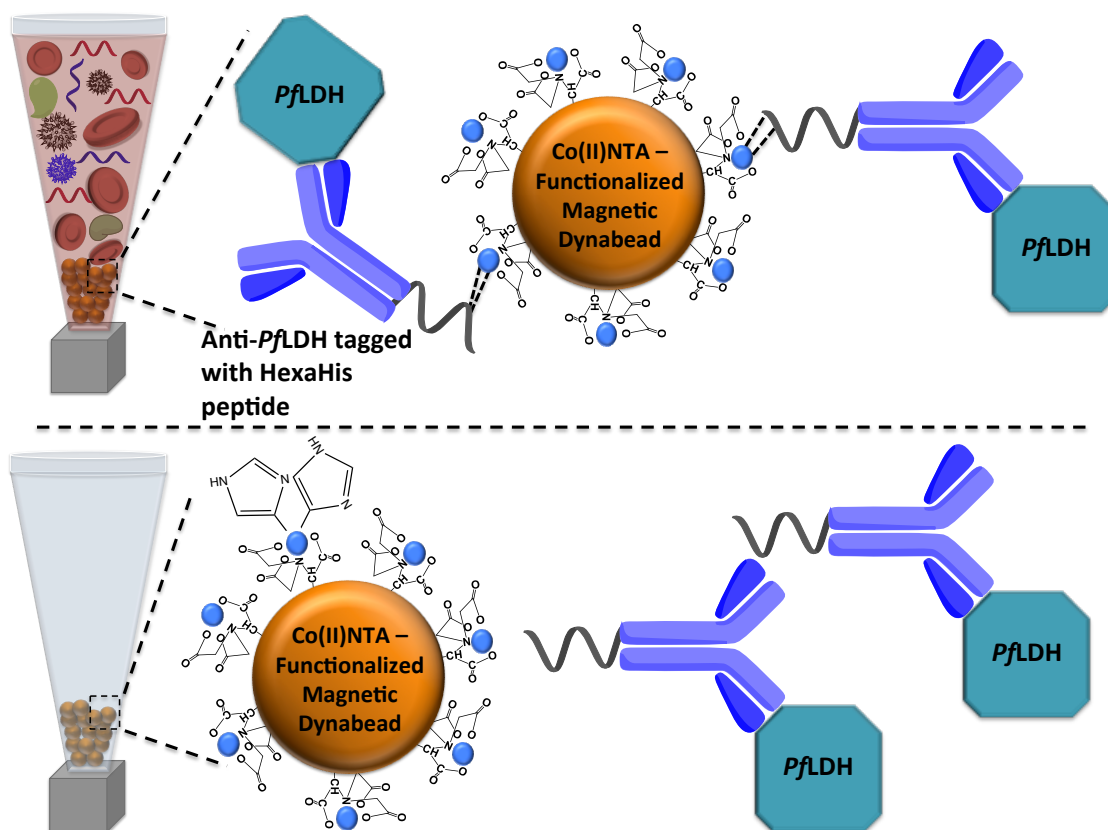


Figure 37. Schematic of capture-and-release of *PflDH*. The top depiction shows the capabilities of a His-tagged antibody binding the Co(II)NTA magnetic beads and extracting the LDH biomarker from a whole blood matrix. The bottom depiction shows that after washing, the antibody-LDH complex can be eluted using high concentrations of imidazole. The imidazole replaces the histidine units and the antibody-LDH complex is partitioned into the pure buffer/imidazole solution.

## Materials and Methods

### *Materials and reagents*

Co(II)NTA-functionalized Dynabeads were purchased from Invitrogen. Fmoc-protected polyethylene glycol (PEG) was purchased from Quanta Biodesign. Fmoc-protected amino acids were purchased from AAPPTec. A cysteine-functionalized Rink Amide resin was purchased from Advanced ChemTech. *PflDH* antigen was purchased from CTK Biotech. *PflDH* monoclonal antibody was purchased from MyBioSource, Inc.

All other reagents were purchased from either Sigma-Aldrich or Fisher Scientific and used without further modification. All deionized water used in this investigation was purified through a 0.22  $\mu\text{m}$  filter at a resistance of 18  $\text{M}\Omega\cdot\text{cm}$ .

#### *Design, synthesis, and characterization of hexa-histidine peptide*

The peptide was designed to possess the following sequence from N-terminus to C-terminus: acetyl-His-His-His-His-His-His-Peg<sub>6</sub>-Cys-amide. Both termini are capped with neutral groups to reduce non-specific interactions and only the free thiol group on the cysteine residue will couple to the antibody. The polyethylene glycol spacer reduces the steric interactions between the antibody and the His tag. Using standard Fmoc solid-phase peptide synthesis, a Rink Amide resin appended with Fmoc-protected cysteine was used as the anchoring substrate. For coupling conditions, a 10X molar excess of reagents (hydroxybenzotriazole, amino acid, and diisopropylcarbodiimide dissolved in dimethyl formamide) was added relative to the resin substitution for one hour. For deprotection conditions, 10 mLs of 20% v/v piperidine dissolved in dimethyl formamide (DMF) was exposed to the resin for 20 minutes. For final N-terminal acetylation, a 10% v/v acetic anhydride, 10% v/v N,N-diisopropylethylamine dissolved in DMF was exposed to the resin for 30 minutes. In-between coupling and deprotection steps, the resin was washed thoroughly with DMF and methanol. Peptide cleavage was performed by exposing the resin to a 90:5:3:2 volume ratio of trifluoroacetic acid:anisole:ethanedithiol:thioanisole for two hours. For every 100 mgs of resin used in the synthesis, 2 mLs of this solution was reacted with the resin. After cleavage, the peptide was filtered using glass wool and precipitated in cold diethyl ether. The pellet

was spun down at 1000 gs for 5 minutes before resuspending in cold ether. This washing process was repeated 4 additional times. After removing the final ether supernatant, the peptide pellet was dried with N<sub>2</sub>. The peptide was then purified with reverse-phase HPLC, and eluted off of a C18 column using a water-acetonitrile gradient. The peptide was lyophilized and characterized via MALDI-MS.

For MALDI-MS analysis, a small millimolar peptide concentration was dissolved in a 50:50 ratio of water and acetonitrile. A 0.5 µL drop of this solution was deposited onto a 100-well MALDI plate. After drying, a 0.5 µL drop of matrix solution (20 mg/mL α-cyano-4-hydroxycinnamic acid) was deposited onto the well with dried peptide and scratched thoroughly to incorporate the peptide into the MALDI matrix. The MALDI-MS operated at an accelerating voltage of 20 kV, a laser intensity of 2000 units, a delay time of 120 ns, grid voltage of 64%, and a shot count of 250. The spectrum shows the protonated peptide along with the peptide-sodium adduct (Figure 38).

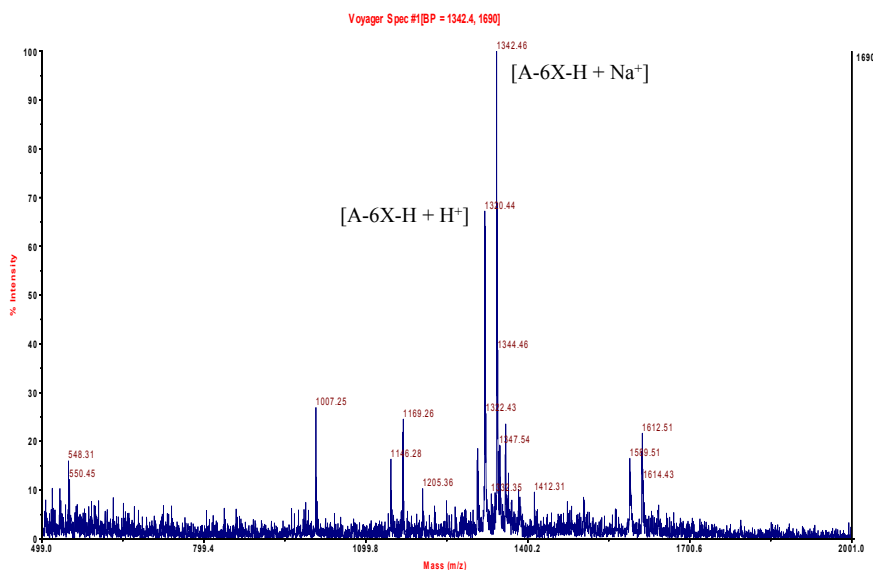


Figure 38. MALDI-MS spectrum of Hexa-His peptide.



### *Coupling hexa-his to PflDH monoclonal antibody*

A 1 mg quantity of 4.2 mg/mL mouse monoclonal antibody (IgG2b isotype) specific for *Pfl*LDH was purchased from MyBioSource, Inc. Aliquots of this protein are stored in a -40°C freezer at volumes of 50 µL and 2 mg/mL concentrations dissolved in phosphate buffered saline (PBS). The peptide coupling was performed using a well-known, water-soluble Sulfo-SMCC coupling reagent (purchased from Thermo Scientific). One end of the Sulfo-SMCC reagent contains a Sulfo-NHS molecule that is reactive for primary amines, while the other end contains a maleimide functional group reactive towards thiol groups. A 40X molar excess of Sulfo-SMCC (20 µL, 534 µM) was reacted with 20 µL of 2 mg/mL *Pfl*LDH antibody for 30 minutes at room temperature. For purification, the activated antibody was purified in a 100k molecular weight cutoff (MWCO) filter and spun down three times at 16,100 gs in a microcentrifuge. The activated antibody (20 µL, 2 mg/mL) containing the surface maleimide group was then reacted with 20 µL of 534 µM Hexa-His peptide overnight. The Hexa-His antibody was purified using 100 MWCO filters as described previously and dissolved in PBS.

### *Malstat assay conditions*

In a 50 mL conical tube, 4.00 g of sodium L-lactate, 1.32 g Tris buffer, and 0.022 g APAD were dissolved in 50 mL deionized water. The pH was adjusted to 9 with concentrated HCl and this solution is referred to as the Malstat reagent. Separately, 0.080 g of the yellow tetrazole (NBT) and 0.004 g PES were dissolved in 50 mLs of Tris buffered saline with 0.050% v/v Tween 20. This is referred to as the NBT/PES solution. In order to perform the assay, 125 µL of the Malstat reagent was added to a 96-well plate

with 25  $\mu\text{L}$  of the NBT/PES solution. Finally, 25  $\mu\text{L}$  of a *Pf*LDH solution (purchased in a recombinant form from CTK Biotech containing a GST tag) was added to the plate and shaken for 30 minutes in the dark. It is important to cover the plate in parafilm and aluminum foil, as the tetrazole dye is sensitive to light. After 30 minutes, the absorbance measurements were immediately read in a Bio-Tek Synergy H4 plate reader at 650 nm to indicate dye turnover catalyzed by *Pf*LDH quantification.

#### *Catch-and-release assay*

In a 1.5 mL Eppendorf tube, 20  $\mu\text{L}$  of 33  $\mu\text{M}$  His-tagged *Pf*LDH antibody was added to a solution of 160  $\mu\text{L}$  of Co(II)NTA Dynabeads (1 mg/mL, purchased from Life Sciences Corporation) and incubated for 10 minutes. Using a magnet, the beads were pulled down and washed three times with PBS containing 0.025% v/v Tween 20. To 50  $\mu\text{L}$  of antibody-functionalized beads (1 mg/mL), 50  $\mu\text{L}$  of lysed whole blood containing varying concentrations of *Pf*LDH was added to the beads. The blood was lysed with 100 mM phosphate, 600 mM NaCl, and 2% Triton X-100, and the protein biomarker dissolved in blood was reacted with the beads for 15 minutes. Afterwards, 4 washes were performed with Tris buffered saline with 0.025% v/v Tween 20. Finally, the *Pf*LDH-antibody complex was eluted from the beads with 100  $\mu\text{L}$  of 450 mM imidazole for 10 minutes. This solution can be quantified via the Malstat assay described previously.

## Results and Discussion

### *Characterization of hexa-his PfLDH antibody*

In order to characterize the Hexa-His coupling to the antibody, bio-layer interferometry is utilized to determine the real-time binding kinetics (Figure 39). Compared to the negative control untagged antibody, significantly more His-tagged antibody loads onto the Ni(II)NTA sensor tips. Histidine units have a high affinity to Ni(II)NTA, so it is hypothesized that more His-tagged antibody would bind to the Ni(II)NTA tips while the untagged antibody binds non-specifically to the tips. More His-tagged antibody is able to immobilize onto the sensor tips, so that a higher quantity of *PfLDH* associates to these His-tagged antibody sensor tips. This experiment reveals that not only is the Hexa-His coupling to the antibody accomplished, but the integrity of the paratope (i.e. molecular recognition region of antibody) is not compromised because more *PfLDH* is able to associate compared to the negative control. Finally, binding occurs instantaneously, which is advantageous in accommodating the WHO's rapid timeframe for disease diagnosis.

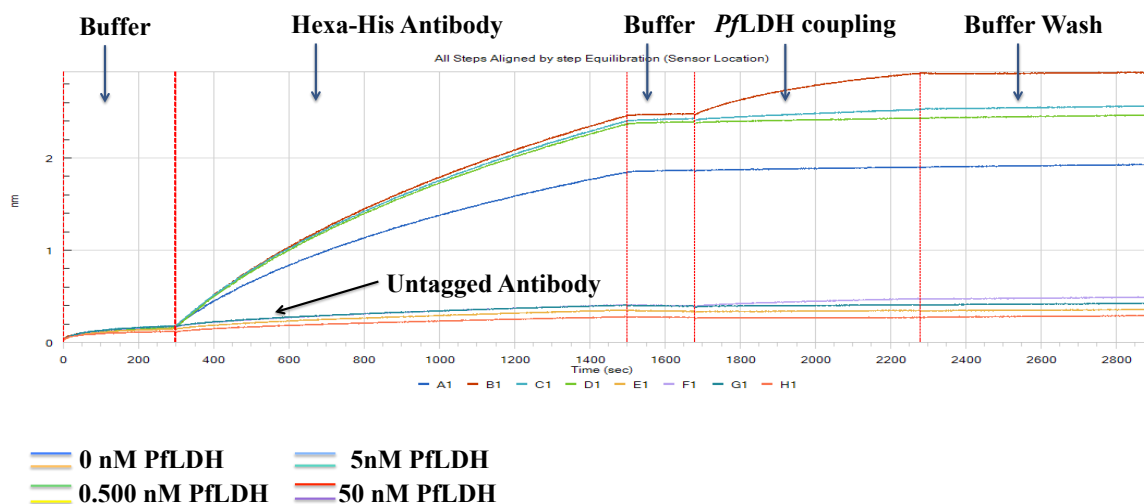


Figure 39. Real-time binding kinetics of Hexa-His antibody to Ni(II)NTA sensor tips. Buffer (PBS containing 0.025% Tween 20) stabilizes the signal for the first five minutes, followed by loading the Hexa-His antibody (25  $\mu\text{g}/\text{mL}$ ) onto four Ni(II)NTA tips for 20 minutes. As a negative control, untagged antibody (25  $\mu\text{g}/\text{mL}$ ) is immersed in four Ni(II)NTA tips for 20 minutes as well. Next, another wash with buffer stabilizes the signal on all eight tips for the next three minutes, so that varying concentrations of *Pfl*LDH can associate to the antibody for 10 minutes. A final buffer dissociates any non-specifically bound material.

#### *Quantifying PflLDH – Malstat assay*

In chemistry and molecular biology, protein levels can be quantified in picomolar quantities using enzyme-linked immunosorbent assays (ELISA). It is the gold standard of protein quantification and recognition because an antigen is sandwiched between two antibodies, resulting in maximum specificity. The secondary antibody is appended with an enzyme, which catalyzes a redox reaction of a small molecule substrate, changing the small molecule's color in solution and generating a concentration-dependent, chromogenic response of an antigen with high sensitivity and ultimate specificity. However, ELISAs are often time-consuming and require skilled expertise to operate them effectively. For quantification of *Pfl*LDH, the Malstat assay takes advantage of the protein's enzymatic activity (140). Human LDH converts L-lactate to pyruvate in the

presence of the coenzyme,  $\text{NAD}^+/\text{NADH}$ , which is found in all human cells. For the malaria parasite to participate in glycolysis, it operates using the coenzyme system, APAD/APADH (141). APAD reduction to APADH can catalyze the formation of a yellow tetrazole to a blue formazan dye in the presence of phenylethyl sulfate, eliciting a concentration-dependent response of LDH (Figure 39). Since human erythrocytes do not contain APAD/APADH, this assay is extremely specific towards detection of *Pf*LDH in human blood. For the purpose of this platform design, the 30-minute Malstat assay time is significantly less in comparison to a four-hour ELISA, and also provides a reproducible and consistent signal.

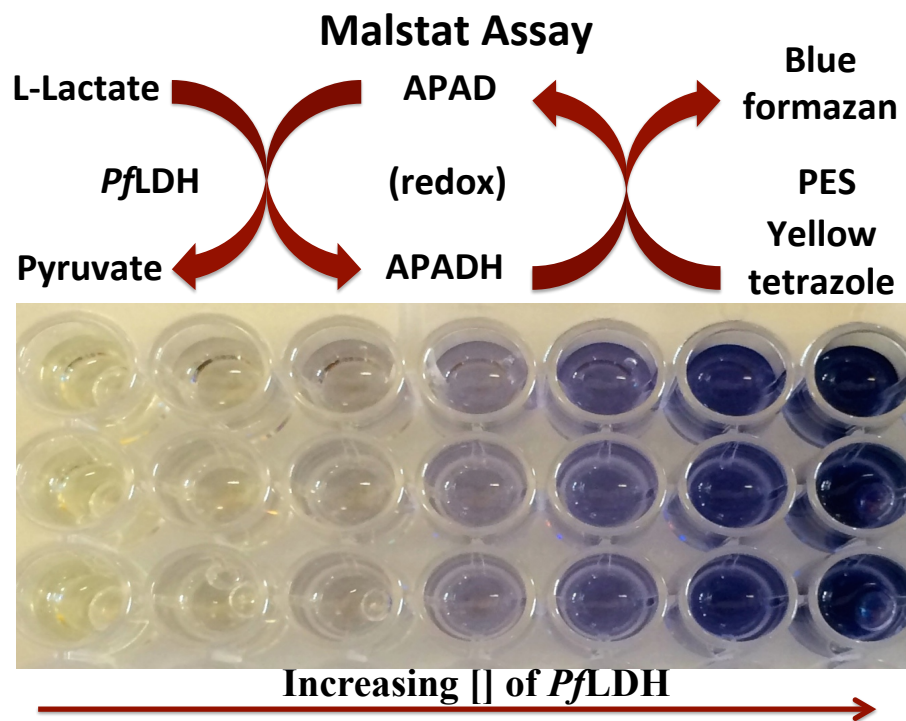


Figure 40. Malstat assay exhibits a colorimetric response as a function of increasing concentrations of *Pf*LDH. *Pf*LDH converts L-lactate to pyruvate in the presence of the cofactor APAD. APAD is then reduced to APADH, which catalyzes the formation of a yellow tetrazole to a blue formazan dye in the presence of phenylethyl sulfate (PES).

### *Catch-and-Release of PflLDH with Co(II)NTA Dynabeads*

Between 0-100 nM *Pfl*LDH, the His-tagged antibody appended to the magnetic Dynabeads captures the biomarker out of whole blood and subsequently elutes the antibody-*Pfl*LDH complex using imidazole. This solution is then deposited onto a 96-well plate to probe for Malstat assay activity. As a negative control, Co(II)NTA beads containing no His-tagged antibody are also titrated against the *Pfl*LDH in lysed whole blood (Figure 41). *Pfl*LDH does not bind specifically to untagged Co(II)NTA magnetic Dynabeads in lysed blood, nor do the beads carry over contaminants that yield false positives in the assay. The incorporation of a Hexa-His tag not only maintains the integrity of the paratope region of the antibody, but the enzymatic active site is also uncompromised. Although the limit of detection (14 nM) is outside the clinically relevant range of detection (160 pM for asymptomatic patients), concentrating the biomarker can increase the limit of detection by an order of magnitude. In addition, the protein recovery is approximately 40% in whole blood, which can also be increased by optimizing the *Pfl*LDH incubation time and the bead concentration to the antibody. Nonetheless, these initial catch-and-release experiments from a whole blood matrix demonstrate the potential to enhance future RDTs and show utility in creating His-tagged antibodies specific for a wide variety of antigens. Finally, the 15-minute timeframe required to capture and release the LDH biomarker is faster than the timeframe allotted by our lab's current extraction technology and shows utility in enhancing RDTs for a various diseases.

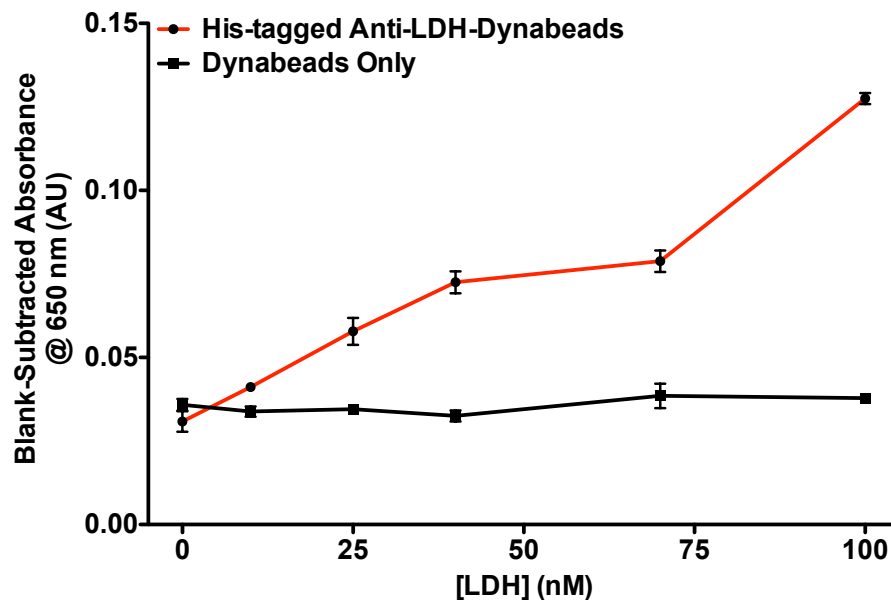


Figure 41. Titration of *Pf*LDH upon capture-and-release assay in lysed whole blood.

### Outlook for POC Diagnostics and Rapid Sensing

The development of novel diagnostic devices and therapeutic strategies do not emerge from a single publication or grant proposal. Often times, years of interdisciplinary science and collaborative efforts bring forth various perspectives, strategies, and techniques in order to create a polished platform device. However, innovative technologies are still necessitated as resistant parasitic strains thwart drug therapies and protein biomarkers begin to undergo genetic variations, limiting the efficacy of well-investigated drugs and molecular recognition elements, respectively. With a limited availability of resources in the developing world, the task toward developing simple, innovative strategies grows increasingly difficult. For a disease such as malaria that has thrived since the earliest recordings of mankind thousands of years ago, we still have not been able to eradicate it. Even with advanced techniques and instrumentation available in western society, they remain impractical for utilization in the developing world.

With the lack of affordable healthcare and resources in the developing world, materials and reagents must be on the orders of pennies. When one considers gold as a material, it is often thought of in an ostentatious manner, carrying expensive weight. On the contrary, gold costs approximately \$40 USD/gram on the international market. Considering proteins, enzymes, and even small molecules fetch for hundreds of dollars from chemical vendors, gold persists when the assay operates at the nanoscale, requiring only femtomoles of material. Gold also endures as a robust material, capable of enduring the extreme climates encountered in sub-Saharan Africa, Asia, and South America. Gold may not be the miracle material employed globally for the progression of public health, but similar materials are required for platform sensor and diagnostic development.

Nonetheless, innovative technologies and multiple perspectives are essential to constantly attack diagnosis and sensing issues from various angles. The greatest example I can offer for why innovative technologies are necessitated is the development and application of the pesticide, DDT. After WWII, this pesticide used to be considered the ultimate cure for malaria, by eliminating parasitic mosquitoes entirely (142). Initially, many first-world countries like the US participated in WHO-sponsored programs to spread nearly every square foot of their landscape with DDT during the 1950's and 1960's. The exorbitant costs and efforts provided by these programs essentially eradicated the disease in first-world regions. However, in regions where government and funds were not so ubiquitous like in the US, DDT coverage was sparser and less frequent, eliminating a high percentage of mosquitoes initially, only to see them return and thrive later. Once these mosquitoes began to develop resistance, people living in the developing world lost faith in the miracle pesticide, and DDT application became less and less



frequent. As a result, the malarial statistics in the developing world pre-WWII were just as severe as post-WWII.

The terrible consequence of DDT did not just pertain to undesirable human and ecological side effects, but during the 50's and 60's when DDT was widely applied, malarial funding ceased and research came to a standstill. Decades had already elapsed before government agencies and researchers were convinced that DDT was not the miracle chemical as originally advertised. Although this is an extreme case, the dystopian effects are exemplified when “eggs are put in one basket,” especially on a global scale. Research in science has given me the opportunity to understand that there are multiple solutions to each problem, and fundamental platforms for chemical sensing, disease diagnosis, and probe development pave the way for the next generation of techniques. It took years, numerous publications, and a large interdisciplinary team to optimize our lab's self-contained extraction platform for biomarker detection, and subsequently the wheels are beginning to turn for manufacturing purposes. All of those man-hours our lab has spent may prove to be futile for disease diagnosis in the long run, but the technology still offers one of many solutions to persistent problems. DDT raises an interesting argument because a single solution was offered for a global issue. Once the first-world countries could fund and eradicate the disease, it was too late for the developing world to combat malaria with a lack of available funding and resources. As gold materials begin to emerge in commercial applications, these fundamental platforms must be amenable to the developing world, not just for their social and economic development, but also to more effectively streamline our own healthcare, biomedical and governmental regulations. I have no doubt that research and innovation exploiting gold's unique properties will

continue to provide building blocks for biomedical purposes not just in the developing world, but in western culture as well.

## REFERENCES

1. Jani, I.V., Peter, T.F. (2013). How point-of-care testing can drive innovation in global health. *N Eng J Med*, **368**, 2319-2324.
2. Peeling, R.W., Holmes, K.K., Mabey, D., Ronald, A. (2006). Rapid tests for sexually transmitted infections (STIs): the way forward. *Sex Transm Infect*, **82**, v1-6.
3. Martinez, A.W., Phillips, S.T., Butte, M.J., Whitesides, G.M. (2007). Patterned paper as a platform for inexpensive, low-volume, portable bioassays. *Angew Chem Int Ed*, **46**, 1318-1320.
4. Martinez, A.W., Phillips, S.T., Whitesides, G.M. (2008). Three-dimensional microfluidic devices fabricated in layered paper and tape. *Proc Nat Acad Sci USA*, **105**, 19606-19611.
5. Martinez, A.W., Phillips, S.T., Carrilho, E., Thomas, III, S.W., Sindi, H. Whitesides, G.M. (2008). Simple telemedicine for developing regions: camera phones and paper-based microfluidic devices for real-time, off-site diagnosis. *Anal Chem*, **80**, 3699-3707.
6. Martinez, A.W., Phillips, S.T., Wiley, B.J., Gupta, M., Whitesides, G.M. (2008). FLASH: A rapid method for prototyping paper-based microfluidic devices. *Lab Chip*, **8**, 2146-2150.
7. Carrilho, E., Martinez, A.W., Whitesides, G.M. (2009). Understanding wax printing: a simple micropatterning process for paper-based microfluidics. *Anal Chem*, **81**, 7091-7095.
8. Malhotra, B.D., Singhal, R., Chaubey, A., Sharma, S.K., Kumar, A. (2005). Recent trends in biosensors. *Curr Appl Phys*, **5**, 92-97.
9. Merchant, B. (1998). Gold, the noble metal and the paradoxes of its toxicology. *Biologicals*, **28**, 49-59.
10. Eustis, S., El-Sayed, M.A. (2006). Why gold nanoparticles are more precious than pretty gold: noble metal surface plasmon resonance and its enhancement of the radiative and nonradiative properties of nanocrystals of different shapes. *Chem Soc Rev*, **35**, 209-217.
11. Jain, P.K., Huang, X., El-Sayed, I.H., El-Sayed, M.A. (2007). Review of some interesting surface plasmon resonance-enhanced properties of noble metal nanoparticles and their applications to biosystems. *Plasmonics*, **2**, 107-118.

12. Hammer, B., Norskov, J.K. (1995). Why gold is the noblest of all the metals. *Nature*, **376**, 238-240.
13. Kreibig, U., Genzel, L. (1985). Optical absorption of small metallic particles. *Surf Sci*, **156**, 678-700.
14. Quinten, M. Kreibig, U. (1986). Optical properties of aggregates of small metal particles. *Surf Sci*, **172**, 557-577.
15. Prodan, E., Nordlander, P. (2004). Plasmon hybridization in spherical nanoparticles. *J Chem Phys*, **120**, 5444-5454.
16. Nath, S., Ghosh, S.K., Kundu, S., Praharaj, S., Panigrahi, S., Pal, T. (2006). Is gold really softer than silver? HSAB principle revisited. *J Nanopart Res*, **8**, 11-116.
17. Bain, C.D., Troughton, E.B., Tao, Y.T., Evall, J., Whitesides, G.M., Nuzzo, R.G. (1988). Formation of monolayer films by the spontaneous assembly of organic thiols from solution onto gold. *J Am Chem Soc*, **111**, 321-335.
18. Nuzzo, R.G., Allara, D.L. (1983). Adsorption of bifunctional organic disulfides on gold surfaces. *J Am Chem Soc*, **105**, 4481-4483.
19. Love, J.C., Estroff, L.A., Kriebel, J.K., Nuzzo, R.G., Whitesides, G.M. (2005). Self-assembled monolayers of thiolates on metals as a form of nanotechnology. *Chem Rev*, **105**, 1105-1169.
20. Moore, D.S. (2008). Instrumentation for trace detection of high explosives. *Rev Sci Instrum*, **75**, 2499-2512.
21. Thomas, III, S.W., Joly, G.D., Swager, T.M. (2007). Chemical sensors based on amplifying fluorescent conjugated polymers. *Chem Rev*, **107**, 1339-1386.
22. Singh, S., Singh, M. (2003). Explosive detection systems (EDS) for aviation security. *Sig Proc*, **83**, 31-55.
23. Hundal, L.S., Singh, J., Bier, E.L., Shea, P.J., Comfort, S.D., Powers, W.L. (1997). Removal of TNT and RDX from water and soil using iron metal. *Environ Pollut*, **97**, 55-64.
24. Kaplan, D.L., Kaplan, A.M. (1982). 2,4,6-trinitrotoluene-surfactant complexes: decomposition, mutagenicity, and soil leaching studies. *Environ Sci Technol*, **16**, 566-571.

25. Talmage, S.S., Opresko, D.M., Maxwell, C.J., Welsh, C.J., Cretella, F.M., Reno, P.H., Daniel, F.B. (1999). Nitroaromatic munition compounds: environmental effects and screening values. *Rev Environ Contam Toxicol*, **161**, 1-156.
26. Van Dillewijn, P., Couselo, J.L., Corredoira, E., Delgado, A., Wittich, R.M., Ballester, A., Ramos, J.L. (2008). Bioremediation of 2,4,6-trinitrotoluene by bacterial nitroreductase expressing transgenic aspen. *Environ Sci Technol*, **42**, 7405-7410.
27. Won, W.D., DiSalvo, L.H., Ng, J. (1976). Toxicity and mutagenicity of 2,4,6-trinitrotoluene and its microbial metabolites. *Appl Environ Microbiol*, **31**, 576-580.
28. EPA. (2011). Emerging Contaminants – 2,4,6-Trinitrotoluene.
29. U.S. Department of Health and Human Services. (1995). Toxicological Profile for 2,4,6-trinitrotoluene.
30. Esteve-Nunez, A., Ramos, J.L. (1998). Metabolism of 2,4,6-trinitrotoluene by *Pseudomonas* sp. JLR11. *Environ Sci Technol*, **32**, 3802-3808.
31. Haidour, A., Ramos, J.L. (1996). Identification of products resulting from the biological reduction of 2,4,6-trinitrotoluene, 2,4-dinitrotoluene, and 2,6-dinitrotoluene by *Pseudomonas* sp. *Environ Sci Technol*, **30**, 2365-2370.
32. Senesac, L., Thundat, T.G. (2008). Nanosensors for trace explosive detection. *Mater Today*, **11**, 28-36.
33. Fetterolf, D.D., Clark, T.D. (1993). Detection of trace explosive evidence by ion mobility spectrometry. *J Forens Sci*, **38**, 28-39.
34. Matz, L.M., Tornatore, P.S., Hill, H.H. (2001). Evaluation of suspected interferences for TNT detection by ion mobility spectrometry. *Talanta*, **54**, 171-179.
35. Habib, M.K. (2007). Controlled biological and biomimetic systems for landmine detection. *Biosens Bioelectron*, **23**, 1-18.
36. Heller, D.A., Pratt, G.W., Zhang, J., Nair, N., Hansborough, A.J., Boghossian, A.A., Reuel, N.F., Barone, P.W., Strano, M.S. (2011). Peptide secondary structure modulates single-walled carbon nanotube fluorescence as a chaperone sensor for nitroaromatics. *Proc Nat Acad Sci USA*, **108**, 8544-8549.
37. French, C.E., Nicklin, S., Bruce, N.C. (1998). Aerobic degradation of 2,4,6-trinitrotoluene by *Enterobacter cloacae* PB2 and by pentaerythritol tetranitrate reductase. *Appl Environ Microbiol*, **64**, 2864-2868.

38. Khan, H., Barna, T., Harris, R.J., Bruce, N.C. Barsukov, I., Munro, A.W., Moody, P.C.E., Scrutton, N.S. (2004). Atomic resolution structures and solution behavior of enzyme-substrate complexes of *Enterobacter cloacae* PB2 pentaerythritol tetranitrate reductase. *J Biol Chem*, **279**, 30563-30572.
39. Jaworski, J.W., Raorane, D., Huh, J.H., Majumdar, A., Lee, S.W. (2008). Evolutionary screening of biomimetic coatings for selective detection of explosives. *Langmuir*, **24**, 4938-4943.
40. Goldman, E.R., Pazirandeh, M.P., Charles, P.T., Balighian, E.D., Anderson, G.P. (2002). Selection of phage displayed peptides for the detection of 2,4,6-trinitrotoluene in seawater. *Anal Chim Acta*, **457**, 13-19.
41. Pesenti, M.E., Spinelli, S., Bezirard, V., Briand, L., Pernollet, J.C., Tegoni, M., Cambillau, C. (2008). Crystal structure of a pheromone binding protein from *Apis mellifera* in complex with the queen mandibular pheromone. *J Mol Biol*, **380**, 158.
42. Kuang, Z., Kim, S.N., Crookes-Goodson, W.J., Farmer, B.L., Naik, R.R. (2010). Biomimetic chemosensor: designing peptide recognition elements for surface functionalization of carbon nanotube field effect transistors. *ACS Nano*, **4**, 452-458.
43. Kim, T.H., Lee, B.Y., Jaworski, J., Yokoyama, K., Chung, W.J., Wang, E., Hong, S., Majumdar, A., Lee, S.W. (2011). Selective and sensitive TNT Sensors using biomimetic polydiacetylene-coated CNT-FETs. *ACS Nano*, **5**, 2824-2830.
44. Jaworski, J., Yokoyama, K., Zueger, C., Chung, W.J., Lee, S.W., Majumdar, A. (2011). Polydiacetylene incorporated with peptide receptors for the detection of trinitrotoluene explosives. *Langmuir*, **27**, 3180-3187.
45. Janshoff, A., Galla, H.J., Steinem, C. (2000). Piezoelectric mass-sensing devices as biosensors-an alternative to optical biosensors? *Angew Chem Int Ed*, **39**, 4004-4032.
46. Gerdon, A.E., Wright, D.W., Cliffel, D.E. (2005). Quartz crystal microbalance detection of glutathione-protected nanoclusters using antibody recognition. *Anal Chem*, **77**, 304-310.
47. Gerdon, A.E., Wright, D.W., Cliffel, D.E. (2005). Hemagglutinin linear epitope presentation on monolayer-protected clusters elicits strong antibody binding. *Biomacromolecules*, **6**, 3419-3424.
48. Sauerbrey, G. (1959). The use of quartz oscillators for weighing thin layers and for microweighing. *Z Phys*, **155**, 206-222.

49. Glassford, A.P.M. (1978). Response of a quartz crystal microbalance to a liquid deposit. *J Vac Sci Technol*, **15**, 1836-1843.
50. Kanazawa, K.K., Gordon, J. (1985). Frequency of a quartz microbalance in contact with liquid. *Anal Chem*, **57**, 1770-1771.
51. Kanazawa, K.K. Gordon, J.G. (1985). The oscillation frequency of a quartz resonator in contact with liquid. *Anal Chim Acta*, **175**, 99-105.
52. Bard, A.J., Faulkner, L.R. *Electrochemical methods: fundamentals and applications, 2nd Ed.* John Wiley & Sons, Inc. (2001).
53. Gulka, C.P, Gizzie, E.A., Cliffler, D.E. Wright, D.W. (2014). Electrochemical detection of 2,4,6-trinitrotoluene at colloidal gold nanoparticle film assemblies. *Submitted*.
54. Li, G., Miao, P. *Electrochemical analysis of proteins and cells*. Springer. (2013).
55. Kwon, S.J., Yang, H., Jo, K., Kwak, J. (2008). An electrochemical immunosensor using p-aminophenol redox cycling by NADH on a self-assembled monolayer and ferrocene-modified Au electrodes. *Analyst*, **133**, 1599-1604.
56. Song, S., Clark, R.A., Bowden, E.F., Tarlov, M.J. (1993). Characterization of cytochrome c/alkanethiolate structures prepared by self-assembly on gold. *J Phys Chem*, **97**, 6564-6572.
57. Nakano, K., Yoshitake, T., Yamashita, Y., Bowden, E.F. (2007). Cytochrome c self-assembly on alkanethiol monolayer electrodes as characterized by AFM, IR, QCM, and direct electrochemistry. *Langmuir*, **23**, 6270-6275.
58. Davis, K. L., Drews, B.J., Yue, H., Waldeck, D.H., Knorr, K., Clark, R.A. (2008). Electron-transfer kinetics of covalently attached cytochrome c/SAM/Au electrode assemblies. *J Phys Chem C*, **112**, 6571-6576.
59. Avila, A., Gregory, B.W., Niki, K., Cotton, T.M. (2000). An electrochemical approach to investigate gated electron transfer using a physiological model system: Cytochrome c immobilized on carboxylic acid-terminated alkanethiol self-assembled monolayers on gold electrodes. *J Phys Chem B*, **104**, 2759-2766.
60. Niki, K., Hardy, W.R., Hill, M.G., Li, H., Sprinkle, J.R., Margoliash, E., Fujita, K., Tanimura, R., Nakamura, N., Ohno, H., Richards, J.H., Gray, H.B. (2003). Coupling to Lysine-13 promotes electron tunneling through carboxylate-terminated alkanethiol self-assembled monolayers to cytochrome c. *J Phys Chem B*, **107**, 9947-9949.

61. Flemming, B.D., Proporski, S., Bond, A.M., Martin, L.L. (2008). Electrochemical quartz crystal microbalance study of azurin adsorption onto an alkanethiol self-assembled monolayer on gold. *Langmuir*, **24**, 323-327.
62. Chi, Q., Zhang, J., Andersen, J.E.T., Ulstrup, J. (2001). Ordered assembly and controlled electron transfer of the blue copper protein azurin at gold (111) single-crystal substrates. *J Phys Chem B*, **105**, 4669-4679.
63. Fujita, K., Nakamura, N., Ohno, H., Leigh, B.S., Niki, K., Gray, H.B., Richards, J.H. (2004). Mimicking protein-protein electron transfer: voltammetry of *Pseudomonas aeruginosa* azurin and the *Thimus thermophilus* Cu-A domain at omega-derivatized self assembled-monolayer gold electrodes. *J Am Chem Soc*, **126**, 13954-13961.
64. Yokoyama, K., Leigh, B.S., Sheng, Y., Niki, K., Nakamura, N., Ohno, H., Winkler, J.R., Gray, H.B., Richards, J.H. (2008). Electron tunneling through *Pseudomonas aeruginosa* azurins on SAM gold electrodes. *Inorg Chim Acta*, **361**, 1095-1099.
65. Loftus, A.F., Reighard, K.P., Kapourales, S.A., Leopold, M.C. (2008). Monolayer-protected nanoparticle film assemblies for controlling interfacial and adsorption properties in protein monolayer electrochemistry. *J Am Chem Soc*, **130**, 1649-1661.
66. Vargo, M.V., Gulka, C.P., Gerig, J.K., Manieri, C.M., Dattelbaum, J.D., Marks, C.B., Lawrence, N.T., Trawick, M.L., Leopold, M.C. (2010). Distance dependence of electron transfer kinetics for azurin protein adsorbed to monolayer protected nanoparticle film assemblies. *Langmuir*, **26**, 560-569.
67. Schmidt, A.R., Nguyen, N.D.T., Leopold, M.C. (2013). Nanoparticle film assemblies as platforms for electrochemical biosensing-factors affecting the amperometric signal enhancement of hydrogen peroxide. *Langmuir*, **29**, 4574-4583.
68. Chua, C.K., Pumera, M., Rulišek, L. (2012). Reduction pathways of 2,4,6-trinitrotoluene: an electrochemical and theoretical study. *J Phys Chem C*, **116**, 4243-4251.
69. de Sanoit, J., Vanhove, E., Mailley, P., Bergonzoa, P. (2009). Electrochemical diamond sensors for TNT detection in water. *Electrochimica Acta*, **54**, 5688-5693.
70. Yu, Y., Cao, Q., Zhou, M., Cui, H. (2013). A novel homogeneous label-free aptasensor for 2,4,6-trinitrotoluene detection based on an assembly strategy of electrochemiluminescent graphene oxide with gold nanoparticles and aptamer. *Biosens Bioelectron*, **43**, 137-142.



71. Goh, M.S., Pumera, M. (2011). Graphene-based electrochemical sensor for detection of 2,4,6-trinitrotoluene (TNT) in seawater: the comparison of single-, few-, and multilayer graphene nanoribbons and graphite microparticles. *Anal Bioanal Chem*, **399**, 127-131.
72. Ma, H., Yao, L., Li, P., Ablikim, O., Cheng, Y., Zhang, M. (2014). Highly sensitive and selective fluorometric/electrochemical dual-channel sensors for TNT and DNT explosives. *Chem Eur J*, **20**, 11655-11658.
73. Finklea, H.O. *Electroanalytical Chemistry*. Marcel Dekker. (1996).
74. Wang, H., Pilon, L. (2011). Accurate simulations of electric double layer capacitance of ultramicroelectrodes. *J Phys Chem C*, **115**, 16711-16719.
75. Lin, C., Tao, K., Hua, D., Ma, Z., Zhou, S. (2013). Size effect of gold nanoparticles in catalytic reduction of p-nitrophenol with NaBH<sub>4</sub>. *Molecules*, **18**, 12609-12620.
76. Zhou, X., Xu, W., Liu, G., Panda, D., Chen, P. (2010). Size-dependent catalytic activity and dynamics of gold nanoparticles at the single-molecule level. *J Am Chem Soc*, **132**, 138-146.
77. Choi, Y., Choi, M.-J., Cha, S.-Y., Kim, Y.S., Cho, S., Park, Y. (2014). Catechin-capped gold nanoparticles: green synthesis, characterization, and catalytic activity toward 4-nitrophenol reduction. *Nanoscale Res Lett*, **9**, 103-110.
78. Brülle, T., Ju, W., Niedermayr, P., Denisenko, A., Paschos, O., Schneider, O., Stimming, U. (2011). Size-dependent electrocatalytic activity of gold nanoparticles on HOPG and highly boron-doped diamond surfaces. *Molecules*, **16**, 10059-10077.
79. Cizek, K., Prior, C., Thammakhet, C., Galik, M., Linker, Tsui, R., Cagan, A., Wake, J., La Belle, J., Wang, J. (2010). Integrated explosive preconcentrator and electrochemical detection system for 2,4,6-trinitrotoluene (TNT) vapor. *Anal Chim Acta*, **661**, 117-121.
80. Swartz, J.D., Gulka, C.P., Haselton, F.R., Wright, D.W. (2011). Development of histidine-targeted spectrophotometric sensor using Ni(II)NTA-functionalized Au and Ag nanoparticles. *Langmuir*, **27**, 15330-15339.
81. Gulka, C.P., Swartz, J.D., Wright, D.W. (2014). Ni(II)NTA AuNPs as a low-resource malarial diagnostic platform for the rapid colorimetric detection of *Plasmodium falciparum* Histidine-Rich Protein-2. *Submitted*.
82. Murray, C.K., Gasser, Jr., R.A., Magill, A.J., Miller, S.A. (2008). Update on rapid diagnostic testing for malaria. *Clin Microbiol Rev*, **21**, 97-110.

83. WHO. World Malaria Report, (2011).
84. Wurtz, N., Fall, B., Bui, K., Pascual, A., Fall, M., Camara, C., Diatta, B., Fall, K.B., Mbaye, P.S., Dieme, Y., Bercion, R., Wade, B., Briolant, S., Pradines, B. (2013). *Pfhrp2* and *Pfhrp3* polymorphisms in *Plasmodium falciparum* isolates from Dakar, Senegal: impact on rapid malaria diagnostic tests. *Malar J*, **12**, 34-41.
85. Kumar, N., Singh, J.P.N., Pande, V., Mishra, N., Srivastava, B., Kapoor, R., Valecha, N., Anvikar, A.R. (2012). Genetic variation in histidine rich proteins among indian *Plasmodium falciparum* population: possible cause of variable sensitivity of malaria rapid diagnostic tests. *Malar J*, **11**, 298-304.
86. Chiodini, P.L., Bowers, K., Jorgensen, P., Barnwell, J.W., Grady, K.K., Luchavez, J., Moody, A. H., Cenizal, A., Bell, D. (2007). The heat stability of *Plasmodium* lactate dehydrogenase-based and histidine-rich protein 2-based malaria rapid diagnostic tests. *Trans R Soc Trop Med Hyg*, **101**, 331-337.
87. Panton, L.J., Mcphie, P., Maloy, W.L., Wellems, T.E., Taylor, D.W., Howard, R.J. (1989). Purification and partial characterization of an unusual protein of *Plasmodium falciparum*: histidine-rich protein II. *Mol Biochem Parasitol*, **35**, 149-160.
88. Terpe, K. (2003). Overview of tag protein fusions: from molecular and biochemical fundamentals to commercial systems. *Appl Microbiol Technol*, **60**, 523-533.
89. Mori, S., Takahashi, H.K., Yamaoka, K., Okamoto, M., Nishibori, M. (2003). High affinity binding of serum histidine-rich glycoprotein to nickel-nitrilotriacetic acid: the application to microquantification. *Life Sci*, **73**, 93-102.
90. Ghimire, P., Samantaray, J.C., Mirdha, B.R., Patra, A.K., Panda, A.K., (2003). Purification and partial characterization of PfHRP-II protein of *Plasmodium falciparum*. *Southeast Asian J Trop Med Public Health*, **34**, 739-743.
91. Knecht, S., Ricklin, D., Eberle, A.N., Ernst, B. (2009). Oligohis-tags: mechanisms of binding to Ni<sup>2+</sup>-NTA surfaces. *J Mol Recognit*, **22**, 270-279.
92. Elghanian, R., Storhoff, J.J., Mucic, R.C., Letsinger, R.L., Mirkin, C.A. (1997). Selective colorimetric detection of polynucleotides based on the distance-dependent optical properties of gold nanoparticles. *Science*, **277**, 1078-1081.
93. Storhoff, J.J., Elghanian, R., Mucic, R.C., Mirkin, C.A., Letsinger, R.L. (1998). One-pot colorimetric differentiation of polynucleotides with single base imperfections using gold nanoparticle probes. *J Am Chem Soc*, **120**, 1959-1964.

94. Xia, F., Zuo, X., Yang, R., Xiao, Y., Kang, D., Vallée-Bélisle, A., Gong, X., Yuen, J.D., Hsu, B.B.Y., Heeger, A.J., Plaxco, K.W. (2010). Colorimetric detection of DNA, small molecules, proteins, and ions using unmodified gold nanoparticles and conjugated polyelectrolytes. *Proc Nat Acad Sci USA*, **107**, 10837-10841.
95. Liu, J., Lu, Y. (2003). A colorimetric lead biosensor using DNAzyme-directed assembly of gold nanoparticles. *J Am Chem Soc*, **125**, 6642-6643.
96. Boisselier, E., Astruc, D. (2009). Gold nanoparticles in nanomedicine: preparations, imaging, diagnostics, therapies and toxicity. *Chem Soc Rev*, **38**, 1759-1782.
97. Shen, L., Hagen, J.A., Papautsky, I. (2012). Point-of-care colorimetric detection with a smartphone. *Lab Chip*, **12**, 4240-4243.
98. Oncescu, V., O'Dell, D., Erickson, D. (2013). Smartphone based health accessory for colorimetric detection of biomarkers in sweat and saliva. *Lab Chip*, **13**, 3232-3238.
99. Lee, S., Oncescu, V., Mancuso, M., Mehtac, S., Erickson, D. (2014). A smartphone platform for the quantification of vitamin D levels. *Lab Chip*, **14**, 1437-1442.
100. Oh, J.W., Chung, W.J., Heo, K., Jin, H.E., Lee, B.Y., Wang, E., Zueger, C., Wong, W., Meyer, J., Kim, C., Lee, S.Y., Kim, W.G., Zemla, M., Auer, M., Hexemer, A., Lee, S.W. (2014). Biomimetic virus-based colourimetric sensors. *Nat Comm*, **5**, 3043-3050.
101. Prime, K.L., Whitesides, G.M. (1991). Self-assembled organic monolayers: model systems for studying adsorption of proteins at surfaces. *Science*, **24**, 1164-1167.
102. Prime, K.L., Whitesides, G.M. (1993). Adsorption of proteins onto surfaces containing end-attached oligo(ethylene oxide): a model system using self-assembled monolayers. *J Am Chem Soc*, **115**, 10714-10721.
103. Bandyopadhyay, K., Shu, L., Liu, H., Echegoyen, L. (2000). Selective K<sup>+</sup> recognition at the interface during self-assembly of a bis-podand thiol on a gold surface. *Langmuir*, **16**, 2706-2714.
104. Banerjee, I., Pangule, R.C., Kane, R.S. (2011). Antifouling coatings: recent developments in the design of surfaces that prevent fouling by proteins, bacteria, and marine organisms. *Adv Mat*, **23**, 690-718.
105. Benedetti, C.E., Kobarg, J., Pertinhez, T.A., Gatti, R.M., de Souza, O.N., Spisni, A., Meneghini, R. (2003). *Plasmodium falciparum* histidine-rich protein II binds to actin, phosphatidylinositol 4,5-bisphosphate and erythrocyte ghosts in a pH-

- dependent manner and undergoes coil-to-helix transitions in anionic micelles. *Mol Biochem Parasitol*, **128**, 157-166.
106. Schneider, E.L., Marletta, M.A. (2005). Heme binding to the histidine-rich protein II from *Plasmodium falciparum*. *Biochemistry*, **44**, 979-986.
107. Hinterworth, H., Kappel, S., Waitz, T., Prohaska, T., Lindner, W., Lammerhofer, M. (2013). Quantifying thiol ligand density of self-assembled monolayers on gold nanoparticles by inductively coupled plasma-mass spectrometry. *ACS Nano*, **7**, 1129-1136.
108. Davis, K.M., Swartz, J.D., Haselton, F.R., Wright, D.W. (2012). Low-resource method for extracting the malarial biomarker histidine-rich protein II to enhance diagnostic test performance. *Anal Chem*, **84**, 6136-6142.
109. Aslan, K., Malyn, S.N., Geddes, C.D. (2007). Metal-enhanced fluorescence from gold surfaces: angular dependent emission. *J Fluoresc*, **17**, 7-13.
110. Sellers, H., Ulman, A., Shnidman, Y., Eilers, J.E. (1993). Structure and binding of alkanethiolates on gold and silver surfaces: implications for self-assembled monolayers. *J Am Chem Soc*, **115**, 9389-9401.
111. Gulka, C.P., Swartz, J.D., Trantum, J.R., Davis, K.M., Peak, C.M., Denton, A.J., Haselton, F.R., Wright, D.W. (2014). Coffee rings as low-resource diagnostics: detection of the malaria biomarker *Plasmodium falciparum* histidine-rich protein-II using a surface-coupled ring of Ni(II)NTA gold-plated polystyrene particles. *ACS Appl Mater Interfaces*, **6**, 6257-6263.
112. Deegan, R.D., Bakajin, O., Dupont, T.F., Huber, G., Nagel, S.R., Witten, T.A. (1997). Capillary flow as the cause of ring stains from dried liquid drops. *Nature*, **389**, 827-829.
113. Deegan, R.D. (2000). Pattern formation in drying drops. *Phys Rev E*, **61**, 475-485.
114. Deegan, R.D., Bakajin, O., Dupont, T.F., Huber, G., Nagel, S.R., Witten, T.A. (2000). Contact line deposits in an evaporating drop. *Phys Rev E*, **62**, 756-765.
115. Tarasevich, Y.Y., Pravoslavnova, D.M. (2007). Segregation in desiccated sessile drops of biological fluids. *Eur Phys J E*, **22**, 311-314.
116. Tarasevich, Y.Y., Pravoslavnova, D.M. (2007). Drying of a multicomponent solution drop on a solid substrate: qualitative analysis. *Tech Phys*, **52**, 159-163.
117. Larson, R.G., Lopez, M.A., Lim, D.W., Lahann, J. (2010). Complex protein patterns in drying droplets. *MRS Proc*, **1273**.

118. Brutin, D., Sobac, B., Loquet, B., Sampol, J. (2011). Pattern formation in drying drops of blood. *J Fluid Mech*, 2011, **667**, 85-95.
119. Wong, T.S.; Chen, T.H.; Shen, X.Y.; Ho, C.M. (2011). Nanochromatography driven by the coffee ring effect. *Anal Chem*, **83**, 1871-1873.
120. Wen, J.T., Ho, C.M., Lillehoj, P.B. (2013). Coffee ring aptasensor for rapid protein detection. *Langmuir*, **29**, 8440-8446.
121. Trantum, J.R., Baglia, M.L., Eagleton, Z.E., Mernaugh, R.L., Haselton, F.R. (2014). Biosensor design based on marangoni flow in an evaporating drop. *Lab Chip*, **14**, 315-324.
122. Trantum, J.R., Wright, D.W., Haselton, F.R. (2012). Biomarker-mediated disruption of coffee-ring formation as a low resource diagnostic indicator. *Langmuir*, **28**, 2187-2193.
123. Westcott, S.L., Oldenburg, S.J., Lee, T.R., Halas, N.J. (1998). Formation and adsorption of clusters of gold nanoparticles onto functionalized silica nanoparticle surfaces. *Langmuir*, **14**, 5396-5401.
124. Oldenburg, S.J., Averitt, R.D., Westcott, S.L.; Halas, N.J. (1998). Nanoengineering of optical resonances. *Chem Phys Lett*, **288**, 243-247.
125. Pham, T., Jackson, J.B., Halas, N.J., Lee, T.R. (2002). Preparation and characterization of gold nanoshells coated with self-assembled monolayers. *Langmuir*, **18**, 4915-4920.
126. Shi, W., Sahoo, Y., Swihart, M.T., Prasad, P.N. (2005). Gold nanoshells on polystyrene cores for control of surface plasmon resonance. *Langmuir*, **21**, 1610-1617.
127. Piao, L., Park, S., Lee, H.B., Kim, K., Kim, J., Chung, T.D. (2010). Single gold microshell tailored to sensitive surface enhanced raman scattering probe. *Anal Chem*, **82**, 447-451.
128. Knecht, M.R., Wright, D.W. (2004). Dendrimer mediated formation of multicomponent nanospheres. *Chem Mater*, **16**, 4890-4895.
129. Perumareddi, J.R., Liehr, A.D., Adamson, A.W. (1963). Ligand field theory of transition metal cyanide complexes. Part I. The zero, one and two electron or hole configurations. *J Am Chem Soc*, **85**, 249-259.
130. Swartz, J.D. (2012). From diatoms to malaria: synthesis and application of functionalized micro- and nanomaterials. Ph.D. Dissertation, Vanderbilt University.

131. van den Meerakker, J.E.A.M. (1981). On the mechanism of electroless plating. II. One mechanism for different reductants. *J Appl Electrochem*, **11**, 395-400.
132. Dondorp, A.M., Desakorn, V., Pongtavornpinyo, W., Sahassananda, D., Silamut, K., Chotivanich, K., Newton, P.N., Pitisuttihum, P., Smithyman, A.M., White, N.J., Day, N.P.J. (2005). Estimation of the total parasite biomass in acute *falciparum* malaria from plasma PfHRP2. *PLoS Med*, **2**, e204.
133. Manning, L., Laman, M., Stanistic, D., Rosanas-Urgell, A., Bona, C., Teine, D., Siba, P., Mueller, I., Davis, T.M.E. (2011). Plasma *Plasmodium falciparum* histidine-rich protein-2 concentrations do not reflect severity of malaria in Papua New Guinean children. *Clin Infect Dis*, **52**, 440-446.
134. Rubach, M.P., Mukemba, J., Florence, S., John, B., Crookston, B., Lopansri, B.K., Yeo, T.W., Piera, K.A., Alder, S.C., Weinberg, J.B., Anstey, N.M., Granger, D.L., Mwaikambo, E.D. (2012). Plasma *Plasmodium falciparum* histidine-rich protein-2 concentrations are associated with malaria severity and mortality in tanzanian children. *PloS ONE*, **7**, e35985.
135. Vyawahare, S., Craig, K.M., Scherer, A. (2006). Patterning lines by capillary flows. *Nano Lett*, **6**, 271-276.
136. Still, T., Yunker, P.J., Yodh, A.G. (2012). Surfactant-induced marangoni eddies alter the coffee-rings of evaporating colloidal drops. *Langmuir*, **28**, 4984-4988.
137. Cui, L., Zhang, J., Zhang, X., Huang, L., Wang, Z., Li, Y., Gao, H., Zhu, S., Wang, T., Yang, B. (2012). Suppression of the coffee ring effect by hydrosoluble polymer additives. *ACS Appl Mater Interfaces*, **4**, 2775-2780.
138. Davis, K.M., Gibson, L.E., Wright, D.W. (2014). Simple sample processing enhances malaria rapid diagnostic test performance. *Analyst*, **139**, 3026-3031.
139. Makler, M.T., Piper, R.C., Milhous, W.K. (1998). Lactate dehydrogenase and the diagnosis of malaria. *Parasitol Today*, **14**, 376-377.
140. Makler, M.T., Ries, J.M., Williams, J.A., Bancroft, J.E., Piper, R.C., Gibbins, B.L., Hinrichs, D.J. (1993). Parasite lactate dehydrogenase as an assay for *Plasmodium falciparum* drug sensitivity. *Am J Trop Med Hyg*, **48**, 739-741.
141. Makler, M.T., Hinrichs, D.J. (1993). Measurement of the lactate dehydrogenase activity of *Plasmodium falciparum* as an assessment of parasitemia. *Am J Trop Med Hyg*, **48**, 205-210.
142. Shah, S. *The fever*. Sarah Crichton Books, Farrar, Straus, and Giroux. (2010).

## Appendix A

### Alternative Microbead Platform Technologies for Detection of the *P. falciparum* HRP-II Malarial Biomarker

#### *Single bead platform sandwich assays exploiting magnetic microparticles*

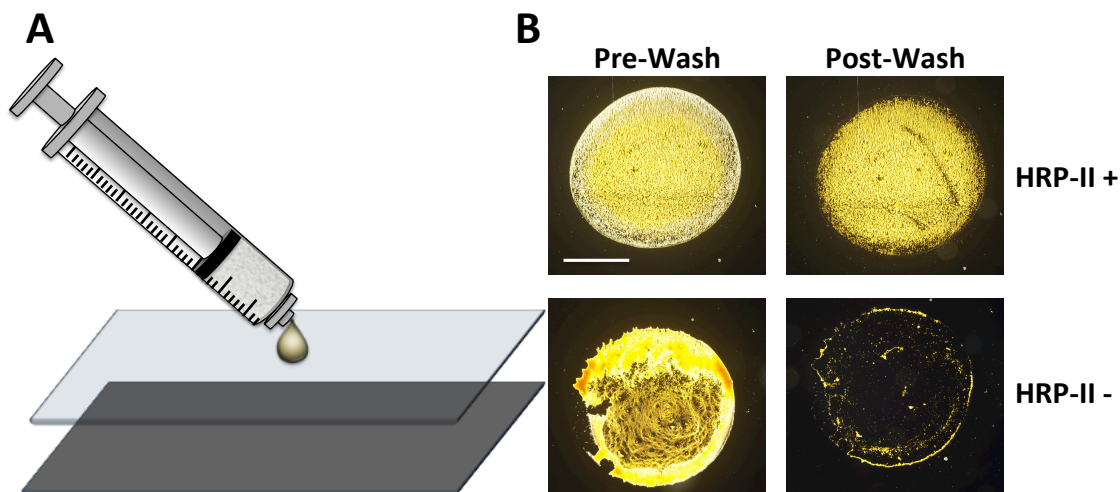
Although the coffee ring-inspired assay using Ni(II)NTA AuPSs addresses many of the shortcomings of low-resource diagnostics for the developing world, one of the inherent problems associated with this platform design is the lack of radial particle flow when a complex matrix is introduced into the sample. In the presence of a complex matrix with the current design of this technology, a pre-assay sample purification step must be performed so that the particles maintain their natural radial flow patterns. Often times, the incorporation of a purification step or a pre-concentration step prolongs the overall assay time, so that alternative platform technologies are sought.

Functionalized magnetic microparticles are an attractive alternative to polystyrene particles in the coffee ring assay because once a biomarker of interest is captured in a complex matrix, a well-positioned magnet underneath the substrate (functionalized glass in this design) can pull the suspended biomarker-particle conjugates towards the surface to sandwich the biomarker in between the substrate and the beads. It is also hypothesized that the stronger magnetic force pulling the biomarker-particle conjugates towards the glass substrate will adsorb the assay materials faster, requiring less time for the platform diagnostic. Mimicking an ELISA, the beads elicit the chromogenic signal instead of an enzyme linked to an antibody after a water wash. The following figures are proof-of-

concept experiments with Co(II)NTA-functionalized magnetic Dynabeads for rcHRP-II capture and detection.

The divalent metal, Co(II), when coordinated to NTA, has the weakest affinity to histidine in comparison to Ni(II)NTA, Zn(II)NTA, and Cu(II)NTA. However, Co(II)NTA demonstrates the highest specificity to histidine repeats, which would be especially useful in recognizing rcHRP-II when dissolved in a complex matrix. Supplemental Figures 1 and 2 are proof-of-concepts experiments showing that the biomarker can be sandwiched in-between the magnetic beads and the glass substrate. In the first experiment, the signal can be enhanced by increasing the duration of magnet exposure to the beads (Supplemental Figure 1). With this format, a thin refrigerator magnet is placed directly underneath the glass in order to attract the beads. Once the beads are reacted with a solution of HRP-II, the protein-particle conjugates are pipetted directly onto a Ni(II)NTA-functionalized glass slide and allowed to dry. Although the magnetic moment of the material is low, the beads need to be exposed to the magnet for approximately 60 minutes and subsequently washed for optimized signal. It is hypothesized that the refrigerator magnet has a weak effect on overall assay signal because a 60-minute drying time is the same time required for the ring assay described in Chapter V. Additionally, the dense Dynabead particles (2.5 g/mL) do not maintain the radial coffee ring flow patterns like their lighter polystyrene counterparts and settle to the middle of the drop during evaporation. The lack of a natural biomarker concentration due to the coffee ring phenomenon complicates this assay format because a longer time is required for the particle-biomarker conjugates to adsorb to the glass.

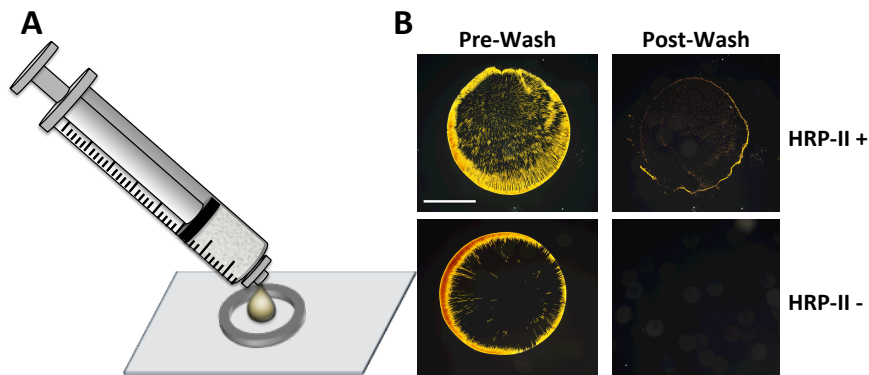




Supplemental Figure 1. Co(II)NTA Dynabead sandwich assays detecting rcHRP-II. (A) Schematic of the assay showing that after the Dynabeads (30X diluted from stock containing 0.005% v/v Tween 20 and 1% glycerol) are reacted with 1  $\mu$ M rcHRP-II for 30 seconds, the protein-particle conjugates are deposited (1  $\mu$ L) onto a Ni(II)NTA-functionalized glass slide. A thin refrigerator magnet is placed directly underneath the glass slide to magnetically attract the Dynabead-biomarker conjugates. After one hour, the slide is placed in a 50 mL conical tube filled with deionized water, and shaken for 10 seconds to wash away non-specific binding. (B) Images captured with a Nikon camera show that the particles are sandwiched to the glass in the presence of protein. “HRP-II+” denotes 1  $\mu$ M rcHRP-II while “HRP-II-” denotes 0 rcHRP-II. The white bar scales to 1 mm. (All data collected with Mark Baglia in the Haselton lab).

Successful POC diagnostics for the developing world using a microparticle platform will have to be carefully optimized for selective and sensitive detection of biomarkers. The assay described in Supplemental Figure 1 requires approximately one hour in order to generate results conveying positive or negative infection. However, the WHO recommends overall assay time not to exceed 15-30 minutes. Because the low-magnetic moment refrigerator magnet has a negligible effect on assay signal, it is hypothesized that a stronger magnet can ultimately increase signal-to-noise. Using a neodymium (Nd) ring magnet, which has one of the largest naturally occurring magnetic moments, assay noise can be reduced by decreasing the duration of exposure to the

magnet (20 min). Additionally, the ring design of the magnet can attract the protein-particle conjugates in a radial configuration, thus creating a biomarker concentration step (Supplemental Figure 2). After exposing the protein-particle conjugates to the magnet for 20 minutes, the slide is washed with water and the noise is significantly reduced. In the absence of protein, there is negligible non-specific binding. Additionally, in the presence of protein, a ring-like pattern is observed after washing, demonstrating that the biomarker is sandwiched in between the glass and the microbeads. While the 20-minute time falls within the WHO's recommended low-resource assay diagnosis time, the strong magnetic moment of Nd requires that the drop be positioned directly in the center of the ring. Nonetheless, the high signal-to-noise and a short assay time for results demonstrate beneficial properties for low-resource diagnostics.



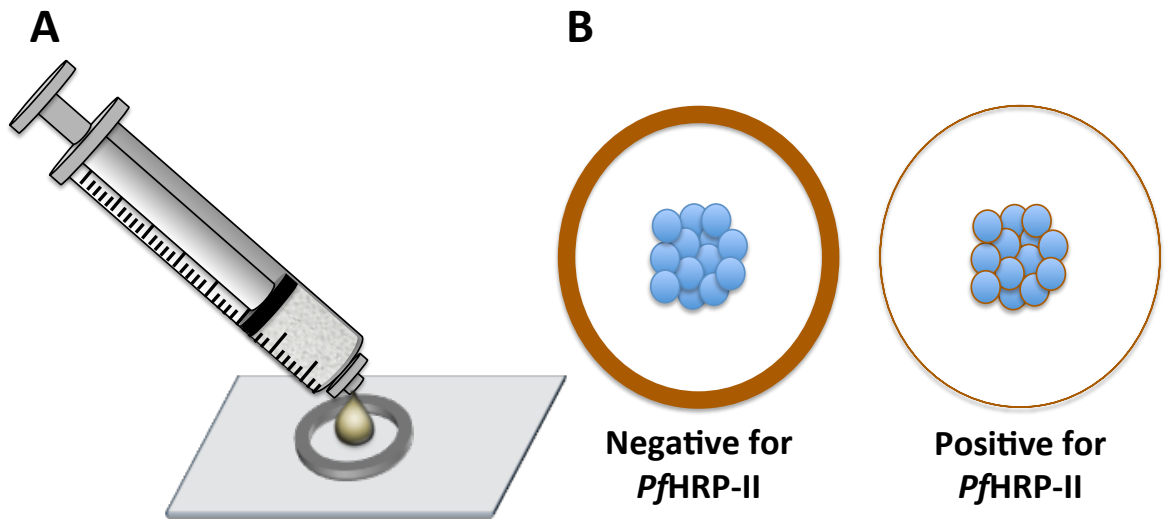
Supplemental Figure 2. Co(II)NTA Dynabead sandwich assays detecting rcHRP-II. (A) Schematic of the assay showing that after the Dynabeads (30X diluted from stock containing 0.005% v/v Tween 20 and 1% glycerol) are reacted with 1  $\mu$ M rcHRP-II for 30 seconds, the protein-particle conjugates are deposited (1  $\mu$ L) onto a Ni(II)NTA-functionalized glass slide. A neodymium ring magnet is placed directly underneath the glass slide to attract the Dynabead-biomarker conjugates in a radial configuration. After 20 minutes, the slide is placed in a 50 mL conical tube filled with deionized water, and shaken for 10 seconds to wash away non-specific binding. (B) Images captured with a Nikon camera show that the particles are sandwiched to the glass in the presence of protein. “HRP-II+” denotes 1  $\mu$ M rcHRP-II while “HRP-II-” denotes 0 rcHRP-II. The white bar scales to 1 mm. (All data collected with Mark Baglia in the Haselton lab).

### *Two-bead assays to detect PfHRP-II by manipulating flow patterns*

The initial bead experiments provide a framework for low-resource diagnostic design exploiting a single magnetic bead component. However, when creating these initial diagnostic technologies, it is advantageous to minimize the number of steps in order to reduce user bias. Current RDT's only necessitate a single step by spotting a patient blood sample onto a nitrocellulose strip and waiting 15-30 minutes for the strip to develop. With the previous two designs in this appendix along with the ring assay elucidated in Chapter V, there are three steps in each assay format: first mixing the protein with the beads, then depositing the biomarker-particle conjugate sample onto the functionalized glass, and finally washing the slide with water. Reducing the number of steps can further reduce user bias and increase assay reproducibility in the developing world. In the next assay format, I reduce the number of steps to two instead of three by eliminating the final water wash.

In this format, I introduce a second bead into the assay and manipulate microparticle flow patterns in order to demonstrate a specific bead configuration indicating positive or negative test results. Herein, a 50  $\mu\text{m}$  Ni(II)NTA sepharose bead is introduced in conjunction with the 1  $\mu\text{m}$  Dynabeads to sandwich the HRP-II biomarker. (Supplemental Figure 3). A protein sample is first mixed with a suspension containing 50  $\mu\text{m}$  Ni(II)NTA sepharose beads and 1  $\mu\text{m}$  Co(II)NTA magnetic Dynabeads. In the presence of a Nd ring magnet, a small volume is next deposited onto a clean glass slide and the flow patterns of the beads indicate infectivity. In the absence of protein, the magnetic beads do not interact with the larger sepharose beads and are separated in a thick, ring-like pattern caused by the magnet. The sepharose beads on the other hand,

settle to the center of the drop because of their large size. In the presence of biomarker, the HRP-II is sandwiched in between the sepharose and magnetic Dynabeads, so that fewer Dynabeads are attracted towards the ring magnet. The sepharose beads are bound to the biomarker-Dynabead conjugates and they settle to the middle of the drop rather than being radially attracted to the edge. The result is a thin ring at the drop edge because there is a greater concentration of magnetic Dynabeads in the middle of the drop. This assay format only involves two steps: first mixing the sample with the suspended particles and subsequently depositing the conjugate solution onto a clean glass slide with a ring magnet directly underneath it. In comparison to previous assays, this assay does not necessitate functionalized Ni(II)NTA glass because there is no sandwich component, thus eliminating an additional water wash step.



Supplemental Figure 3. Schematic of two-bead assay design for detection of *Pf*HRP-II. (A) A mixture of 50  $\mu\text{m}$  sepharose beads and 1  $\mu\text{m}$  Dynabeads are deposited onto a clean glass slide with a Nd ring magnet placed directly underneath the slide and the drop is allowed to dry. (B) Depiction of assay results for positively and negatively infected malarial patients, respectively.

### *Synthesis of 50 $\mu\text{m}$ Ni(II)NTA sepharose beads*

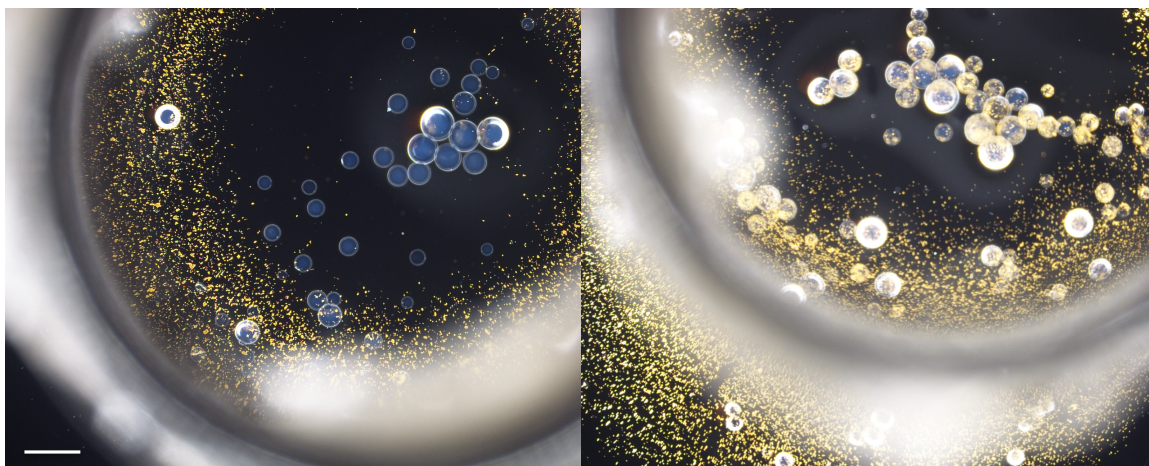
NHS-activated Sepharose 4 Fast Flow beads were purchased from Sigma-Aldrich suspended in isopropanol. Store beads in a refrigerator so that the surface groups do not hydrolyze.  $\text{N}_{\alpha},\text{N}_{\alpha}$ -Bis(carboxymethyl)-L-lysine hydrate (i.e. NTA ligand) was also purchased from Sigma-Aldrich and contains a free primary amine that is reactive towards NHS moieties.

These particles were first spun down for 2 minutes at 1000 gs in a microcentrifuge and washed with 1 mM cold HCl five times. The final suspension buffer consisted of 0.2 M  $\text{NaHCO}_3$  containing 0.5 M NaCl (pH 8.3). Particles were then reacted with 16 mM of the NTA ligand for four hours and washed in 0.1 M Tris-HCl (pH 8.5) five times. In order to coordinate Ni(II) to the NTA ligand, particles were charged with 0.1 M  $\text{NiCl}_2$  overnight in 0.1 M Tris-HCl (pH 8.5). Particles were then washed five times and finally resuspended in 0.1 M Tris-HCl.

### *50 $\mu\text{m}$ sepharose/1 $\mu\text{m}$ Dynabead two-bead assay*

Upon reacting the HRP-II biomarker with a suspension of sepharose beads and magnetic Dynabeads for 15 minutes, the conjugate suspension was deposited onto a clean glass slide containing a Nd ring magnet directly above the glass. As soon as the suspension is deposited in the middle of the ring magnet, the magnetic Dynabeads are attracted towards the drop edge, closest to the magnet. It is clearly evident that in this assay design, in the presence of biomarker, images show that the protein is sandwiched in between the larger sepharose beads and the smaller Dynabeads (Supplemental Figure 4). Because the images are taken during evaporation, the total time required for results is 20

minutes: 15 minutes for protein incubation time with the particles and images are captured 5 minutes into drying. Images of the sepharose beads have to be captured while wet because after drying, the beads shrivel up, hence complicating the assay. Therefore an alternative large microbead system is essential for this assay that can maintain its spherical integrity upon drop drying.



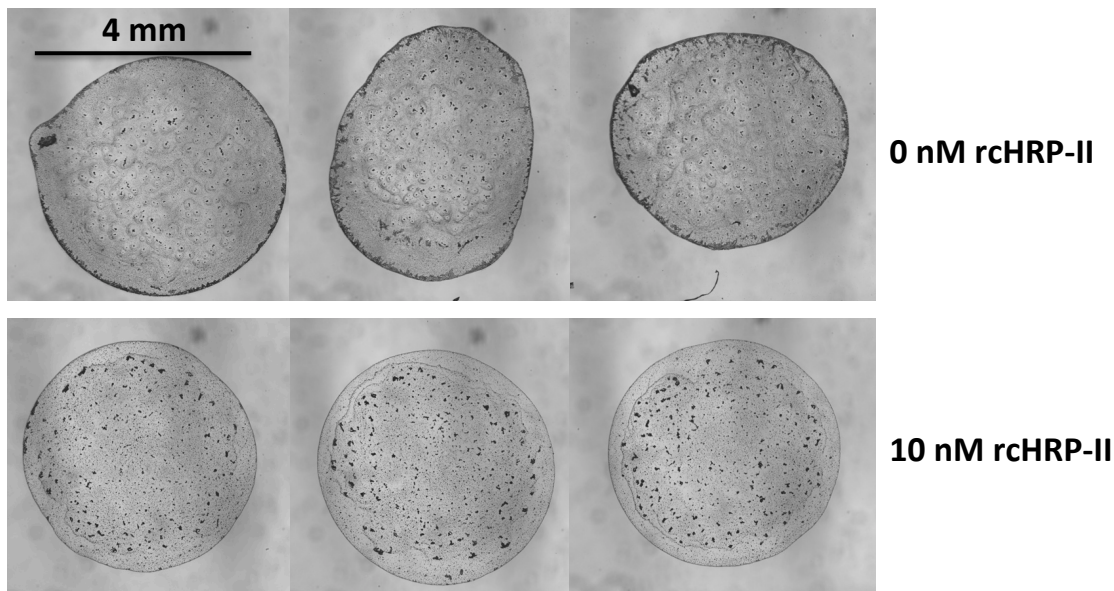
Supplemental Figure 4. Two-bead assay consisting of 50  $\mu\text{m}$  Ni(II)NTA sepharose and 1  $\mu\text{m}$  Co(II)NTA Dynabeads. A suspension of both types of microparticle are mixed with HRP-II biomarker for 15 minutes before depositing 1  $\mu\text{L}$  in the middle of a ring magnet on a clean glass slide. The left image shows that in the absence of biomarker, Dynabeads do not adhere to the larger sepharose beads (blue spheres). The image on the right shows that in the presence of 1  $\mu\text{M}$  biomarker, the Dynabeads (small gold dots) stick to the larger sepharose beads because the biomarker is sandwiched in between them. These images are taken on a Nikon camera on an inverted microscope and are captured during evaporation. The white bar scales to 100  $\mu\text{m}$  and assay conditions are as follows: 0.1% Tween 20, sepharose beads diluted 10X from stock, Co(II)NTA beads diluted 40X from stock.

#### *50 $\mu\text{m}$ agarose/1 $\mu\text{m}$ Dynabead two-bead assay*

In order to build upon the current two-bead assay design, I decided to investigate 50  $\mu\text{m}$  Ni(II)NTA agarose beads mixed with the current configuration of 1  $\mu\text{m}$  Dynabead Co(II)NTA Dynabeads. Reactions are carried out as described in the previous



spharose/Dynabead design, but in this format, a magnet is not utilized. After a 15 minute protein incubation time with the particles, the suspension is deposited onto an amine-functionalized glass slide and allowed to dry. After 15 minutes, images are captured in the absence and presence of HRP-II biomarker (Supplemental Figure 5). The Dynabeads adhere to the radial flow patterns in the absence of biomarker, causing thick ring-like patterns. In contrast, the large agarose beads settle to the center of the drop. In the presence of biomarker, rcHRP-II is sandwiched in between the Dynabeads and agarose beads, forming large Dynabead-agarose aggregates in the center of the drop. As a result, a smaller percentage of Dynabeads flow radially to the drop edge and the ring appears thinner relative to the negative controls.



Supplemental Figure 5. Two-bead assay consisting of 50  $\mu\text{m}$  Ni(II)NTA agarose and 1  $\mu\text{m}$  Co(II)NTA Dynabeads. A suspension of both types of microparticle are mixed with HRP-II biomarker for 15 minutes before depositing 1  $\mu\text{L}$  on an amine-functionalized glass slide. These images are taken on a Nikon camera on an inverted microscope and are captured after drop evaporation (15 minutes after initial deposition). The assay conditions are as follows: PBS with 0.1% Tween 20, agarose beads diluted 2X from stock, Co(II)NTA beads diluted 40X from stock.

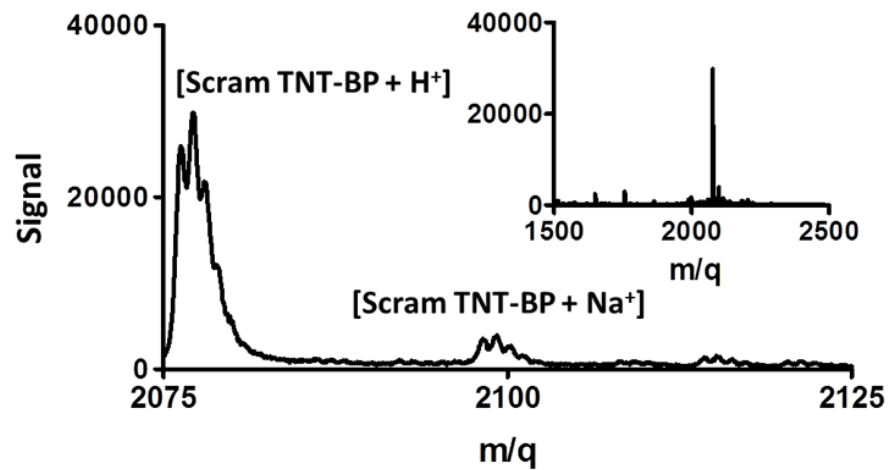
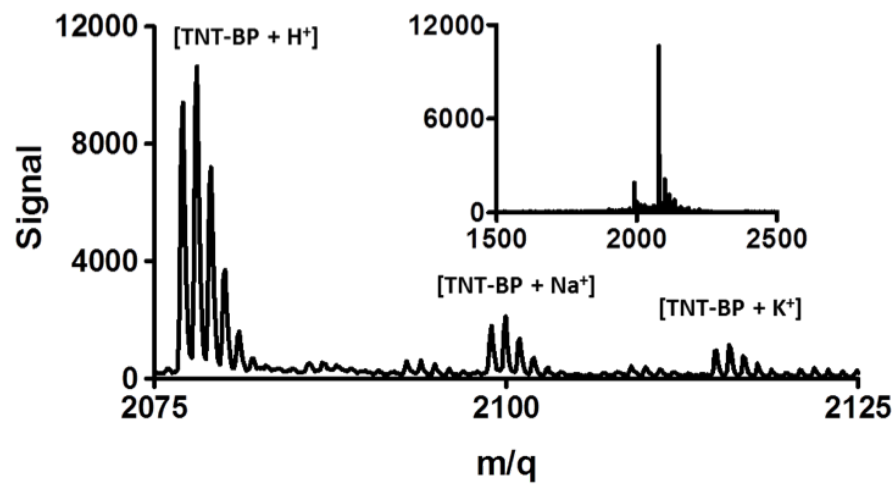
This assay also takes advantage of high concentrations of salt (1X PBS) and surfactant (0.1% Tween 20) so that the low contact angle increases the drop diameter, favoring coffee ring-like radial flow patterns for the dense Dynabeads. Even though the assay conditions in this format are different in comparison to the sepharose/Dynabead design, the incorporation of a strong Nd magnet may complicate the natural flow patterns of the microbeads. Nonetheless, I have demonstrated that two-bead designs can potentially reduce the assay to two steps and fall within the WHO's recommended threshold of 15-30 minutes for total assay time. Although I did not investigate complex matrix effects, preliminary data shows that these initial designs address some of the issues of low-resource diagnostics.

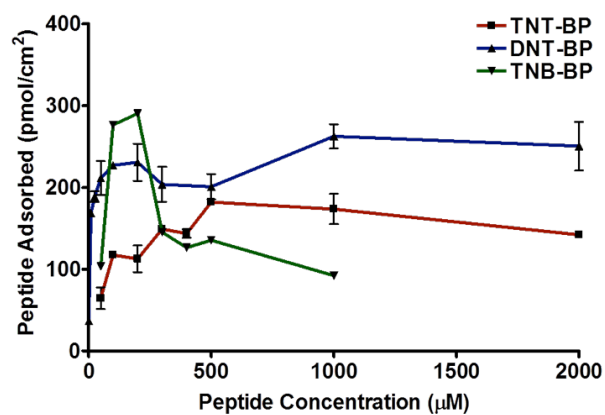
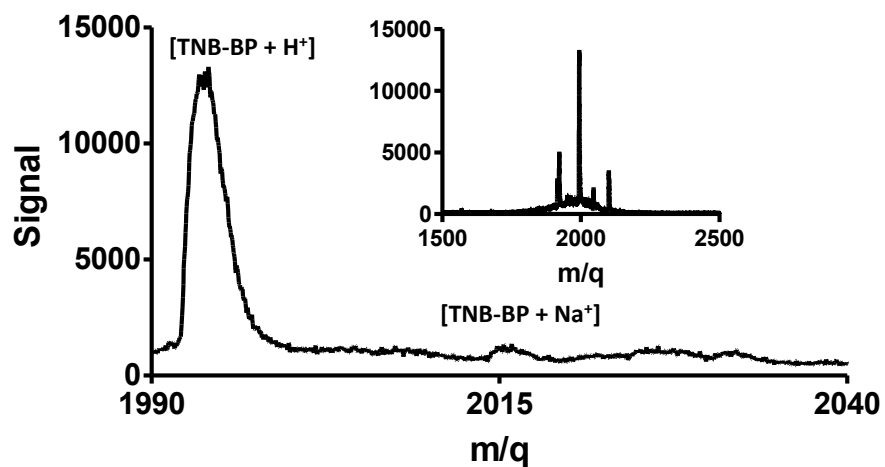
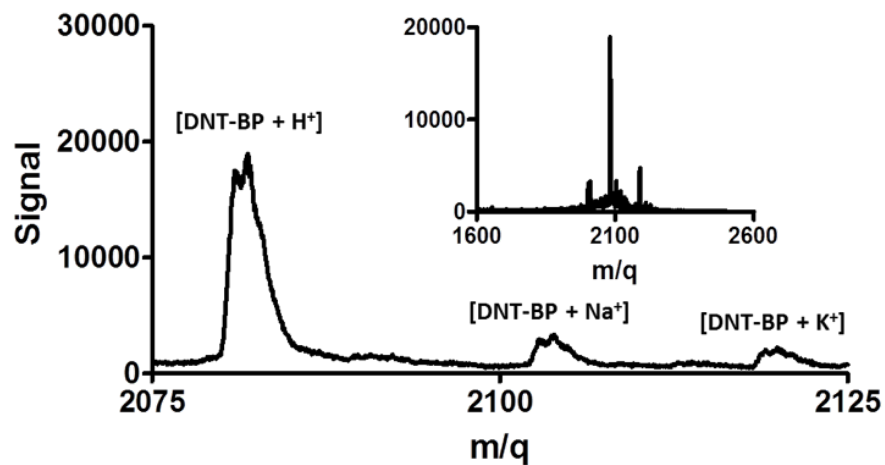


Appendix B

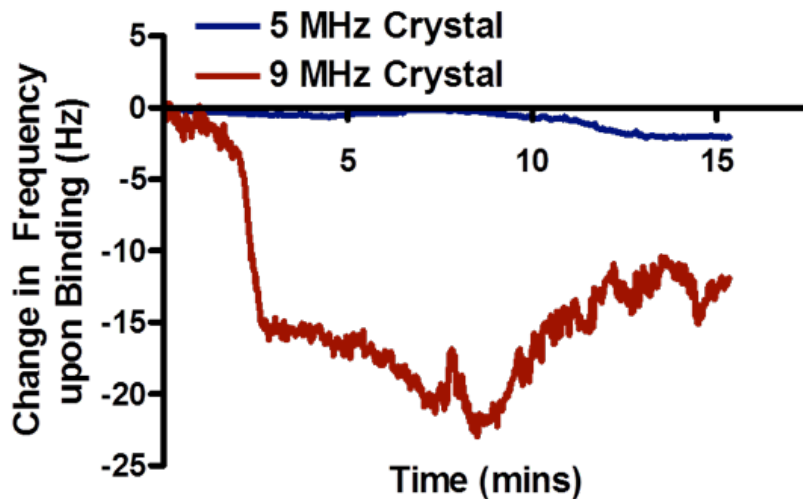
Supplementary Data: Chapter II

Supplemental Figure 6. MALDI-MS analysis of nitroaromatic-binding peptides, TNT-BP, SCRAM TNT-BP, DNT-BP, and TNB-BP.

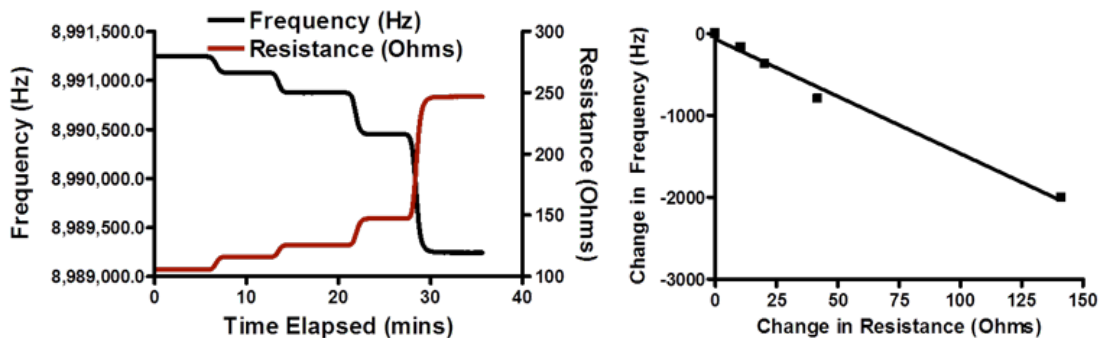




Supplemental Figure 7. Effect of peptide surface coverage versus immobilization concentration. The maximum surface coverage of recognition peptides were achieved at 500 µM, 1000 µM, and 200 µM for TNT-BP, DNT-BP, and TNB-BP, respectively.



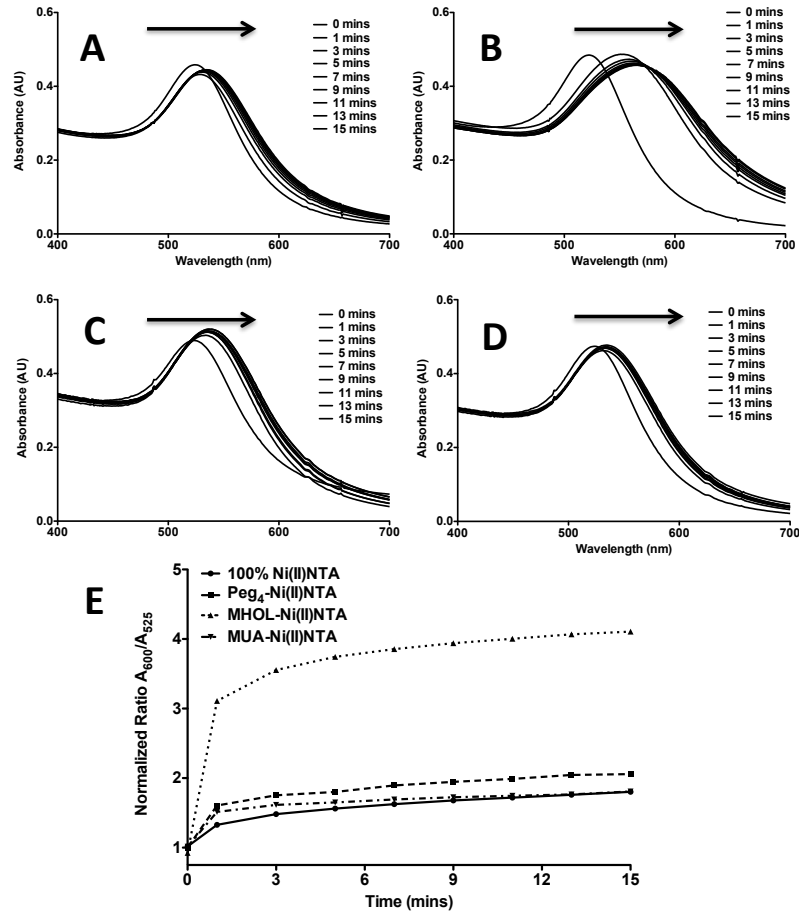
Supplemental Figure 8. Representation of 500  $\mu\text{M}$  TNT binding to immobilized TNT-BP using commercially available 5 and 9 MHz QCM chips. The frequency drop is denoted by a reduction in the crystal's oscillations, which correspond to positive mass binding. The 9 MHz QCM chip generates significantly higher sensitivity in comparison to 5 MHz chips, so that small nitroaromatic molecules could be easily detected. However, quantifying large peptide binding to Au could be more easily quantified using 5 MHz QCM chips.



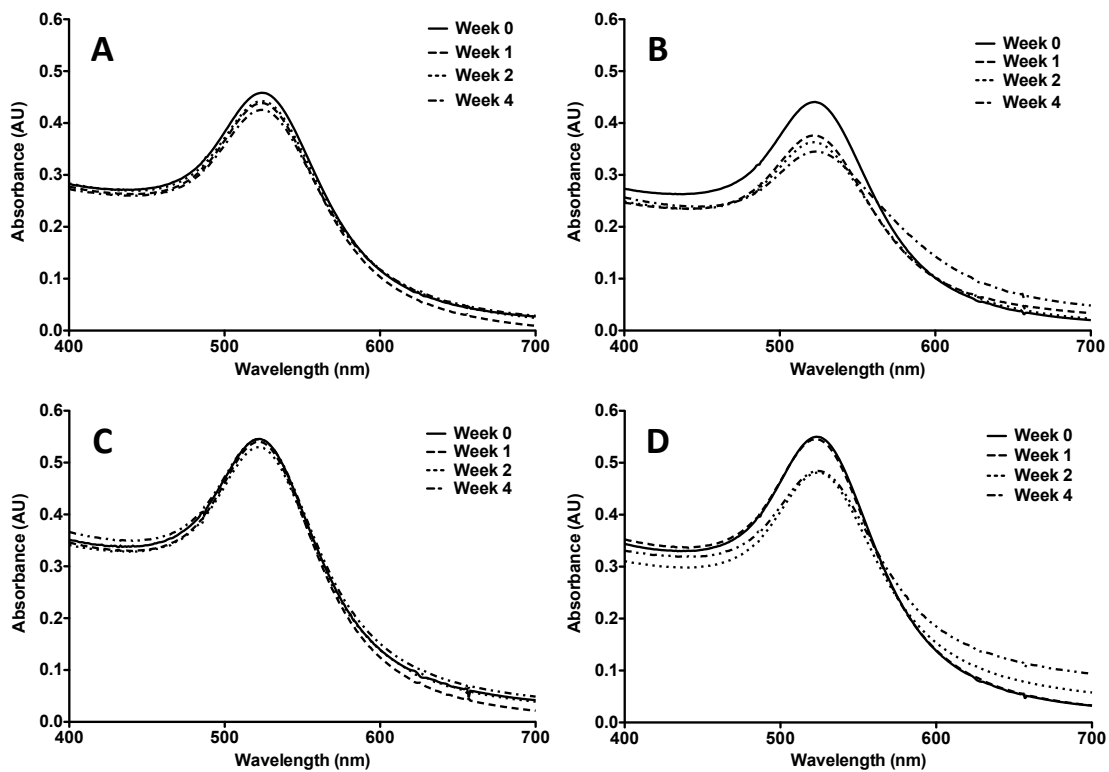
Supplemental Figure 9. Calculation of the resistance factor ( $\Delta R$ ) to account for changes in solution viscosity. The change in frequency and resistance is denoted for a Piranha-cleaned 9 MHz QCM chip exposed to 0, 5, 10, 20, and 40 wt% sucrose, respectively, dissolved in deionized water. The slope of the frequency versus resistance curve is -14.0, which is the value of the constant resistance factor for a 9 MHz QCM chip.

## Appendix C

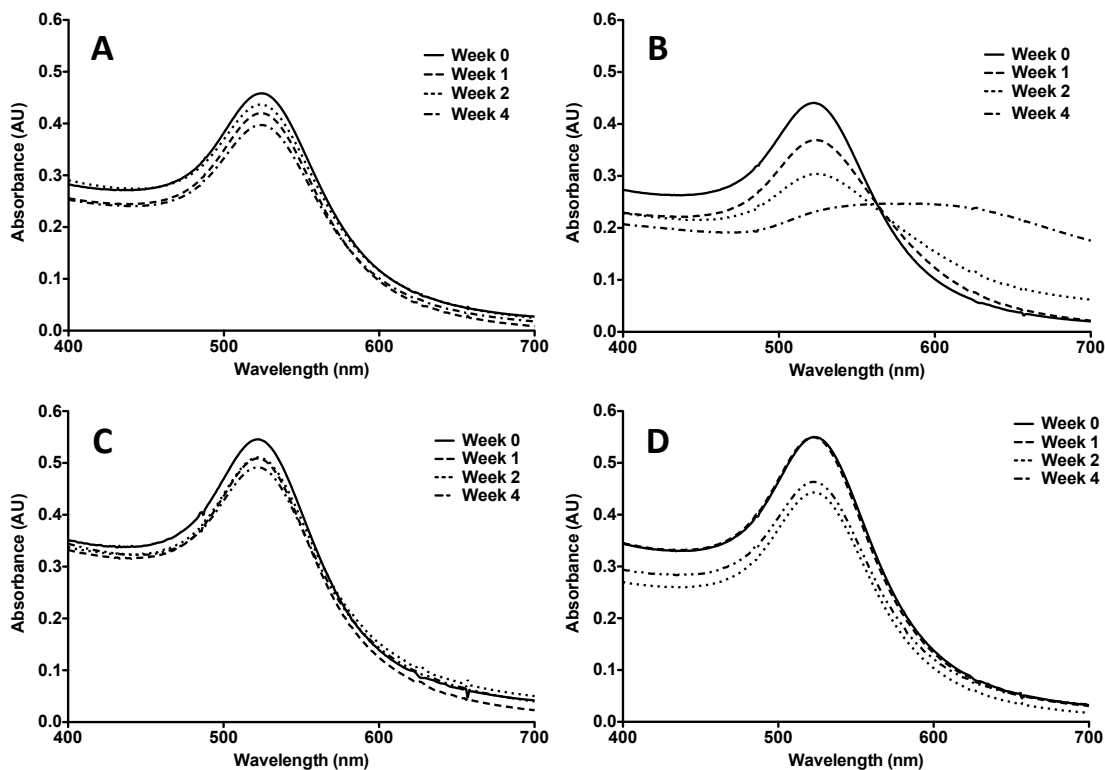
### Supplementary Data: Chapter IV



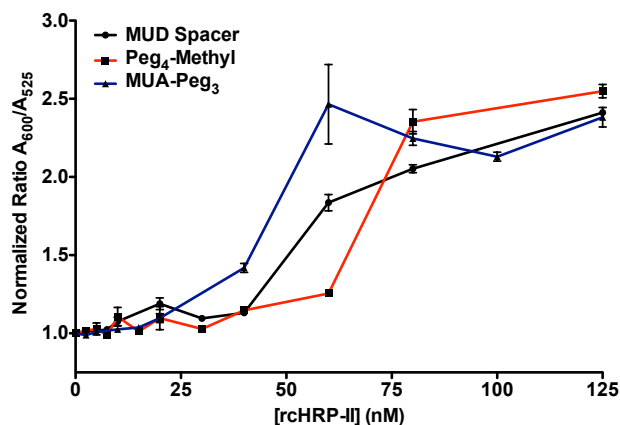
Supplemental Figure 10. Kinetic spectrophotometric shifts of (A) 100% Ni(II)NTA AuNPs, (B) MHOL:Ni(II)NTA AuNPs, (C) Peg<sub>4</sub>:Ni(II)NTA AuNPs, and (D) MUA:Ni(II)NTA AuNPs upon aggregation with 100 nM rcHRP-II (0.1 M MES with 0.025% Tween 20 at pH 5.5). The arrows indicate that the UV-vis spectra are redshifting as time increases. (E) Aggregation signal as a function of time. Aggregation occurs in as little as one minute, and slows down after 15 minutes.



Supplemental Figure 11. UV-vis spectra of 1 nM (A) 100% Ni(II)NTA AuNPs, (B) MHOL:Ni(II)NTA AuNPs, (C) Peg<sub>4</sub>:Ni(II)NTA AuNPs, and (D) MUA:Ni(II)NTA AuNPs stored in sealed Eppendorf tubes at room temperature for four weeks (0.1 M MES buffer with 0.025% Tween 20, pH 5.5).



Supplemental Figure 12. UV-vis spectra of 1 nM (A) 100% Ni(II)NTA AuNPs, (B) MHOL:Ni(II)NTA AuNPs, (C) Peg<sub>4</sub>:Ni(II)NTA AuNPs, and (D) MUA:Ni(II)NTA AuNPs stored in sealed Eppendorf tubes at 37°C for four weeks (0.1 M MES buffer with 0.025% Tween 20, pH 5.5).



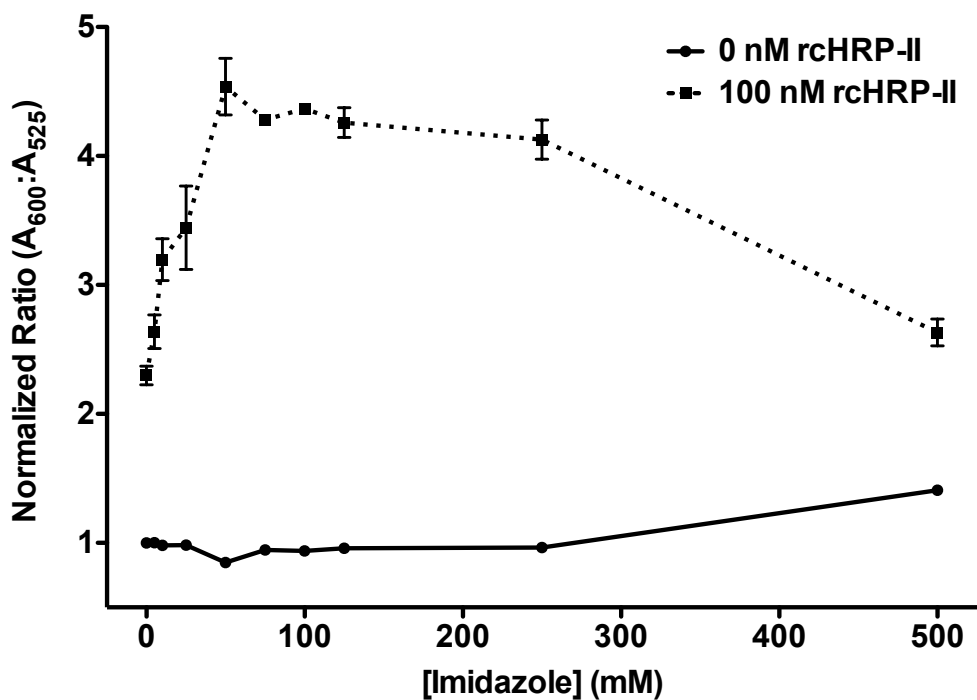
Supplemental Figure 13. Titration of rcHRP-II with 1 nM Ni(II)NTA AuNPs assembled with alternative spacer ligands in a 50:50 ratio to the Ni(II)NTA recognition ligand. Particles are reacted with rcHRP-II for 15 minutes in 0.1 M MES containing 0.025% Tween 20 (pH 5.5).

Supplemental Table 1. Limits of detection, confidence intervals, and sensitivities of rcHRP-II when Ni(II)NTA AuNP platforms are assembled with varying spacer ligands.

<b>Ni(II)NTA AuNP Platform</b>	<b>LOD (nM)</b>	<b>95% Confidence Interval (nM)</b>	<b>Sensitivity (Signal/nM)</b>
100% Ni(II)NTA AuNPs	51	39-60	0.0066
50:50 MHOL:Ni(II)NTA AuNPs	6.6	2.4-10	0.040
50:50 Peg <sub>4</sub> :Ni(II)NTA AuNPs	7.4	2.8-11	0.015
50:50 MUA:Ni(II)NTA AuNPs	6.7	5.2-8.0	0.021
50:50 MUD:Ni(II)NTA AuNPs	15.7	8.2-21.5	0.014
50:50 Peg <sub>4</sub> -Methyl:Ni(II)NTA AuNPs	13.4	0.75-22.0	0.004
50:50 MUA-Peg <sub>3</sub> :Ni(II)NTA AuNPs	18.3	8.5-24.7	0.031

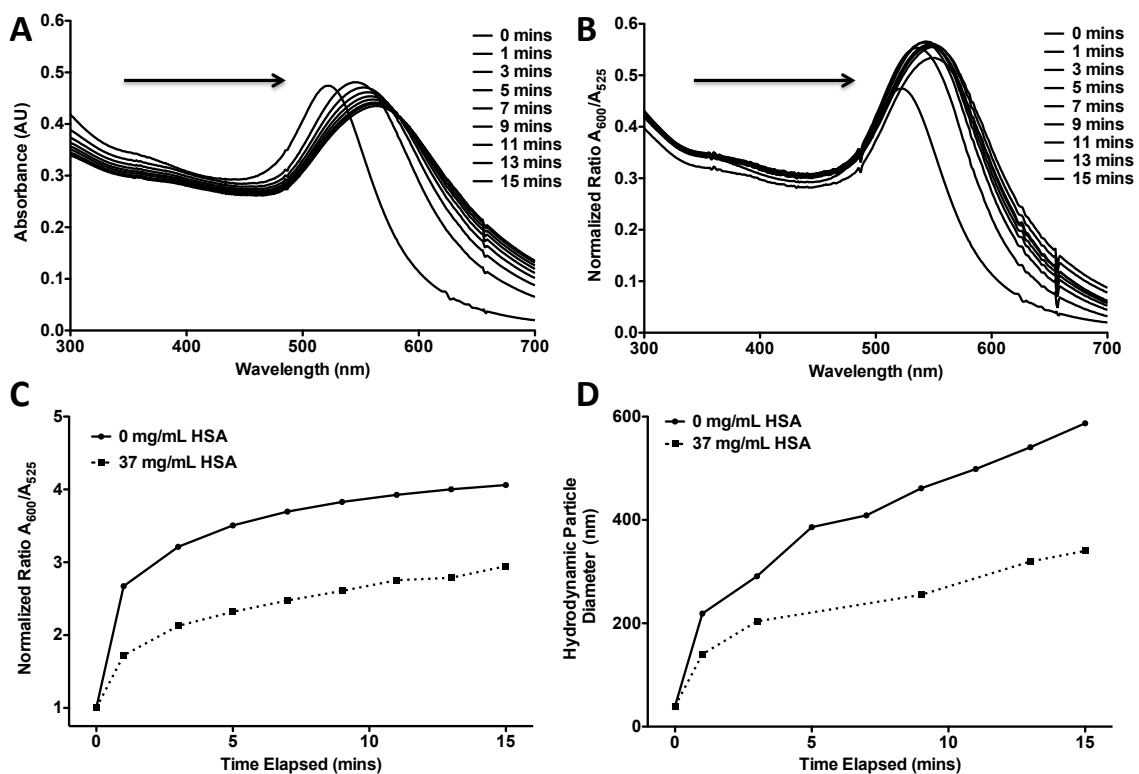
Supplemental Table 2. Limits of detection, sensitivity, and confidence intervals of rcHRP-II upon reactions with Peg<sub>4</sub>:Ni(II)NTA AuNPs when the biomarker is dissolved in a complex matrix

<b>[HSA] (mg/mL)</b>	<b>LOD (nM)</b>	<b>95% LOD CI (nM)</b>	<b>Sensitivity (Signal/nM)</b>	<b>95% Sensitivity CI (Signal/nM)</b>
37	2.9	1.47-4.14	0.0743	0.0670-0.0817
0	4.2	0.243-7.01	0.0533	0.0395-0.0672

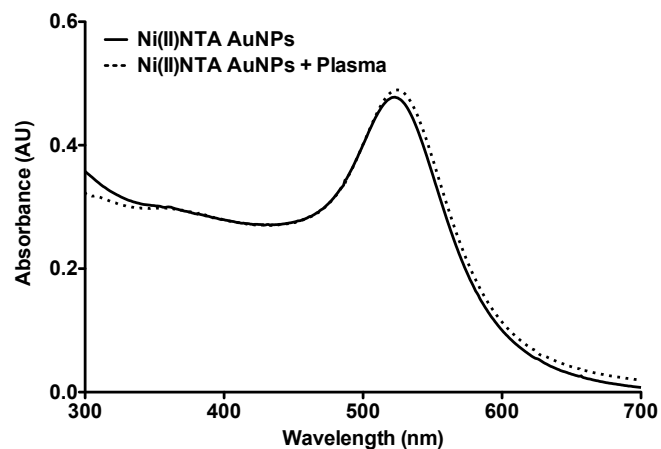


Supplemental Figure 14. Effect of imidazole on Peg<sub>4</sub>:Ni(II)NTA AuNP assay performance in 0.1 M MES buffer with 0.025% Tween 20 and 150 mM NaCl (pH 5.5). The particles suspended in buffer and varying concentrations of imidazole are reacted with 0 nM or 100 nM rcHRP-II, respectively. After 15 minutes incubation time, absorbance measurements are taken at 525 nm and 600 nm. In the absence of rcHRP-II, the Ni(II)NTA AuNPs are stable when exposed to 250 mM imidazole concentrations. Above 250 mM, the protonated imidazole cations begin to aggregate the Peg<sub>4</sub>:Ni(II)NTA AuNPs. In the presence of rcHRP-II, imidazole enhances assay performance linearly from 0 mM to 50 mM imidazole. Between 50 mM and 250 mM imidazole, the assay signal plateaus, whereas above 250 mM, assay signal decreases due to the lack of stability of the Ni(II)NTA AuNPs.

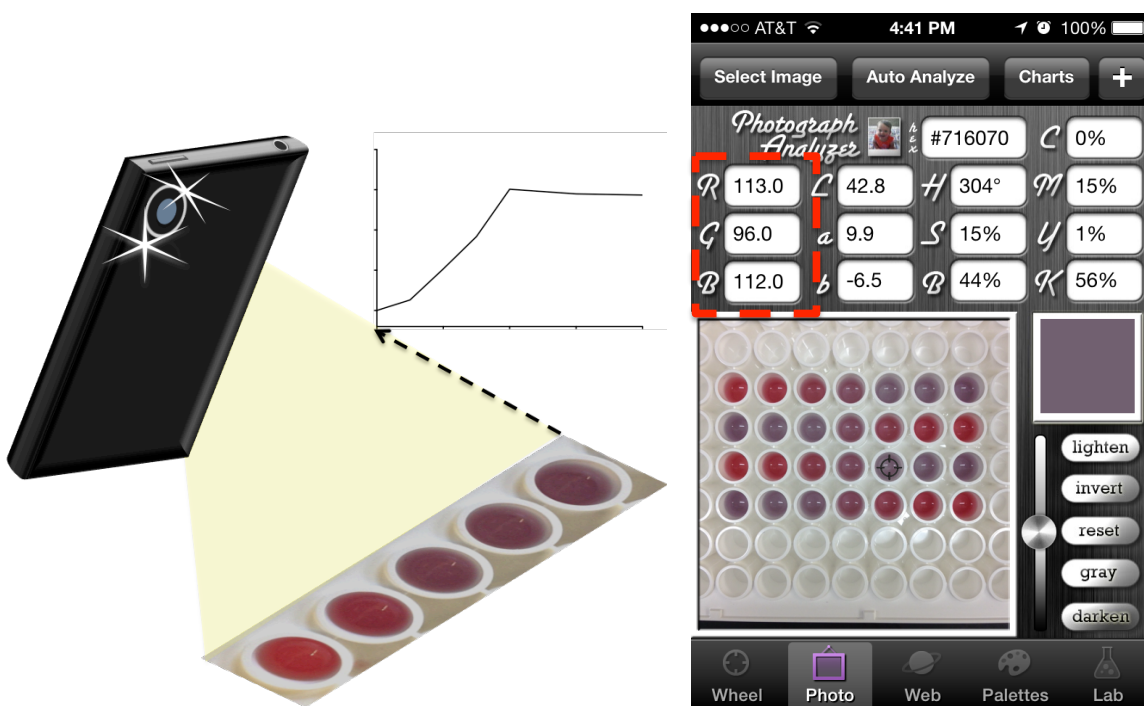




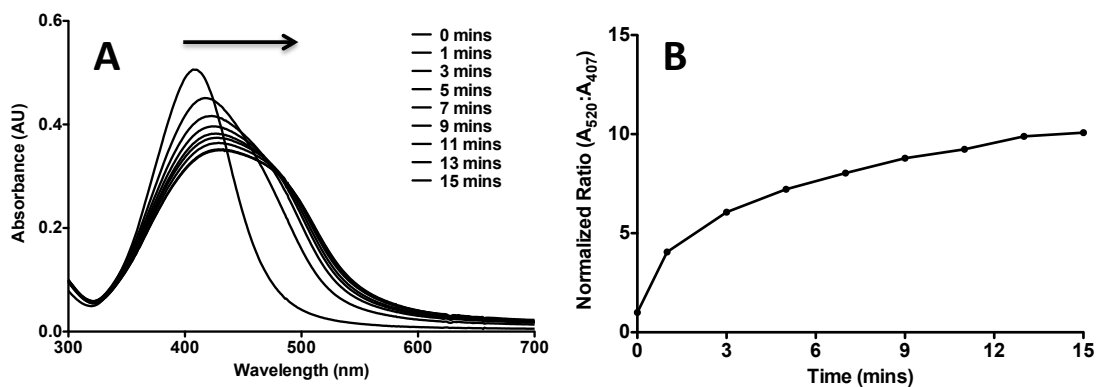
Supplemental Figure 15. Kinetics of Peg<sub>4</sub>:Ni(II)NTA AuNP aggregation induced by 100 nM rHRP-II. Particles are suspended in 125 mM imidazole and 150 mM NaCl in 0.1 M MES buffer with 0.025% Tween 20 (pH 5.5). There is a spectrophotometric redshift upon 100 nM rHRP-II addition when dissolved in (A) 0 mg/mL HSA and (B) 37 mg/mL HSA. The arrows show that the Peg<sub>4</sub>:Ni(II)NTA AuNP spectrum redshifts as a function of time. (C) Spectrophotometric kinetics demonstrating that aggregation and a color change occurs in as little as one minute. After five minutes, signal begins to plateau until the 15-minute mark. (D) Dynamic laser light scattering of Peg<sub>4</sub>:Ni(II)NTA AuNP aggregation, demonstrating that significant aggregation occurs in as little as one minute as the change in particle diameter difference is approximately 200 nm. In correspondence to the UV-vis spectra, aggregation slows significantly after five minutes.



Supplemental Figure 16. Stability of Peg<sub>4</sub>:Ni(II)NTA AuNPs in the presence of plasma. A 90  $\mu$ L Peg<sub>4</sub>:Ni(II)NTA AuNP suspension in 0.1 M MES containing 125 mM imidazole and 150 mM NaCl with 0.025% Tween 20 (pH 5.5) is incubated with 10  $\mu$ L whole plasma for 15 minutes before taking an absorbance spectrum. The lack of a significant spectral shift demonstrates that plasma does not induce non-specific aggregation of the particles, but the slight redshift does suggest that plasma non-specifically coats the surface of the particles.



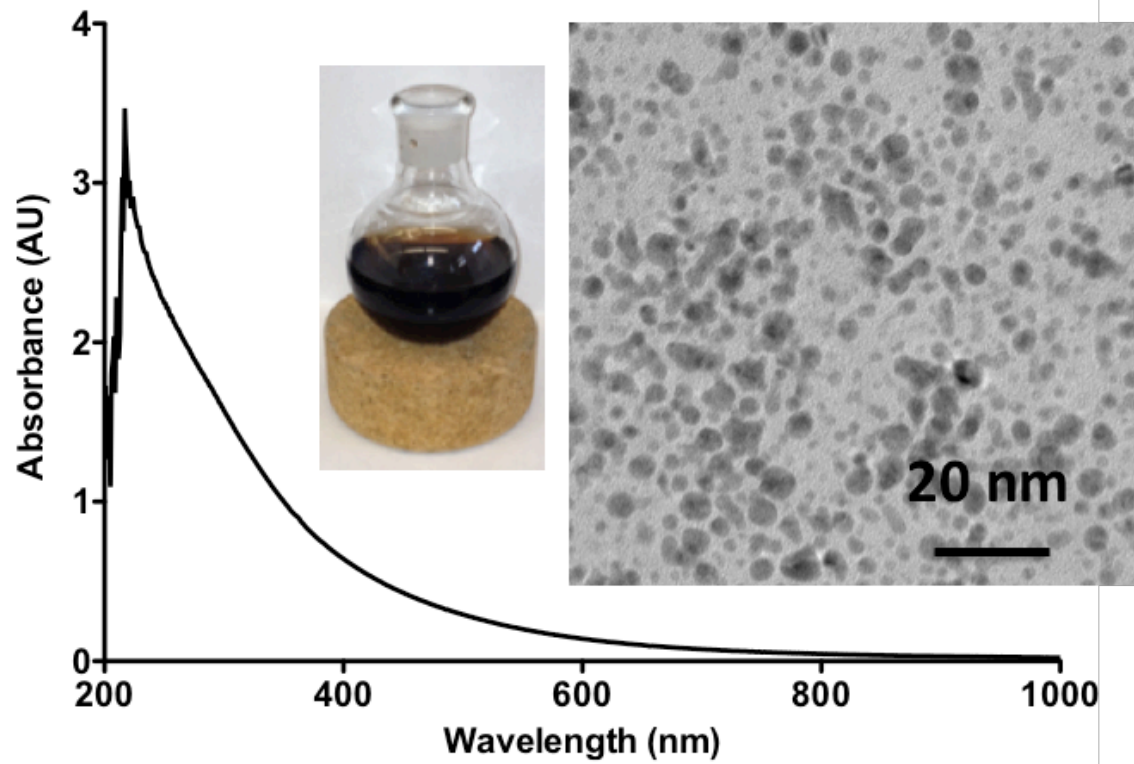
Supplemental Figure 17. Analysis of Peg<sub>4</sub>:Ni(II)NTA AuNP aggregation induced by rcHRP-II using an iPhone 4S equipped with the Color Companion (Digital Media Interactive, LLC) application. The Ni(II)NTA AuNPs are titrated with rcHRP-II (n=4). In the first and third rows, 0, 10, 20, 30, 40, 60, and 80 nM rcHRP-II concentrations increase from left to right. The second and fourth rows show a decrease in rcHRP-II concentrations from left to right to control for varying signal intensities due to light dimming effects. After capturing the image, it is uploaded into the Color Companion application and the circular bulls-eye is moved over a well, where signal intensity values are conferred for red, green, and blue colors. The dashed red box displays the raw red, green, and blue signal intensity values as the bulls-eye cursor is focused over one of the wells. To calculate final intensity, the green and blue intensities are averaged and divided by the red intensity.



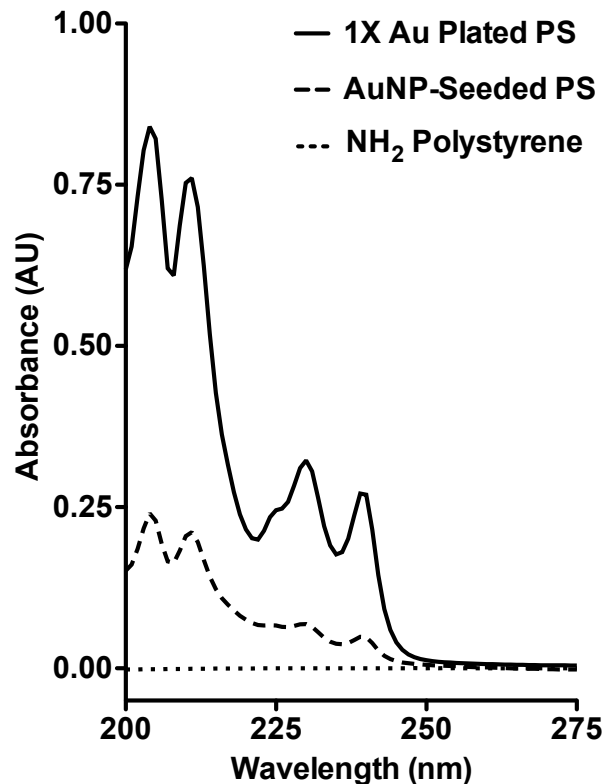
Supplemental Figure 18. Kinetics of Peg<sub>4</sub>:Ni(II)NTA AgNP aggregation induced by rcHRP-II. An 80 pM concentration of particles suspended in 0.1 M MES with 0.025% v/v Tween 20 (pH 5.5) is reacted with 100 nM rcHRP-II for over the course of 15 minutes. (A) UV-vis spectral profiles show a redshift over time, while (B) the aggregation signal plotted as a function of time shows that nearly half of the signal is generated in the first minute while it begins to plateau after 15 minutes.

## Appendix D

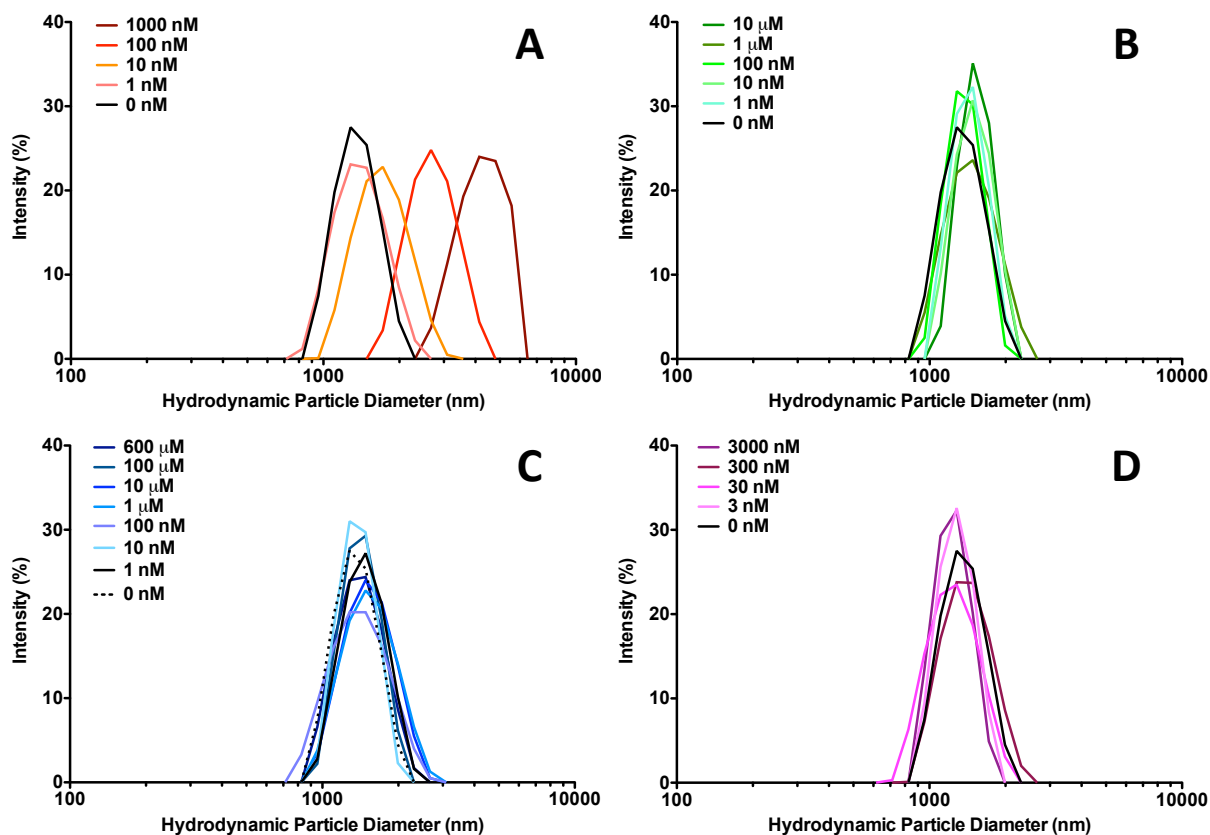
### Supplementary Data: Chapter V



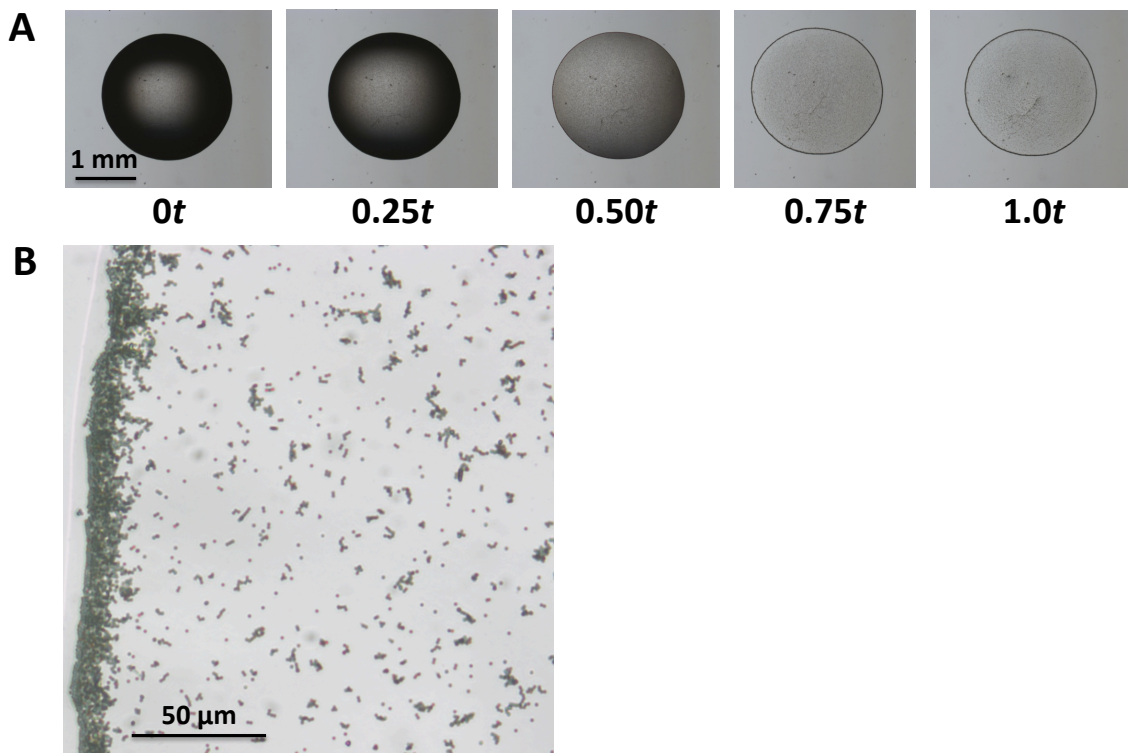
Supplemental Figure 19. Characterization of tetrakis(hydroxymethyl) phosphonium chloride-functionalized (THPC) AuNP seeds. The dark brown-colored AuNPs do not display a localized surface plasmon resonance peak in the UV-vis spectrum, indicating that the AuNPs are smaller than 5 nm in diameter. Inset is a TEM image of the AuNPs, where the average particle diameter was determined to be  $(3.4 \pm 1.1)$  nm.



Supplemental Figure 20. Quantifying Au adsorption onto the varying polystyrene spheres. The different polystyrene spheres at 1.1 pM concentrations are first treated with 8 mM KCN for 15 minutes. Afterwards the aliquots are centrifuged at 16,100 gs for 5 minutes. Next the supernatant is decanted and filtered through a 0.22 um filter. A UV-vis spectrum of the supernatant is measured and peaks at 204, 211, 230 and 240 nm are representative of the water-soluble,  $K^+[Au(CN)_2]$  complex that is formed when  $Au^0$  is reacted with KCN. It can be determined that for an aliquot of 1.1 pM AuNP-seeded PS, the average number of Au atoms encompassing the polystyrene sphere is  $9.03 \times 10^7$ , increasing the density of the sphere from 1.06 g/mL to 1.16 g/mL. After plating, the average number of gold atoms per particle increases to  $8.28 \times 10^8$ , increasing the average density of each particle to 1.49 g/mL.

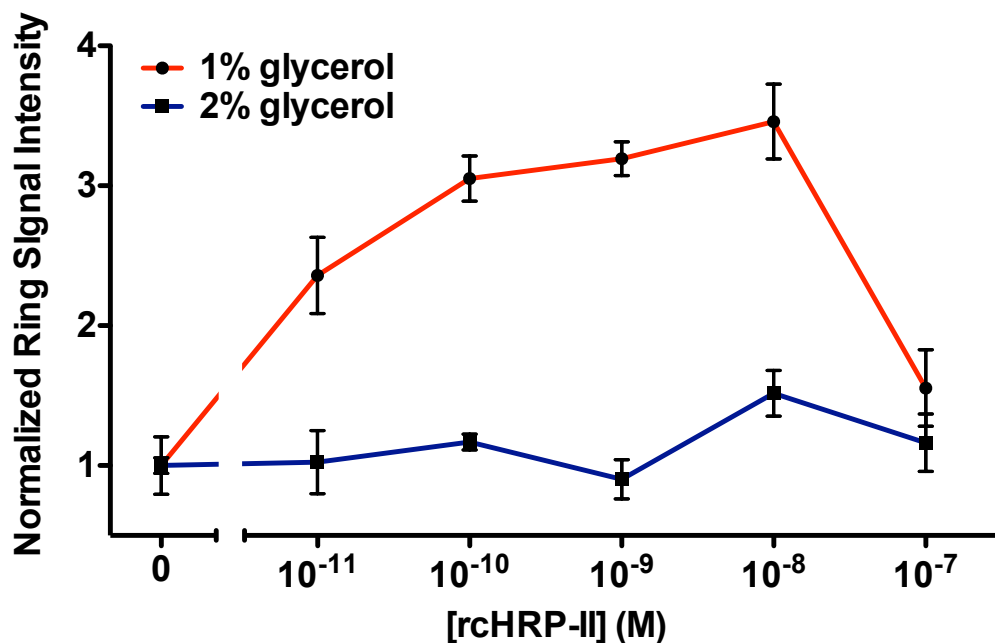


Supplemental Figure 21. Dynamic laser light scattering size distributions of Ni(II)NTA AuPSs in the presence of varying concentrations of positive and negative control proteins. A 1 pM suspension of Ni(II)NTA AuPS in 0.1 M MES buffer containing 125 mM imidazole and 0.020 v/v% Tween 20 (pH 5.5) is reacted against varying concentrations of proteins for 15 minutes before taking size distribution measurements. The shifts in size distribution profiles are evident due to particle aggregation when the particles are exposed to (A) rHRP-II, whereas no significant aggregation occurs when the particles are exposed to (B) GST, (C) HSA, and (D)  $\alpha_2$ -macroglobulin. Aggregation is not evident at the physiological concentrations of HSA (600  $\mu$ M, 40 mg/mL) and  $\alpha_2$ -macroglobulin (3  $\mu$ M, 2 mg/mL), highlighting the specificity of the particle platform. Although measurements are performed in triplicate, this data demonstrates a single size distribution profile of particles.

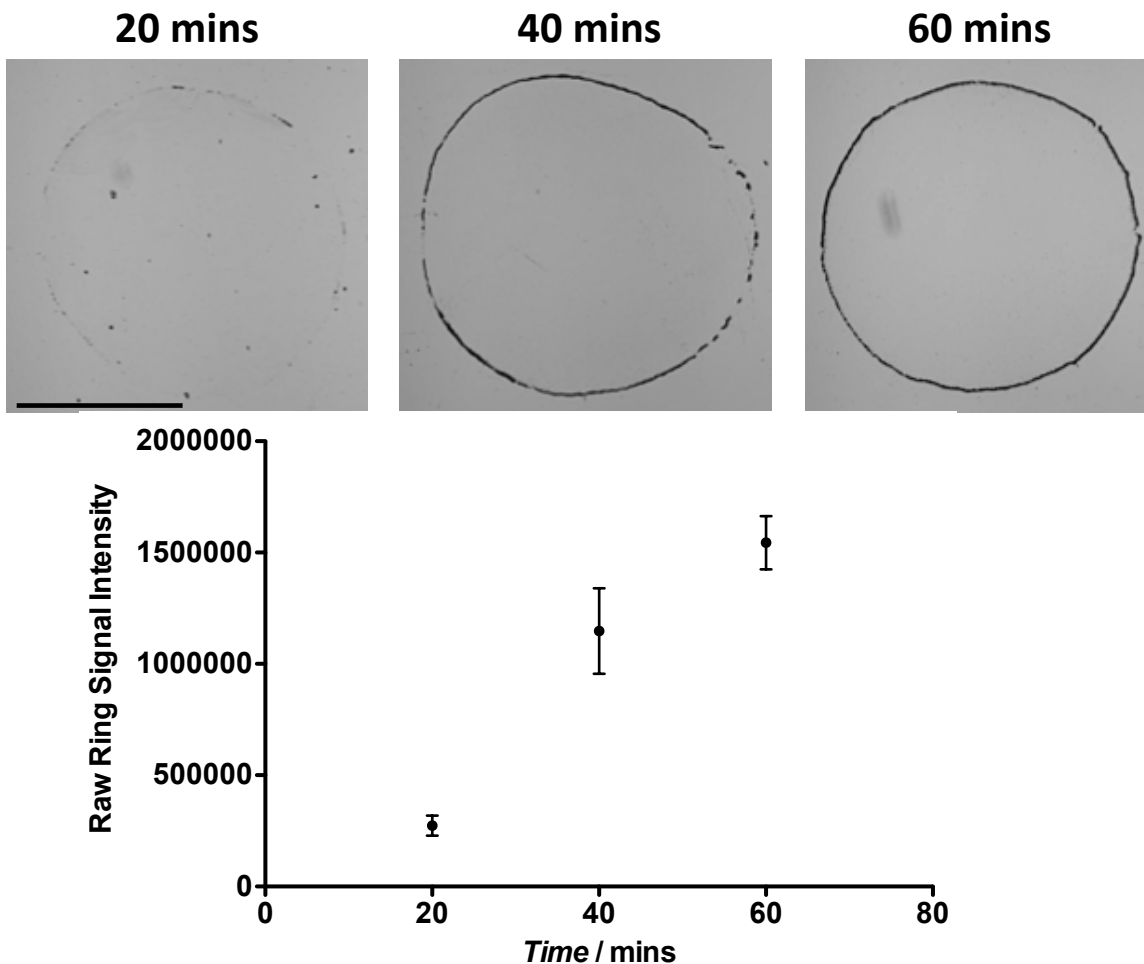


Supplemental Figure 22. Top-view progression of ring formation of Ni(II)NTA AuPSs during drop evaporation on a Ni(II)NTA-functionalized glass slide. (A) A 1  $\mu\text{L}$  suspension of 1 pM Ni(II)NTA AuPSs containing 0.020% Tween 20 and 1% glycerol is deposited onto a Ni(II)NTA-functionalized slide and evaporated. Top-view images showing the drop when the particle suspension is first deposited onto glass ( $0t$ ) and the progression of radially directed particle motion until a full ring is observed after drying ( $1.0t$ ). (B) High magnification image of the drop edge at  $1.0t$ , displaying that the ring is comprised of Ni(II)NTA AuPSs.

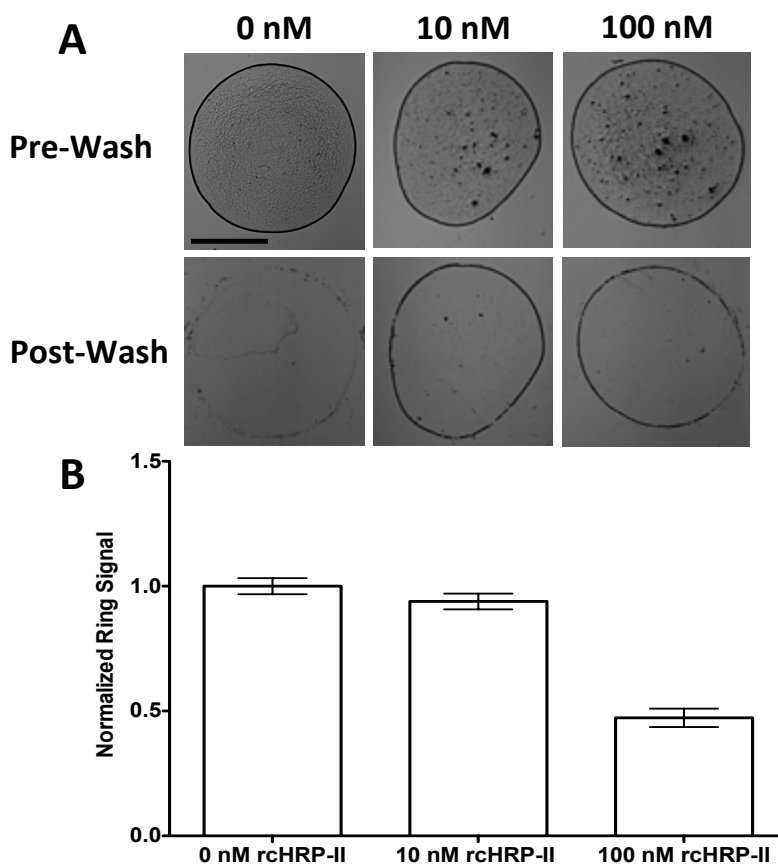




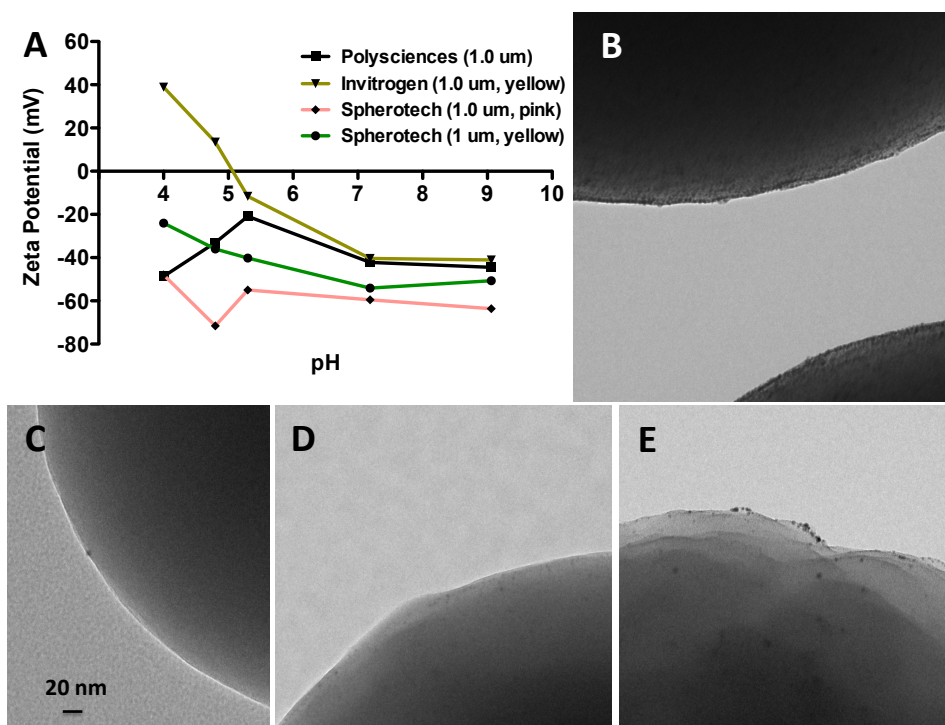
Supplemental Figure 23. Effects of glycerol as a blocking agent in the Ni(II)NTA AuPS ring assay for signal-to-noise optimization. A 1 pM concentration of particles containing 0.020% Tween 20 and glycerol was reacted with varying concentrations of rcHRP-II. After deposition of 1  $\mu$ L of a protein-particle conjugate solution onto the glass, slides are rinsed with water after one hour. In the absence of glycerol, no significant signal is observed and at 2% v/v glycerol concentrations, there is too much glycerol blocking the Ni(II)NTA sites on the glass surface, yielding a minimal signal. Therefore, a 1% (v/v) glycerol blocking concentration is optimal for this ring assay.



Supplemental Figure 24. Optimization of drying time with the Ni(II)NTA AuPS ring assay. A 1 pM concentration of Ni(II)NTA AuPS containing 1% glycerol and 0.020% Tween 20 is reacted with 10 nM rHRP-II, and a 1  $\mu$ L solution is deposited onto a Ni(II)NTA-functionalized glass slide. The slide is rinsed with water at time intervals of 20, 40 and 60 minutes. At a rinse time of 20 minutes, there is not sufficient time for the rHRP-II-Ni(II)NTA AuPS-conjugates to coordinate to the Ni(II)NTA glass. At 40 minutes, ring formation is more evident, but also incomplete. At 60 minutes, the maximum signal begins to plateau and complete ring formation is evident. The black bar scales to 1 mm.



Supplemental Figure 25. (A) Pre-wash and post-wash images of Ni(II)NTA AuPS rings in the presence of rCHRP-II. The black bar scales to 1 mm. (B) Ring signal is analyzed for the pre-wash images using the aforementioned methods in Figure 35. In the presence of 100 nM rCHRP-II, large AuPS aggregates settle vertically to the center of the drop, and the washed ring signal intensity decreases. When exposed to 100 nM rCHRP-II, the particles form large aggregates, and vertically settle ( $6.0 \times 10^{-5}$  cm/s) to the middle of the drop faster than migrating to the drop edge. Analysis of the pre-wash images at 100 nM rCHRP-II indicates that approximately twice as many particles at this concentration regime settle inside of the drop in comparison to the lower concentration regimes, thus decreasing ring signal.



Supplemental Figure 26. Choosing the Invitrogen polystyrene microsphere: Analysis of microbeads procured from various vendors. (A) Zeta potential measurements of different types of microbeads suspended in 10 mM NaCl at different pH values. The data in (A) was collected by Dr. Joshua Trantum. TEM images of microspheres (1  $\mu\text{m}$ ) purchased from (B) Invitrogen, (C) Spherotech, (D) Spherotech, and (E) Bangs Laboratories after electrostatically adsorbing 2-4 nm AuNP seeds. Although gold can be plated onto polystyrene in a uniform, tailored nanoshell using beads procured from Invitrogen, beads purchased from other vendors do not display the same levels of consistency. Since the gold-plating process begins with amine-terminated polystyrene, each supplier provides beads with different concentrations of primary amines on the surface. This can be probed by taking zeta potential measurements of amine-terminated polystyrene spheres and TEM images of AuNP-seeded spheres. The purpose of zeta potential is to measure the relative surface charge of a bead or particle surface. In order to validate the surface concentrations of amine groups on the particle surface, zeta potential measurements indicate that only the Invitrogen beads demonstrate positively charged zeta potential values below pH 5. All of the other particles exhibit negative zeta potentials at all of the pH values, meaning Invitrogen beads have the highest relative surface coverage of amines on the particle surface. To probe this further, each type of particle underwent the AuNP seeding step to determine if the negative surface charge impacts the seeding process. The Invitrogen microparticles exhibit a uniform monolayer of AuNP seeds as shown by the TEM images. However, all of the other particles display sparse coverage of THPC-functionalized AuNPs. It is hypothesized that the overall negative charge of the surfaces of the Spherotech, Polysciences, and Bangs particles repels the negatively charged AuNPs, yielding poor AuNP coverage. In contrast, the positively charged Invitrogen particles demonstrate high AuNP coverage, which is favorable for adsorbing AuNP seeds to act as catalytic sites for subsequent gold plating.

## Christopher Peter Gulka

1711 18<sup>th</sup> Ave S Apt C-3

Nashville, TN 37212

617-803-5198

*chris.gulka@vanderbilt.edu and chrisgulka22@gmail.com*

### EDUCATION

**Ph.D.** Chemistry, December 2014

Vanderbilt University, Nashville, TN

Advisor: Dr. David W. Wright

**Dissertation Title:** “Gold as a Sensing Platform for the Rapid Detection of Explosives and Malarial Biomarkers.”

**B.S.** Chemistry, May 2009

Minor in Latin American and Iberian Studies

University of Richmond, Richmond, VA

Advisor: Dr. Michael C. Leopold

La Universidad de Blas Pascal, Córdoba, Argentina (May 2007-July 2007 study abroad)

### RESEARCH EXPERIENCE

**Post-Doctoral Fellow**

Vanderbilt University, Nashville, TN

Advisor: Dr. David W. Wright

2014-present

**Graduate Student in Chemistry**

Vanderbilt University, Nashville, TN

Advisor: Dr. David W. Wright

2009-2014

**Undergraduate Research Fellow**

University of Richmond, Richmond, VA

Advisor: Dr. Michael C. Leopold

2008-2009

### PUBLICATIONS

1. **Gulka, C. P.**, Swartz, J. D., Trantum, J. R., Davis, K. M., Peak, C. M., Denton, A. J., Haselton, F. R., Wright, D. W. Detection of the Malarial Biomarker *Plasmodium falciparum* Histidine-Rich Protein-II Using a Surface-Coupled Ring of Ni(II)NTA Gold-Plated Polystyrene Particles. *ACS Appl. Mater. Interfaces* 2014 6(9): 6257-6263.

2. Swartz, J. D., **Gulka, C. P.**, Haselton, F. R., Wright, D. W. Development of a Histidine-Targeted Spectrophotometric Sensor Using Ni(II)NTA-Functionalized Au and Ag Nanoparticles. *Langmuir* 2011 27(24): 15330-15339.
3. Doan, T. D., Vargo, M. L., Gerig, J. K., **Gulka, C. P.**, Trawick, M. L., Dattelbaum, J. D., Leopold, M. C. Electrochemical Analysis of Azurin Thermodynamic and Adsorption Properties at Monolayer-Protected Cluster Film Assemblies - Evidence for a More Homogeneous Adsorption Interface. *J. Colloid Interface Sci.* 2010 352(1): 50-58.
4. Vargo, M. L.,\* **Gulka, C. P.**,\* Gerig, J. K., Manieri, C. M., Dattelbaum, J. D., Marks, C. B., Lawrence, N. T., Trawick, M. L., Leopold, M. C. Distance Dependence of Electron Transfer Kinetics for Azurin Protein Adsorbed to Monolayer Protected Nanoparticle Film assemblies. *Langmuir* 2010 26(1): 560-569. \*These authors contributed equally.

#### Submitted Manuscripts

5. **Gulka, C. P.**, Gizzie, E. A., Cliffel, D. E., Wright, D. W. Electrochemical Detection of 2,4,6-Trinitrotoluene at Colloidal Gold Nanoparticle Film Assemblies. *The NATO Science Programme for Peace and Security – Nanotechnology to Aid Chemical and Biological Defense*.
6. **Gulka, C. P.**, Swartz, J. D., Wright, D. W. Ni(II)NTA AuNPs as a Low-Resource Malarial Diagnostic Platform for the Rapid Colorimetric Detection of *Plasmodium falciparum* Histidine-Rich Protein-2. *Talanta*.

#### Manuscripts in Preparation

7. **Gulka, C. P.**, Bauer, W. S., Silva-Baucage, L., Markwalter, C. F., Adams, N. M., Wright, D. W. Capture-and-Release of the Malarial Biomarker *Plasmodium falciparum* Lactate Dehydrogenase for the Enhancement of Rapid Diagnostic Tests.

### PRESENTATIONS

1. *Coffee Rings as Low-Resource Malaria Diagnostics*. Materials Chemistry Division, 66<sup>th</sup> Southeastern Regional Meeting of the American Chemical Society, Nashville, TN, October 2014 (oral presentation).
2. *Electrochemical Detection of 2,4,6-Trinitrotoluene at Gold Nanoparticle Film Assemblies*. NATO Advanced Research Workshop on Nanotechnology to Aid Chemical and Biological Defense, Antalya, Turkey, September 2014 (poster presentation).
3. *Coffee Rings as Low-Resource Malarial Diagnostics*. Vanderbilt University Graduate Student Council Three-Minute Thesis, Nashville, TN, April 2014 (oral presentation).
4. *Low-Resource Coffee Ring Diagnostics: Detection of the Malarial Biomarker PfHRP-II Using a Surface-Coupled Ring of Ni(II)NTA Gold Particles*. Vanderbilt Institute of Nanoscale Science and Engineering 14<sup>th</sup> Annual Nanoscience and Nanotechnology Forum, Nashville, TN, November 2013 (poster presentation).

5. *Low-Resource Coffee Ring Diagnostics: Detection of the Malarial Biomarker PfHRP-II Using a Surface-Coupled Ring of Ni(II)NTA Gold Particles*. Vanderbilt Institute of Chemical Biology 7<sup>th</sup> Annual Student Research Symposium, Nashville, TN, August 2013 (oral presentation).
6. *Nano and Microparticle Malaria Coffee Ring Diagnostic Platforms*. Vanderbilt Institute of Nanoscale Science and Engineering 13<sup>th</sup> Annual Nanoscience and Nanotechnology Forum, Nashville, TN, October 2012 (poster presentation).
7. *Biomimetically Inspired Recognition of 2,4,6-Trinitrotoluene*. Chemical and Biological Defense Science and Technology Conference, Las Vegas, NV, November 2011 (poster presentation).
8. *Biomimetically Inspired Recognition of 2,4,6-Trinitrotoluene*. Vanderbilt Institute of Chemical Biology 5<sup>th</sup> Annual Student Research Symposium, Nashville, TN, August 2011 (poster presentation).
9. *Distance Dependence of Biological Electron Transfer Kinetics: Azurin Protein Adsorbed to Monolayer Protected Nanoparticle Film Assemblies*. University of Richmond School of Arts and Sciences' 24<sup>th</sup> Annual Student Research Symposium, Richmond, VA, April 2009 (poster presentation with John Gerig).
10. *Distance Dependence of Biological Electron Transfer: Azurin at Self-Assembled Monolayers Versus Nanoparticle Platforms*. Nanochemistry Division, 60<sup>th</sup> Southeastern Regional Meeting of the American Chemical Society, Nashville, TN, November 2008 (poster presentation with John Gerig).

## **AWARDS**

Vanderbilt University Three-Minute Thesis People's Choice Award, April 2014  
 Vanderbilt University Three-Minute Thesis Finalist, April 2014  
 Vanderbilt Institute of Chemical Biology Oral Presentation Award, August 2013

## **MENTORSHIP AND TEACHING EXPERIENCE**

### **National Science Foundation Undergraduate Research Mentorship**

Vanderbilt University, Nashville, TN  
 Student mentored: Lidalee Silva-Baucage, May 2014-August 2014

### **Graduate Rotation Student Research Mentorship**

Vanderbilt University, Nashville, TN  
 Students mentored: Westley Bauer, Braden Durbin  
 August 2012-October 2012

### **Undergraduate Research Mentorship**

Vanderbilt University, Nashville, TN  
 Student mentored: Alec Pawlukiewicz,\* October 2011-April 2014  
 \*Awarded undergraduate research award for outstanding senior student in chemistry

### **Organic Chemistry Laboratory Teaching Assistant**

Vanderbilt University, Nashville, TN

August 2009-May 2010

## **TECHNICAL SKILLS**

### **Instrumentation and Techniques**

Peptide synthesis

HPLC separation of peptides

MALDI mass spectrometry of peptides

Electroanalytical techniques (voltammetry, polarography, potentiometry)

Substrate-ligand binding kinetics (quartz crystal microbalance and bio-layer interferometry)

Transmission electron microscopy of nanomaterials, micromaterials, and biological systems

Phase-contrast imaging of micromaterials

Dynamic laser light scattering characterization of nanomaterials

Raman spectroscopy of nanomaterial substrates

UV-Vis, IR spectroscopy, fluorescence spectroscopy

Atomic absorption/emission spectroscopy, inductively-coupled plasma-optical emission spectroscopy

MS Office, ImageJ, Image Pro Plus, Graphpad Prism, Origin

Manuscript preparation

## **OUTREACH AND COMMUNITY SERVICE**

### **Outreach**

Sharefest-A Showcase of Emerging Communications Strategies on Campus

Vanderbilt University, Nashville, TN

April 2014

### **Community Service**

Alpha Phi Omega service fraternity

University of Richmond, Richmond, VA

March 2007-May 2009